On driven neural assemblies:
synchrony, chaos and entropy.

Guillaume Lajoie

A dissertation
submitted in partial fulfillment of the
requirements for the degree of

Doctor of Philosophy

University of Washington

2013

Reading Committee:

Dr Eric Shea-Brown, Chair

Dr Nathan Kutz

Dr Bernard Deconinck

Dr Adrienne Fairhall

Program Authorized to Offer Degree:
Applied Mathematics

University of Washington

Abstract

On driven neural assemblies:
synchrony, chaos and entropy.

Guillaume Lajoie

Chair of the Supervisory Committee:
Professor Dr Eric Shea-Brown
Applied Mathematics

In this dissertation, I address mathematical problems arising from the field of theoretical neuroscience that share a common theme: temporally driven neural networks treated as perturbed, coupled nonlinear dynamical systems. Guided by this theme, I present projects falling in two main categories.

The first relates to synchrony, or lack thereof, in neural populations receiving a common input. This is intimately linked to studies of neural pathologies such as Parkinson's disease and their treatments via neuroprosthetics. Here, synchronous dynamics within certain neural nuclei disrupt normal brain functions and electrical stimulation can restore them. How do these networks synchronize? How can we break this synchrony with (global) input stimulation? I use a variety of tools such as geometric perturbation theory, discrete dynamical systems and numerical simulations to approach these questions.

The second set of projects is motivated by neural coding, or the ability of neural networks to encode information from a stimulus that drives their dynamics. Encoding of a signal by a dynamical system strongly depends on its reliability: the ability of a system to reproduce similar output, given the same stimulus, on many trials where initial conditions change. Many large networks such as the ones found in cortex are

believed to be chaotic and hence highly sensitive to small changes in initial state. How does such chaos influence the reliability of spikes in large driven networks? What are the implications of the resulting unreliability on the neural coding of stimuli? I use mathematical techniques from random dynamical systems and information theory, along with large-scale numerical simulations, to address these questions for large networks of spiking neurons.

TABLE OF CONTENTS

LIST OF FIGURES

Figure Number Page

ACKNOWLEDGMENTS

The author wishes to acknowledge the support of many that have made this dissertation possible. First and foremost, Dr. Eric Shea-Brown for his guidance and mentorship as an advisor. The staff and members of the applied mathematics department at the University of Washington. The scientific colleagues and mentors: Joshua Goldwyn, Nicholas Cain, Natasha (Alex) Cayco Gajic, Yu Hu, Tim Oleskiw, Kameron Decker Harris, Megan Lacy, Mike Famulare, Michael Schwemmer, Andrea Barreiro, Joel Zylberberg, Braden Brinkman, Kevin K. Lin, Adrienne Fairhall, Nathan Kutz, Bernard Deconinck, Jean-Philippe Thivierge and Eduardo Blanchard Wrigglesworth the IV. The countless friends and family members whose support and kindness made this all possible.

The research presented in this manuscript was supported in part by: NSF grants DMS-0817649 and DMS-0907927, NSERC Graduate Fellowship, Burroughs-Wellcome Fund, NIH-UW Center for Computational Neuroscience training grant, University of Washington, XSEDE supercomputing platform.

DEDICATION

To my parents, Charlotte and Léon

Chapter 1

INTRODUCTION AND BACKGROUND

In 1952, Hodgkin and Huxley successfully derived a biophysically-based mathematical model of the giant squid axon [52]. Since then, it has become clear that the marriage of mathematics and physiology presents a powerful approach to understand the inner workings of the most complex organ found in nature: the brain. In a functional context, mathematical techniques are particularly well suited to address the central question: How do networks of neurons –the building blocks of the brain– dynamically interact, with each other and with the outside world, to ensure the survival, well being, and functioning of an animal?

In the past few decades, much effort has been invested in understanding how individual neurons and the synaptic connections between them operate (e.g. [34, 59]). Key electrophysiological mechanisms, such as the action potential or *spike* –a rapid change in electrical potential across a neuron's membrane– are now well understood. However, predicting the behavior of neuronal populations remains a daunting task and is at the forefront of present computational neuroscience research.

In this dissertation, I study questions related to the central theme of *driven networks of biologically inspired dynamical systems*. More precisely, I am interested in two aspects of driven networks: (1) synchrony in neural populations receiving a common input and (2) the reliability of responses in neural networks driven by a stimulus. The former theme is intimately linked to dynamical pathologies like Parkinson's disease, while the latter is related to questions of how neural activity conveys information to other brain areas. Both are motivated by a common question: What constrains the dynamics of large systems of non-linear units in response to a signal?

From a mathematical perspective, this overarching question connects to non-autonomous networks of dynamical systems in two complementary ways. First, there is the question of dynamical behavior across the "neurons" that form a population. One can ask how well their behavior is correlated in response to a presented signal. Do they synchronize or do they remain independent? How rich are their responses and how much do they depend on intrinsic system attributes and input signal characteristics? Second, there is the question of reliability, or repeatability of responses given a fixed signal. If one presents the same input on many trials where initial system states change, how different can we expect the population dynamics to be? In the absence of stochastic noise, the main dynamical mechanism leading to system response variability is chaos (sensitivity to initial conditions). As we will see, chaos plays a central role in shaping the reliability of a system, which in turn regulates how information can be stored in a network's activity.

As described in detail below, this dissertation is motivated by precise questions about biological systems. However, the research presented is mathematical in flavor. I adopt the point of view that studying mathematical models of neural systems that are as simple and general as possible leads to a mechanistic understanding that bridges a wide range of scales and details. Building on existing literature, most of the models used throughout this manuscript are non-dimensionalized and contain as few parameters as possible, while preserving the key dynamical properties of the biological system they represent. This often allows for analytically tractable results that provide powerful insights about generalized system properties. I use a wide range of techniques from dynamical systems, stochastic dynamics, probability and information theories in concert with large-scale numerical simulations to tackle these challenging, high-dimensional and non-linear problems.

In what follows, I present a brief overview of recent progress and motivation behind the problems addressed throughout this dissertation.

1.1 Synchrony and asynchrony in driven neural populations

Part of this dissertation is inspired by theoretical studies of *Parkinson's Disease* (PD). PD is a neurological disorder arising from the death of *dopaminergic* neurons in a neural nucleus called the *substantia nigra* (SN). PD patients' motor functions are typically altered through one or many of the following symptoms: enhanced muscle rigidity, *bradykinesia* (or reduced motor function velocity) and tremor. Although the cause of this degenerative condition is not well understood, the onset of motor symptoms is believed to be a result of altered neural activity in a group of midbrain neural nuclei called *basal ganglia* (BG), containing neurons whose function is associated with motor control and learning. Indeed, reduced dopaminergic activity from SN considerably changes the dynamical properties of neurons throughout BG. In normal individuals, neural activity in BG is mostly irregular and uncorrelated. However, after the onset of PD, there is increased coherent and synchronous spiking activity between and within various BG sub-nuclei. The most pronounced changes are believed to be present in the *subthalamic nucleus* (STN) and the *globus pallidus interna* (GPi) and *externa* (GPe) [82, 38, 94] which are involved in the relay of motor commands arising in cortex (see Figure 1.1 (a) for diagram). As a result, PD is often characterized as a dynamical pathology.

There is no known cure for PD and medical intervention is generally aimed at treating symptoms. While most common treatments are pharmaceutical in nature, neurosurgical procedures are often used to treat patients with advanced PD for which drugs are no longer effective. Despite a limited understanding of the electro-physiological properties of BG, surgical interventions have proven successful and fall in two main categories: lesions and stimulation. Lesions essentially amount to removing parts of neural nuclei to mitigate pathological activity and are only rarely used in modern treatments. Stimulation procedures, better known as *deep brain stimulation* (DBS), consist of implanting an electrode in the brain designed to deliver electrical impulses,

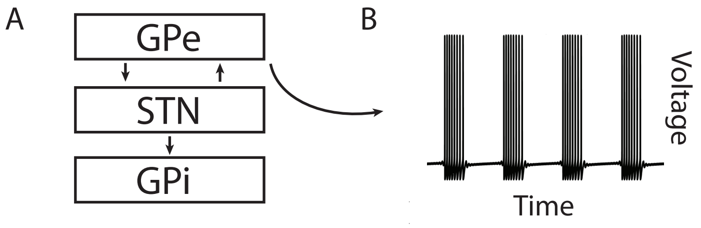

Figure 1.1: (a) Simple diagram of connectivity in the *basal ganglia* subnetwork composed of *subthalamic nucleus* (STN), *globus pallidus externa* (GPe) and *interna* (GPi). (b) Simulated voltage trace of an *elliptic bursting* neuron.

with the aim of perturbing neural dynamics out of pathological states. Such neural prosthetics are often referred to as "brain pacemakers" and are increasingly used as a modern medical treatment for PD [84, 48] and other disorders (see e.g. [112]).

Clinical success of DBS along with increasingly efficient prosthetic technologies have triggered an increased interest in theoretical studies aimed at understanding the dynamical principles underlying PD and ways to optimize DBS (see e.g. [83, 111, 132, 121, 25]). Among these efforts, Rubin, Terman,Yu and Wilson developed an influential biophysically detailed mathematical model of key circuits in BG [124]. This model is composed of many coupled ordinary differential equations (ODEs) capturing experimentally measured attributes of several cell types throughout BG. It successfully reproduces key dynamical changes from normal to PD regimes and has been used to investigate dynamical mechanisms involving DBS in many subsequent studies [98, 36, 37, 11].

Central features of PD dynamics reproduced by the Terman *et al.* model are the synchronization of STN, GPe and GPi neurons [82] as well as a shift of GPe neurons from an excitable to a bursting regime [47]. Bursting refers to periodic electrical activity of neurons that alternates between periods of quiescence and of repetitive firing of action potentials [106, 55] (see Figure 1.1 (b)). For GPe neurons, PD bursting is believed to arise from a dynamical interaction of mechanisms with distinct time-scales, also called “slow/fast” dynamics, and is modeled as such in [124]. Indeed, the interaction of the “slow” calcium dynamics with other “fast” ionic currents periodically steers the GPe neurons’ membrane potentials between quiescence and repetitive spiking. Mathematically, the onset of the spiking phase is due to a sub-critical Hopf bifurcation of the fast dynamics, and the termination of this burst of spikes follows from a saddle-node bifurcation of invariant circles. This type of bursting is typically referred to as *elliptic bursting* [57] and plays a central role in the synchronization of the STN-GPe-GPi subnetwork of BG [11].

Generally, PD DBS targets the STN with high frequency and high intensity signals to fight pathological synchrony found in this subnetwork. However, there is evidence that stimulating GPe or GPi can yield very good therapeutic results [61]. Bursting systems such as GPe neurons have intrinsic instabilities stemming from their slow/fast dynamics that could be exploited by external signals such as DBS inputs. While many studies have dealt with the synchronization of elliptic bursters [2, 58], little is known about their response to periodic pulsatile inputs.

Chapter 2 of this dissertation presents a detailed analysis of an uncoupled population of elliptic bursters subject to such inputs. The goal is to derive the best class of driving signals to desynchronize a population of identical neurons of this type. As GPe neurons have very weak lateral coupling in BG (see [124] and references therein), this serves as a first step toward a network stimulation paradigm. Moreover, GPe neurons are entrained into synchrony by a common synchronized input from STN neurons, which are themselves coupled to GPe. DBS inputs to GPe should thus be able to compete with another entraining input if they are to be effective in this network setting. This question is also treated in Chapter 2. In more detail, the analysis there is developed for a simplified normal-form model of elliptic bursting [57] and employs slow/fast decomposition techniques to develop a discrete dynamical system capturing the effect of pulsatile inputs on a neural population. It is shown that certain input amplitudes and frequencies can lead to a successful desynchronization of model neurons, while others lead to synchrony via entrainment. This mechanism is also found to be robust to moderate amounts of noise. Finally, a direct numerical verification of the validity of these results for the biophysically based model of GPe neurons of [124] is presented.

1.2 Reliability and encoding in driven balanced networks

Beyond artificial neural stimulation, the concept of "driven" neurons naturally arises from the brain's primary function: to encode and process information about an animal's environment and produce appropriate behavioral responses. Sensory pathways such as visual and auditory systems have a clear role to play: to relay stimuli such as light or sound patterns to the brain so that information about the world can be processed. However, the function of higher brain areas responsible for this information processing can be considerably more complex, as are their architecture and dynamics. Understanding the nature of the "neural code," which dictates the behavior of interacting neurons in order to achieve tasks, is one of the most important problems in modern computational neuroscience. As neurons primarily interact with one another via spikes, the features of evoked spike trains relevant to information processing are not well understood. Whether the brain makes use of the precise timing of spikes or only relies on coarser statistics such as firing rates over longer time periods is still unknown in many contexts, and likely depends on both input attributes and network architecture.

Neurons typically have unidirectional connections called *synapses*. When a presynaptic (upstream) neuron fires a spike, it either increases or decreases the likelihood of its postsynaptic (downstream) neuron to fire a spike of its own. Which of these two outcomes follows a presynaptic spike generally depends on whether the synapse is *excitatory* or *inhibitory*, an attribute typically determined by presynaptic cell type. As there are myriad neuron types and connectivity architectures throughout the brain, features of neural activity relevant for coding are likely to vary from one brain area to the next. Nevertheless, some stereotypical attributes are found across a collection of neuronal networks responsible for higher order function called the *cerebral cortex*. There are approximately 20 billion neurons in the human cortex, roughly 20% of which are inhibitory while 80% are excitatory. They are arranged in interacting subnetworks which are typically sparsely connected with a recurrent architecture promoting a balance between excitatory and inhibitory incoming synapses to each cell. This results in a sustained, seemingly random spiking activity (see Figure 1.2 (a)) with a wide range of mean firing rates across neurons [116]. What kind of neural code can be supported by such complex neural activity is a daunting question and calls for a better theoretical understanding of large recurrently connected networks.

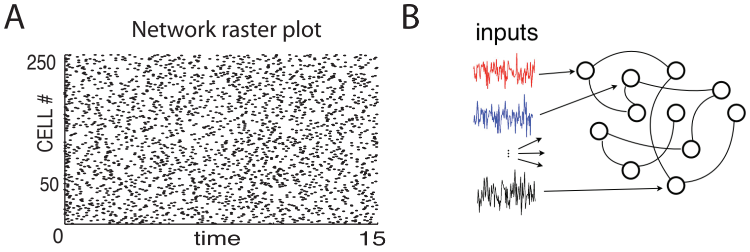

Figure 1.2: (a) Simulated network *raster plot* showing the spiking activity of 250 neurons. Abscissa represents time while ordinates show cell number; each dot shows a spike time for corresponding cell. (b) Cartoon diagram of a driven balanced network. Neurons are sparsely connected and each receive independent, fluctuating input.

In their seminal work, Van Vreeswijk and Sompolinski developed a simplified mathematical model called the *balanced state network* [129] that successfully captures many experimentally observed features of cortical networks, such as a balance between excitation and inhibition and sustained irregular activity. The original model is composed of a large number N of binary threshold neurons, separated in inhibitory and excitatory populations and connected randomly so that that on average, each neuron receives K incoming synapses from neurons in each population. In addition, neurons from each population are given a constant excitatory drive so that they would periodically fire were they disconnected from the network. Provided that $K \ll N$ and the strength of synapses are $\mathcal{O}(1/\sqrt{K})$, it was found that networks are self-tuning as they settle into a stable, irregular spiking state with constant mean firing rate. This firing rate continuously depends on the constant excitatory drive to each population, and it was shown that networks can track a sudden change in these constant inputs on timescales orders of magnitude faster than the time-constant of a single neuron.

1.2.1 Chaos and spike-time reliability

Balanced state networks inspired a great number of subsequent studies, and their fundamental architecture is now ubiquitous throughout models of cortical dynamics. As was demonstrated originally [129] and in several related contexts [6, 72, 130, 87], balanced networks are chaotic systems and thus, are extremely sensitive to small perturbations. This suggests that very small changes in the initial state of a network or the presence of intrinsic noise may lead to widely different spiking patterns. As a result, it has been suggested that cortex might only support firing rate based codes [79]. However, most studies involving balanced networks rely on a constant external source of excitation to maintain spiking activity (see e.g. [129, 87]). Such a simplification does not account for fast temporal features that may be present in inputs driving cortical networks. Moreover, experimental studies suggest that while there is variability in cortical activity, some neurons fire very precisely timed spikes when an animal is presented with temporally fluctuating sensory stimuli on repeated trials [63, 134]. How pronounced is the effect of temporal inputs on the reliability of balanced networks is not well understood.

Chapter 3 of this dissertation contains a detailed study of temporally driven balanced networks (see diagram in Figure 1.2 (b)). Inputs are modeled as rapidly fluctuating signals and the question of spike time reliability is investigated. Here, reliability refers to the repeatability of spikes if the network is driven by the same input on many trials where the initial network state is changed. Building on [87], we use the θ-neuron model [33] to represent the dynamics of single cells. Here, the state of each neuron is described by a phase variable $\theta \in S^1 = \mathbb{R}/\mathbb{Z}$ and obeys the differential equation

$$\dot{\theta} = 1 + \cos(2\pi\theta) + [1 - \cos(2\pi\theta)][\eta + \text{inputs}]. \tag{1.1}$$

We say a spike is fired when $\theta = 1 \sim 0$. In Chapters 3 and 4, the "inputs" term will contain synaptic interactions from other neurons in the network as well as a temporally varying input signal. Equation 1.1 is based on the normal form of Type I excitability [33], the primary spike-generating mechanism found in cortical neurons. The parameter η controls the degree of excitability: When $\eta < 0$, the neuron is said to be *excitable* and 1.1 contains one stable and one unstable fixed point, together representing rest and threshold potentials. When $\eta > 0$, the neuron becomes oscillatory with frequency that grows as $\sqrt{\eta}$.

Chapter 3 shows that when driven networks are in the excitable regimes, chaotic dynamics persist but the dimension of underlying chaotic attractors is very limited. As a result, evoked spikes have varying degrees of reliability and a majority are perfectly repeated from trial to trial. Random dynamical systems theory, as well as large scale numerical simulations, are used to formulate geometrical arguments leading to this result.

1.2.2 Dynamical origins of spike train noise entropy

If a network is to encode information using temporal patterns of spikes, a limiting factor is the trial-to-trial variability of stimulus-induced spike trains. Beyond the isolated spike reliability described in Chapter 3, what matters here is the activity of all neurons in driven networks over extended periods of time. More precisely, it is crucial to understand how "noisy" joint network spike patterns are in response to stimuli. The variability of interacting neurons has been the subject of many theoretical studies using probabilistic models such as *generalized linear-nonlinear models* (GLM) [97, 93, 92] and *maximum entropy models* [113, 126, 136]. However, little is known about the link between dynamical properties of neural networks and the variability they produce.

Probabilistic tools give a way of quantifying this variability. Specifically, if S denotes a random variable over the space of all network spike outputs and I is a stimulus, then $P(S|I)$ is the conditional probability of observing S in response to I. How much variability one can expect from this input/output relationship is captured by the conditional *noise entropy*:

$$H_{noise} = -\sum_S P(S|I) \log_2 P(S|I).$$

This is one key term that affects the amount of information that S may contain about I (see e.g. [102]). H_{noise} can sometimes be directly estimated for single neurons using large data sets from experiments or simulations [118]. The idea here is to estimate probability distributions of spike patterns by sampling from the data. However, such direct methods quickly fail at capturing the joint noise entropy of groups of more than a few cells, since the size of the space to sample grows exponentially with the number of neurons.

Chapter 4 establishes a relationship between chaos-induced variability in network spike output and the resulting noise entropy. This entropy, defined in a probabilistic setting, can be bounded by the dynamical entropy production of this chaotic system. This correspondence suggests surprising and complex dependencies between neurons that may lead to lower noise entropy than estimated by considering limited interactions between neurons. Finally, this result is used to show that the temporal features in an input, such as mean and variance, may directly influence the level of chaos-induced noise in network spike trains. This is a phenomenon that has strong implications for temporal neural coding.

1.3 Summary

Temporally driven systems are ubiquitous throughout the field of computational neuroscience, and beyond. A better theoretical understanding of them is crucial if we are to develop a mathematical theory of brain function. However, such systems produce challenging mathematical problems, especially in high dimensions. In this dissertation, results that build toward the development of neural prosthetics as well as a theory of encoding mechanisms by large networks are presented.

Chapter 2 treats the dynamics of a population of bursting neurons in response to periodic, pulsatile inputs. Specific attributes of such driving signals are derived to maximize the desynchronization of neural populations. This is motivated by the contemporary question of optimizing a therapeutic procedure named *deep brain stimulation*, which is used as treatment for Parkinson's Disease.

Chapters 3 and 4 present results concerning dynamics of temporally driven *balanced state* networks. Properties of chaotic attractors underlying input-evoked spiking activity are derived, and reveal surprising levels of trial-to-trial spike-time reliability. Furthermore, the joint activity of all neurons in a network are studied. Their input-conditioned *noise entropy* is approximated with tools from dynamical systems theory which provide a novel and surprising view of spiking statistics. These results have important implications for the possible neural encoding mechanisms implemented by large recurrent networks of neurons in the brain.

Chapter 2

SHARED INPUTS, ENTRAINMENT, AND DESYNCHRONY IN ELLIPTIC BURSTERS: FROM SLOW PASSAGE TO DISCONTINUOUS CIRCLE MAPS

2.1 Overview

What input signals will lead to synchrony vs. desynchrony in a group of biological oscillators? This question connects with both classical dynamical systems analyses of entrainment and phase locking and with emerging studies of stimulation patterns for controlling neural network activity. Here, we focus on the response of a population of uncoupled, elliptically bursting neurons to a common pulsatile input. We extend a phase reduction from the literature to capture inputs of varied strength, leading to a circle map with discontinuities of various orders. In a combined analytical and numerical approach, we apply our results to both a normal form model for elliptic bursting and to a biophysically-based neuron model from the basal ganglia. We find that, depending on the period and amplitude of inputs, the response can either appear chaotic (with provably positive Lyaponov exponent for the associated circle maps), or periodic with a broad range of phase-locked periods. Throughout, we discuss the critical underlying mechanisms, including slow-passage effects through Hopf bifurcation, the role and origin of discontinuities, and the impact of noise.

The contents of this chapter are taken in part from a manuscript published in the SIAM Journal of Applied Dynamical Systems entitled *Shared Inputs, Entrainment, and Desynchrony in Elliptic Bursters: From Slow Passage to Discontinuous Circle Maps*, by Guillaume Lajoie and Eric Shea-Brown [70]. Special thanks go to Jonathan

Rubin, David Terman, Pablo G. Barrientos, Artem Raibekas, and Joshua Goldwyn for helpful discussions and insights. This research was supported by NSF grant DMS-0817649, by a NSERC Graduate Fellowship (to G.L.) and by a Career Award at the Scientific Interface from the Burroughs-Wellcome Fund (to E.S.-B.).

2.2 Introduction

Many types of physical and biological systems exhibit intrinsic bursting – rapid discharges of consecutive, fast dynamical events separated by periods of quiescence. In particular, bursting neurons serve myriad functions in the nervous system; prominent among these is their role in central pattern generators that create rhythmic neural activity [19, 24, 115, 21]. Bursting dynamics is also a feature in pathological oscillations associated with disease conditions, as for basal ganglia networks in Parkinsons disease [98, 124, 11, 2, 58], where elevated synchrony and rhythmicity among neurons are linked to motor symptoms.

Here, we focus on synchrony and desynchrony among bursting neurons in the simplest possible setting: a population of uncoupled bursting neurons receiving a common input signal. We study elliptic bursters [57, 103] – that is, non-linear oscillators with fast and slow variables, and for which burst onset is caused by passage through a (subcritical) Hopf bifurcation in the fast subsystem and burst offset follows from a saddle-node bifurcation of limit cycles (see Sect. 2.3 below). The driving signals are periodic pulsatile inputs.

We find that there is rich variety in the response to these inputs, depending on their strength and frequency. An illustrative example is presented in Fig. 2.1, where we plot simulated voltage traces of two bursting cells, both receiving a common pulsatile input $I(t)$. In the left panel, the cells' bursting phases are initially well separated, but a pair of "strong" input pulses synchronizes them. In the right panel, the cells' phases are initially nearly synchronized, but a relatively "weak" input drives them apart. As we will show, the outcome depends on pulse strength and on inter-pulse timing in interesting ways that arise directly from the dynamics of elliptic bursting.

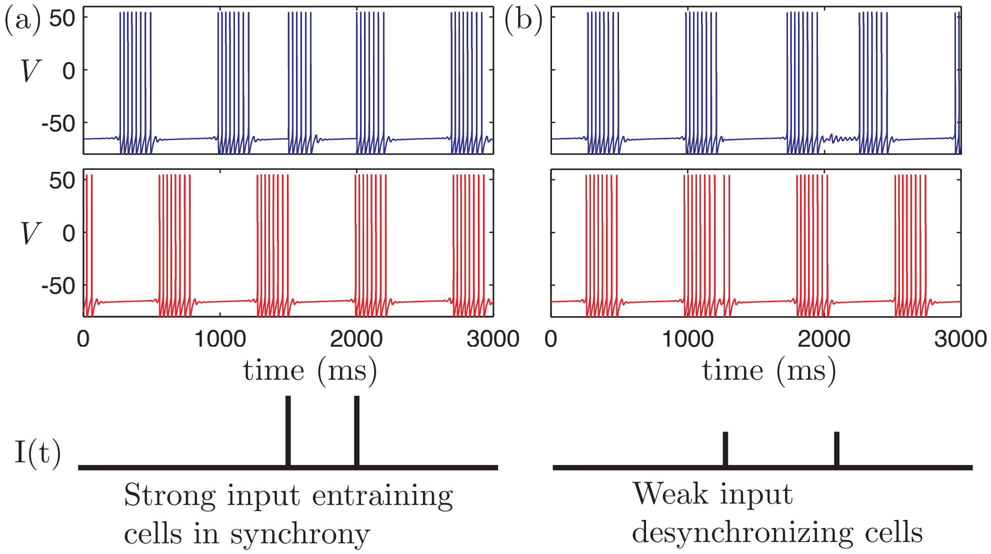

Figure 2.1: Simulated voltage traces of two uncoupled cells receiving common inputs (from the conductance-based neuron model of Eqn. (2.38); see Sect. 2.6). (a) A strong input synchronizes cells that are initially out of phase. (b) A weak input desynchronizes cells with close by initial phases.

Our goal is to understand the mechanisms responsible for this and related phenomena. Specifically, we ask whether or not cells will entrain or become separated under the driving effect of a common periodic input signal. Our main goal is to develop and explain a general answer to this question. We note two broad scientific motivations for doing so, although exploring the implications of our results for each largely remains for future work. First, entrainment of a population of uncoupled cells to an input signal determines the “reliability” of a neuron’s response – that is, the repeatability of a response to a fixed input signal on multiple trials in which the neuron is in a different initial condition. Reliability is fundamental in understanding how neural dynamics encode, e.g., sensory signals [16, 80, 54, 96, 75, 5]. Second, common input signals to populations of bursting cells (of elliptic and other types) occur naturally in layered neural networks, as in the basal ganglia; in this brain area, common, pulsatile electrical stimuli are also artificially applied as a therapy for Parkinson's disease [98, 124, 11]. We give a very brief application to this general setting in Sect. 2.7.

Throughout this chapter, we use a normal form model for elliptic bursting developed by Izhikevich [57]. It is the simplest system that captures the dynamical features of elliptic bursting and we show that it accurately describes a more complex bursting neuron model derived from basal ganglia physiology. Thus, we will often refer to the *normal form model* as describing a "cell."

Building from, e.g. [11], we show that the dynamics of the normal form model under periodic, pulsatile inputs admits an accurate reduction to a discontinuous circle map that can be analytically defined. This map forms the basis for our theoretical results, and correctly predicts synchrony and desynchrony for the physiological model. Nevertheless, because our results are linked to the normal form model, we note that our approach and results have potential applications in the study of general slow/fast oscillators undergoing a delayed bifurcation, well beyond neuroscience.

The chapter proceeds as follows. Section 2.3 deals with the analysis of elliptic bursting dynamics as well as phase reduction to a discrete dynamical system on the circle. Section 2.4 presents an analysis of the reduced dynamics and explores synchronizing and desynchronizing effects of common pulsatile inputs. Next, in Section 2.5, we study the effect of noise, which has a non-trivial and interesting impact on the circle map and resulting patterns of synchrony. In Section 2.6, we carry out a series of numerical experiments that verify our reduced models. Finally, in Section 2.7, we show how the circle map framework can be used to analyze the effect of multiple sequences of pulsatile inputs. As a proof of concept, we present a brief example in which an input signal is designed to compete with the effect of a global entraining drive synchronizing a population, as in the basal ganglia setting described above. *Our principal finding – unifying analyses of several models and settings – is that a population of (elliptic) bursting cells will desynchronize in the presence of weak* *to moderately strong common inputs, if these inputs have a frequency slightly slower than the natural burst frequency.*

2.3 Geometry of forced elliptic bursters

In order to better understand the effect of a common stimulus on a population of bursters, we first describe the dynamics of single cells. Dynamical models that capture bursting usually include multiple timescales and are often called *slow/fast* systems. Indeed, most intrinsically bursting solutions arise from the evolution of one or more *slow* variables that periodically steer *fast* variables into distinct dynamical regimes – here, spiking and resting.

2.3.1 Timescale dissection and basic model

Slow/fast systems can be written in the form

$$\begin{aligned} \dot{z} &= f(z, y, \varepsilon) \\ \dot{y} &= \varepsilon g(z, y, \varepsilon) \end{aligned} \tag{2.1}$$

where z is a vector of *fast* variables, y is a vector of *slow* variables and ε is the slow/fast timescale ratio. Such systems arise in many areas of mathematical modeling and can describe general multiple timescale phenomena. In the singular limit, where $\varepsilon \to 0$, one obtains an equation where the slow variable(s) y can be considered as parameter(s) for the fast subsystem (z). This approach allows one to investigate the dynamics of the fast subsystem and subsequently to construct solutions of the full system by carefully reintroducing slow dynamics – i.e., by studying the perturbed system ($\varepsilon \neq 0$). An elegant mathematical toolset known as geometric singular perturbation theory has been developed to study such phenomena [23, 62].

The results brought forward in this chapter relate to the effect of pulsatile perturbations on slow/fast bursters in which a delayed Hopf bifurcation is central to the onset of rapidly varying dynamics. One of the first systems of this type to be studied was a bursting phenomenon in the Belousov-Zhabotinskii chemical reaction [105]. The mechanisms central to our study can be found in many chemical, physical and biological systems.

However, our main purpose is to better understand the effect of perturbations on conductance based models of single neurons (i.e., models of Hodgkin-Huxley type) that possess such a separation of timescales. In many cases, calcium concentration acts as a slow variable while voltage and associated ionic currents evolve on the fast timescale. Rinzel and Lee first studied fast/slow solutions to models of parabolic bursters in 1987 using singular perturbation methods [104]. Since then, much effort has been invested in understanding bursting solutions arising in conductance-based neural models and their reduced forms [122, 103]. In 2000, Izhikevich produced a classification of bursting mechanisms [55], including all of the possible codimension one bifurcations of the fast subsystem that could be responsible for the onset and termination of spiking dynamics.

We concentrate on cells characterized as (subcritical) elliptic bursters or type III bursters, in which a subcritical Hopf bifurcation of the fast subsystem drives the onset of bursting and a saddle node bifurcation of limit cycles is responsible for the return to silent state (see Fig. 2.2). This type of intrinsic bursting is well understood in the absence of forcing (input). In particular, Su, Rubin and Terman established existence and stability properties of elliptic bursting solutions in [120]. Izhikevich [57] presented a portrait of elliptic bursting dynamics by describing the fast subsystem via the normal form of the (codimension two) Bautin bifurcation, and derived a closely-related model of weakly coupled networks of these bursters [58]. Throughout this chapter, we keep our analysis as general as possible and often illustrate our results with a variation of Izhikevich's *normal form model* (see Eqn.(2.2)) to simplify mathematical manipulations. However, we stress that our analysis can be carried out for any elliptically bursting model.

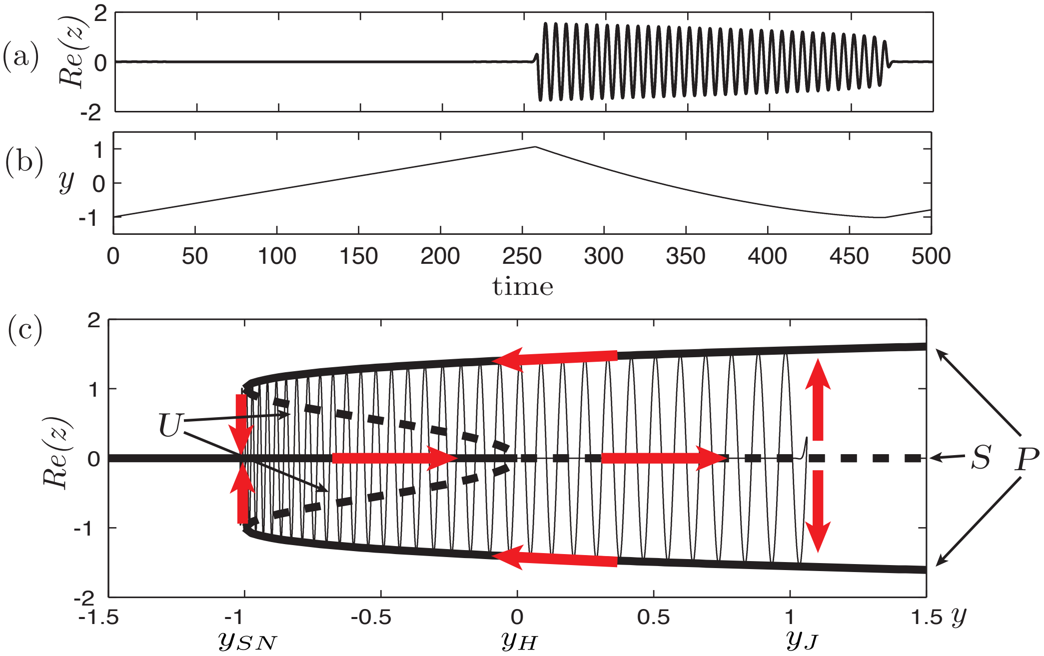

Figure 2.2: Elliptic bursting trajectory from model (2.2). (a) Trace of $Re(z)$. (b) Trace of y. (c) Projected into the $(Re(z),\ y)$ plane, thicker black lines show y-parametrized fixed points and limit cycles of the fast subsystem (i.e., from the singular limit). S is a family of fixed points (stable for the solid line and unstable for dashed), U is a family of unstable orbits and P is a family of stable orbits. Thin black line shows bursting trajectory, with red arrows indicating time evolution direction.

The *normal form model* is

$$\begin{aligned} \dot{z} &= (y + iw)z + 2z|z|^2 - z|z|^4 + I(t) \\ \dot{y} &= \varepsilon(a - |z|^2 - by) \end{aligned} \tag{2.2}$$

where $z \in \mathbb{C}$ represents the fast variable and $y \in \mathbb{R}$ the slow variable. This is as found in [58], but with the term by added to the slow variable dynamics in order to explore the effect or nonlinear ramping in the delayed Hopf bifurcation, a feature that is found in many models for which bursting dynamics are caused by slowly varying calcium concentration. We set $w = 1$ and $\varepsilon = 0.01$ for the remainder of the chapter and will consider distinct cases in which we vary a and b. Intrinsically bursting solutions generally arise for parameter choices where $\dot{y}$ is positive when z is at rest and negative when z is spiking (oscillating).

Notice the forcing via the signal $I(t)$ in the equation for the fast variable. We wish to model an input signal that causes an instantaneous voltage response, so we set $I(t) = \sum_n A_n \delta(t - t_n)$ where δ is a delta function and $A_n \in \mathbb{R}^+$. We will refer to these perturbations as *t_n-kicks* of *amplitude* A_n: a kick simply translates a solution at time t_n by an amount A_n in the real "direction" of z. In this chapter, we focus on periodic kicks of fixed amplitude $A = A_n$ and equal spacing $\tau = t_n - t_{n-1}$ between kick times.

2.3.2 The elliptic bursting cycle

Figure 2.2 shows an elliptic bursting trajectory from numerically integrating Eqn. (2.2) with $a = 0.8$ and $b = 0$. As mentioned above, the standard approach is to think of the slow variable y as a parameter that determines the fast dynamics (z). The fast subsystem undergoes a subcritical Hopf bifurcation at $y_H = 0$ and a saddle-node of limit cycle bifurcations at $y_{SN} = -1$. When $\varepsilon = 0$, and given a fixed $y \in (y_{SN}, y_H)$, the fast subsystem is bistable and has a sink at $z = 0$ inside an unstable periodic orbit, itself contained within a stable periodic orbit. These y-parametrized limit sets form normally hyperbolic invariant manifolds that persist under small perturbations ($1 >> \varepsilon > 0$) [120]. We denote by S the family of equilibria ($z = 0$). These are stable when y lies to the left of y_H and unstable on the right, together forming the *silent* branch. P is the family of stable periodic orbits and represents the *spiking* branch. For Eqn.(2.2), the radii of these orbits about S are given by $r_P(y) = \sqrt{1 + \sqrt{y+1}}$ for $y > y_{SN}$. Finally, U refers to the family of unstable orbits with radii $r_U(y) = \sqrt{1 - \sqrt{y+1}}$ for $y \in (y_{SN}, y_H)$, acting as a separatrix between the stable side of S and P. A bursting solution occurs when the slow dynamics of y steer the fast subsystem rightward along the silent branch S, until the Hopf point y_H is reached.

The solution then keeps moving rightward, sticking close to S for some transient period even though the equilibria forming S are now unstable, but is eventually attracted to P when y reaches y_J, where spiking begins. The y dynamics then pull the oscillating fast subsystem leftward along P, until the latter vanishes at y_{SN}, where the solution is attracted back to S and another cycle begins.

Of particular interest is the *slow passage effect* through the Hopf point y_H, in which the solution does not immediately jump up into spiking when S loses stability ($y_J \neq y_H$). This delayed bifurcation phenomenon has been previously studied [4, 3, 120] and its implications in the context of pulsatile perturbations will be established in Sect. 2.3.4. Importantly, several authors have shown that noise can sharply diminish this slow passage effect [69, 68, 3, 120]. While we first treat the noiseless case, we study the effect of stochastic terms on the phase reduction and response dynamics in Sect. 2.5.

2.3.3 Phase reduction

There is a substantial body of literature concerning phase reduction of oscillators and their behavior under noise, forcing, or coupling [35, 59, 15, 22, 43, 88, 123, 34]. The general idea is simply to associate the endpoints of a periodic solution's cycle and to parametrize the movement along this solution with a phase $\theta \in S^1$. Although the point $\theta = 0$ is arbitrary, it is often chosen to correspond to a distinguishable event within the periodic orbit, such as the apex of an action potential in a model of a spiking cell. This reduction becomes useful when the limit cycle has some stability properties and one can track the phase response of the solution following a perturbation: specifically, by computing the phase difference on S^1 between the unperturbed solution and the perturbed one, as $t \to \infty$ and the latter contracts back to the limit cycle. When well defined, this one-dimensional description has the advantage of being analytically tractable while preserving the behavior of an oscillator subject to perturbations.

For systems with asymptotically stable limit cycles, phase reduction can be carried out rigorously as long as the effect of forcing translates the solution to a point in the cycle's basin of attraction. This basin is foliated by the strong stable manifolds of each point on the limit cycle. By knowing on which manifold – or *isochron* – the solution lands following a perturbation, we know exactly to which phase it will be attracted in the limit as $t \to \infty$ [35, 133, 46, 85, 22, 56].

We next describe a phase reduction for elliptic bursters. As we will discuss further, the bursting trajectories are not stable limit cycles, and so we cannot directly compute isochrons. Nevertheless, the difference between the timescale of the burst period and the timescale of attraction normal to the (singular limit) solution enables us to proceed. We closely follow Best et al. [11], who derive circle dynamics for an elliptic burster receiving periodic inputs from a model excitatory neuron. In their work, each excitatory kick always transitions a solution from the resting to the spiking state – i.e., to the branch of periodic orbits P in Fig. 2.2, if it is not already following that branch. Best et al. also use an approximation of linearity for the slow trajectories (i.e., $\dot{y}$ is piecewise constant). Here, we relax both of these assumptions, in particular while studying the response to weaker kicks that do not necessarily generate a burst. As we will see, it is these weaker kicks that will lead to desynchrony; that is, dynamics that appear chaotic or are phase locked at high period.

In [120], the authors use Fenichel theory to show that there exist $O(\varepsilon)$ neighborhoods N_S and N_P around S and P such that – if a solution enters either the left side of N_S or the right side of N_P and the slow dynamics behave as mentioned above – then the solution will transition between the two neighborhoods in a periodic, bursting fashion. Furthermore, they use averaging techniques to show that the period of such a cycle can be approximated up to $O(\varepsilon)$ by the sum of the passage times T_S and T_P along the respective manifolds.

Although it is not clear whether or not there exists a single periodic solution of the full system, [120] shows that such dynamics are at least metastable. That is,

N_S and N_P are locally attracting and any bursting solutions must live in these sets. Furthermore, solutions starting outside the two attracting sets are quickly attracted back to them.

Numerically obtained solutions of Eqn. (2.2) do not trace back exactly the same path from cycle to cycle but have periods that vary minimally, as expected [120]. Specifically, we numerically integrated a solution in order to obtain 150 burst cycles and computed the coefficient of variation ($CV = \frac{\text{standard deviation}}{\text{mean}}$) of the cycle durations. We found $CV = O(10^{-3})$ for parameter choices yielding a bursting solution in Eqn. (2.2) (numerical methods as in Sect. 2.6). Whether there is a periodic solution with a much longer period than the bursting cycle, or whether solutions are instead quasiperiodic or aperiodic remains an open question.

The small CV (indicating a robust cycle period), along with the metastability described above, motivate an approximate reduction to dynamics on the circle, as in [11]. We will revisit the notion of uncertainty in cycle periods in Sect. 2.5. However, for what follows, we use the singular limit assumption that a bursting trajectory evolves along S and P with well defined passage times T_S and T_P, and will use this trajectory to compute phase reduced dynamics.

As illustrated in Fig. 2.3, we represent bursting solutions by a phase variable $\theta(t) \in S^1 = \mathbb{R}/\mathbb{Z}$. We let $\theta = 0 \simeq 1$ correspond to the "jump down point" on the bursting trajectory, where solutions transfer from spiking to resting. We choose this reference point because the spiking to resting transition is fast and is associated with a constant value of the slow variable, $y = y_{SN}$ (unlike, as we will see, the transition to spiking following a pulsatile input). Essentially, the phase θ of a bursting cycle is given by time rescaled by the period ($\theta = \frac{t}{T_S + T_P}$) where at $t = 0$, $y = y_{SN}$. Note that the first portion of the unit circle following $\theta = 0$ represents the silent branch S and the remaining portion represents the spiking branch P.

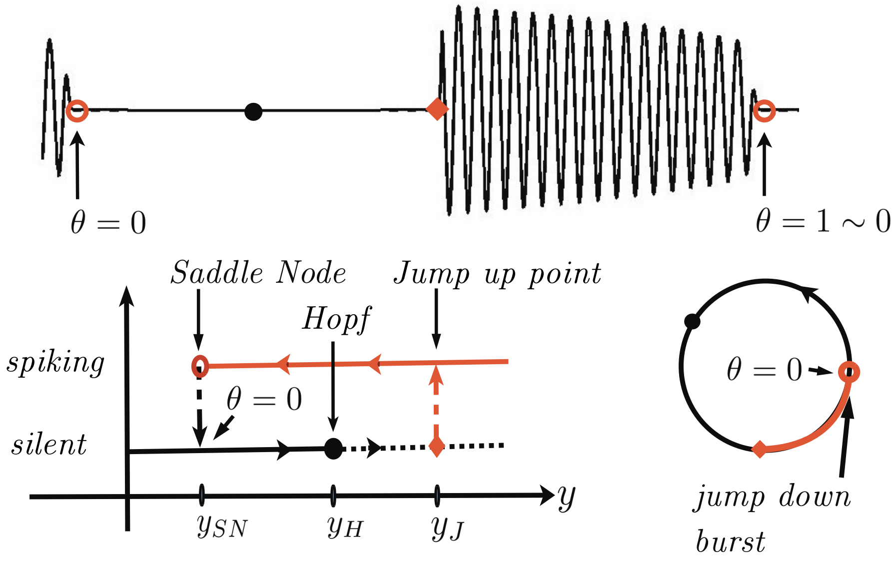

Figure 2.3: Schematic presentation of phase reduction. We associate endpoints of a bursting cycle (where $y = y_{SN}$), and map the trajectory onto the unit circle.

2.3.4 The kick map

We now study phase dynamics of bursters receiving pulsatile inputs (kicks). Specifically, we derive a phase translation mapping $F_A(\theta)$, such that if θ is the phase of a cell when a kick of strength A arrives, $F_A(\theta)$ is the phase of the kicked solution – relative to the unperturbed solution – after it relaxes back to the burst cycle. We will refer to this as the *kick map*. In [11], a similar map for elliptic bursters is derived, and this idea inspired the present work. However, there are two differences with the map we derive here. First, the phase of trajectories in [11] is defined relative to the period of pulsatile inputs; in our case, phase is defined relative to the (unperturbed) period of a burst trajectory. This latter construction has been previously used in the context of integrate and fire cells with soft reset [9], and we find that this makes it easier to visualize the role of changing kick amplitude and period on the structure of the map. Second, in [11], only “strong” kicks are considered; as we will see, the map develops additional features, including discontinuity and expansion, in the case of weaker kicks.

As discussed in Sect. 2.3.3, we assume that unperturbed elliptic bursting solutions have fixed times spent in silent (T_S) and spiking phases (T_P). When computing a map for a given system as done in Sect. 2.3.5, it is best to work with unscaled time and later (implicitly) normalize the time variable by the burst period ($T_S + T_P$) so that our phase variable θ remains between zero and one. In this section however, we derive the kick map for an arbitrary elliptic bursting model and assume that the period is already unitary ($T_S + T_P = 1$) for simplicity. The rest of the notation follows that of system (2.2) but the reader should keep in mind that z and y represent general fast and slow variables.

Our computations are intimately linked to the evolution of the slow variable y along the branches S and P. Recall that y spans $[y_{SN}, y_J]$ when z travels along S or P. To better track the variable y, we label its dynamics along S by $y(t) = h_S(t)$ and along P by $y(t) = h_P(t)$.

Thus, for a burst trajectory that starts at $y = y_{SN}$ when $t = 0$, we have

$$y(t) = \begin{cases} h_S(t) & \text{if } 0 \leq t < T_S \\ h_P(t) & \text{if } T_S \leq t < 1 \end{cases} \tag{2.3}$$

where $h_S(0) = y_{SN} = h_P(1)$ and $h_S(T_S) = y_J = h_P(T_S)$. Here, h_S and h_P are functions with ranges $[y_{SN}, y_J]$ and respective domains $[0, T_S]$ and $[T_S, 1]$. We assume h_S is an increasing function while h_P is decreasing. We now define the phase θ of a bursting solution $(z(t), y(t))$ by

$$\theta = \begin{cases} h_S^{-1}(y(t)) & \text{if silent } (z(t) \in S) \\ h_P^{-1}(y(t)) & \text{if spiking } (z(t) \in P). \end{cases} \tag{2.4}$$

For unperturbed solutions, $\theta = t \mod 1$. In general, expressions for h_S and h_P can be hard to find. As in standard approaches, one can integrate the dynamics of y by restricting the fast variable to the invariant manifolds S and P, and using the averaged motion of z on those manifolds [103, 34, 3, 120]. These calculations yield explicit formulas for the normal form system (2.2), as we demonstrate in Sect. 2.3.5.

We are now equipped to define the kick map. We proceed by stating a set of assumptions that will enable us to analytically define the map in a piecewise fashion. Our first assumption is that a kick which arrives during the spiking regime has no effect on $\theta(t)$. Due to the separation of timescales, trajectories are attracted back to the stable limit cycles that form P in a vanishingly short time (with respect to the timescale over which the phase evolves). Nevertheless, when a cell is spiking and $y \in (y_{SN}, y_H)$, it is possible that a kick of the correct strength will send the trajectory close to the stable branch and preemptively terminate a burst. However, due to geometry of the state space, such a scenario is rare, seldom being seen in numerical simulations (e.g., see Fig. 2.15 (d) in bottom right corner for isolated instances of such events). We therefore neglect this possibility in defining our maps.

On the other hand, a kick while the cell is silent (z near S) may have distinct outcomes. If $y(t) \in [y_H, y_J]$ (sticking to the unstable part of S), any kick will send the cell to the spiking state since the trajectory is highly sensitive to perturbations. However, if $y(t) \in [y_{SN}, y_H]$, one of two things can happen. If the kick is strong enough to translate the solution past the separatrix U, then the cell jumps to the spiking state (Fig. 2.4 (b)). If on the other hand, the kick is not strong enough, the solution will attract back to S (Fig. 2.4 (a)).

$$\theta_w(A) = h_S^{-1}(y_w(A)). \tag{2.5}$$

From now on, we refer to a kick as *strong* if $A > r_U(y)$ for all $y \in [y_{SN}, y_H]$ where, $r_U(y)$ is the distance between S and U at y, in the direction of the kick. In other words,

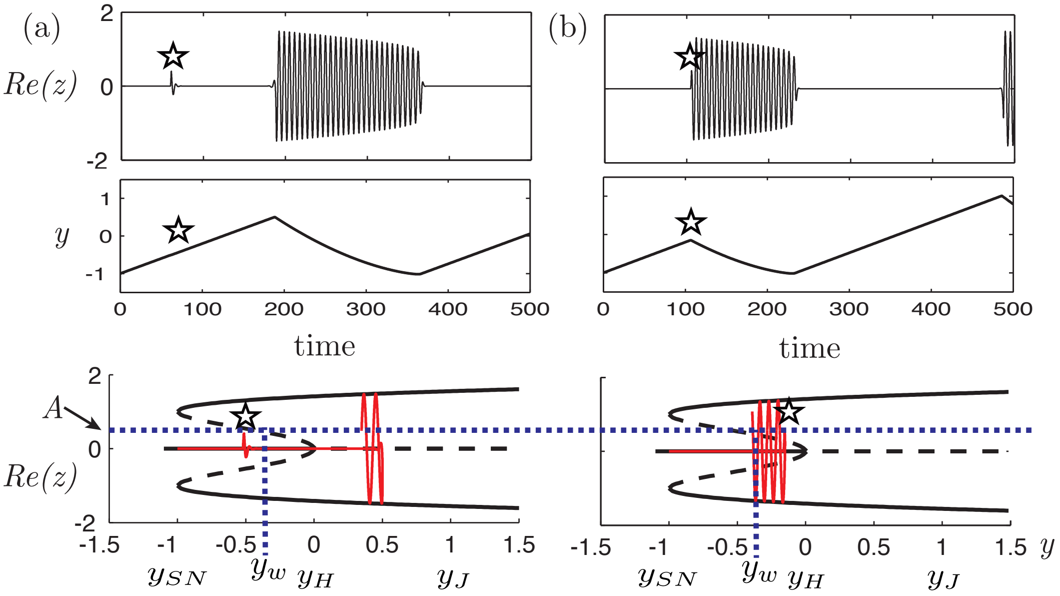

Figure 2.4: Weakly kicked ($A = 0.5$) trajectories from (2.2). Top to bottom: $Re(z)$ trace, y trace and $y - Re(z)$ solution curve (red) truncated at $t = 200$ for clarity. Star indicates a kick and dashed blue line the kick's amplitude A. (a) Kick received at $t = 80$ and does not clear separatrix. (b) Kick received at $t = 110$ and clears separatrix.

a strong kick will immediately result in spiking independently of the cell's phase. In contrast, we define a *weak* kick as one with an amplitude $A < r_U(y)$ for values of y in some subinterval of $[y_{SN}, y_H]$, so that the kick does not always immediately cause a cell to spike. However, we impose that a weak kick is such that $A > O(\varepsilon)$, so that it interacts strongly enough with trajectories to elicit spiking for any value of y outside this interval. As we will see, this condition is important due to slow passage effects through the Hopf bifurcation.

For the strong kick case, the kick map is

$$F_A(\theta) = \begin{cases} h_P^{-1} \circ h_S(\theta) & \text{if } \theta \in [0, T_S] \\ \theta & \text{if } \theta \in [T_S, 1]. \end{cases} \tag{2.6}$$

While in silent phase, $\theta \in [0, T_S]$, y increases according to $h_S(t)$; when spiking is induced by a kick, the value of y is left unchanged but its dynamics are "reversed" and it starts decreasing via $h_P(t)$. The cell will then spike until y reaches y_{SN}, which takes less time since we started closer y_{SN}. Thus the impact of the kick is to advance the phase. This explains the first line of Eqn. (2.6), and is sketched in the panel (a) of Fig. 2.5. As already discussed, the kick has no effect when the cell is spiking, as expressed in the second line of Eqn. (2.6).

For weak kicks, the situation is more complex. Recall that the branches U and P meet at y_{SN} ($r_U(y_{SN}) = r_P(y_{SN})$), and U vanishes at y_H ($r_U(y_H) = 0$); we assume that r_U is a non-increasing, continuous function. As a result, for $r_U(y_{SN}) > A > 0$, we can find $y_w(A)$ such that $A = r_U(y_w(A))$ and $A < r_U(y)$ for all $y \in [y_{SN}, y_w(A)]$. If the cell is in silent phase, $y_w(A)$ is essentially a cutoff point before which a weak kick will not elicit immediate spiking, as illustrated in Fig. 2.4(a). A weak kick delivered at any other point through the burst cycle will result in instantaneous spiking, as in the strong kick case. We recast this condition in phase coordinates, obtaining the cutoff phase

What happens to a cell's phase when a weak kick does not evoke spiking ($\theta \in [0, \theta_w(A)]$)? The trajectory is attracted back toward S but jumps up into spiking before it reaches y_J, as if it retained a memory of this past weak kick (Fig. 2.4 (a)). To better understand this phenomenon, we first need expressions for slow passage times through Hopf points. We use results for delayed bifurcations derived in [4] in order to predict points of transition between silent and active states.

Let $\lambda(y)$ be the extremal eigenvalue of the fast subsystem linearized about the equilibrium points $z_0(y)$, for some chosen value of $y \in [y_{SN}, y_J]$. (Recall that this collection of points forms the manifold $S = \{z_0(y) | y \in [y_{SN}, y_J]\}$.) Points on S to the left of y_H are sinks with $Re(\lambda(y)) < 0$, whereas to the right, they are sources and $Re(\lambda(y)) > 0$. Assume $\frac{d\lambda(y)}{dy}|_{y=y_H} \neq 0$. As a solution is pulled to the right by the slow dynamics, y crosses y_H, $Re(\lambda(y))$ changes sign and solutions switch from being attracted to being repelled by S. However, this repulsion is not immediately apparent: the difference in time scales of our slow/fast system induces a discrepancy in spatial scales. As y varies, z is attracted to S for $y < y_H$ and repelled for $y > y_H$, both at an exponential rates (proportional to $Re(\lambda(y))$) on the fast timescale.

The length of the slow passage (also called delay) to the right of y_H depends on the dynamics of y along S. Borrowing notation from [4], suppose we can write

$$y(t) = y_i + g(\varepsilon t) \tag{2.7}$$

where we assume g is a non-decreasing function and $g(0) = 0$. In this context, $h_S(t) = y_{SN} + g(\varepsilon t)$. If the system's full solution starts at (z_i, y_i) such that $y_i \in [y_{SN}, y_H]$ and z_i is far enough from $z_0(y_i)$ but is still in its basin of attraction, then the jump up point y_j can be implicitly computed via

$$0 = \int_{y_i}^{y_j} (\frac{d}{dy} g^{-1}(y - y_i)) Re(\lambda(y)) dy \tag{2.8}$$

where g^{-1} is the inverse of g. In the unperturbed case, the point y_J can be derived using $y_i = y_{SN}$ in (2.8); this is sometimes called the memory effect for elliptic bursters [104]. We refer the reader to the appendix of [4] for the derivation of this integral condition.

If a weak kick does not elicit instantaneous spiking, we find that the "memory" starts anew at the time of the kick; in other words, if the kick is administered when $y \in [y_{SN}, y_w(A)]$, then we set $y_i = y$ in Eqn. (2.8), and denote the associated jump up point by $\tilde{y}_j(y)$. In phase coordinates, if the cell is kicked at $\theta \in [0, \theta_w(A)]$, y is given by $h_S(\theta)$. The onset of spiking happens at $y_j = \tilde{y}_j(h_S(\theta))$, or equivalently at

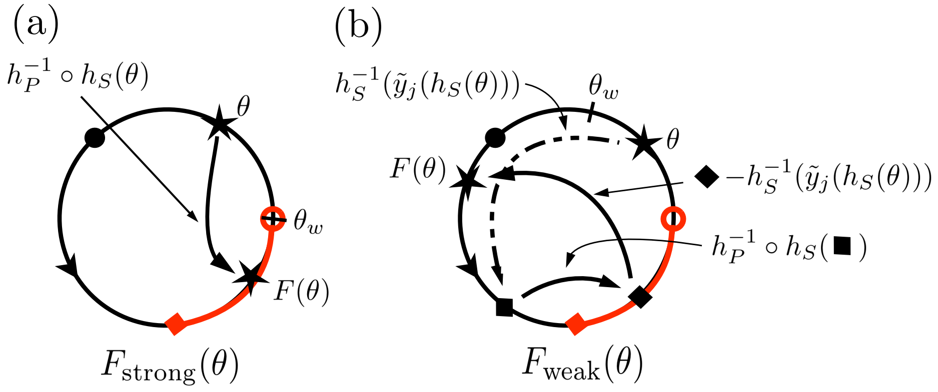

Figure 2.5: Schematic representation of the kick map $\theta \to F_A(\theta)$ on the unit circle. (a) Strong kick map (2.6). (b) Weak kick map of Eq. (2.9). The solid arrows represent instantaneous change of phase while the dotted arrow indicates the evolution of the phase along the circle in time.

$\theta_j = h_S^{-1}(\tilde{y}_j(h_S(\theta)))$. We capture this via:

$$F_A(\theta) = \begin{cases} \theta + h_P^{-1}(\tilde{y}_j(h_S(\theta))) - h_S^{-1}(\tilde{y}_j(h_S(\theta))) & \text{if } \theta \in [0, \theta_w(A)) \\ h_P^{-1} \circ h_S(\theta) & \text{if } \theta \in [\theta_w(A), T_S] \\ \theta & \text{if } \theta \in [T_S, 1]. \end{cases} \tag{2.9}$$

The first conditional definition maps the slow variable to its jump up value $y_j = \tilde{y}_j(h_S(\theta))$, and then applies the strong kick map $h_P^{-1} \circ h_S(\theta)$, and finally translates back by the phase $-h_S^{-1}(\tilde{y}_j(h_S(\theta)))$ to account for the time taken in "slow passage" from $y_i = h_S(\theta)$ to $y_j = \tilde{y}_j(h_S(\theta))$. This mapping is sketched in the right panel of Fig. 2.5; note that it is only valid if the cell does not receive additional kicks before it enters the spiking state.

This construction implies that the shape of a kick map does not vary continuously with the strength of a kick. Moreover, the only criterion which dictates the qualitative shape of the map is the value of $\theta_w(A)$ (we sometimes drop the A and write θ_w). Other than determining the threshold θ_w, the perturbative role of A is dimensionless since a kick acts on the fast variable as opposed to the phase which is defined over the slow timescale. That is, if two kicks of distinct amplitudes yield the same strong (resp. weak) outcome, the discrepancies between the times needed to attract close to the unperturbed trajectories are negligible. We emphasize that θ_w decreases as A increases: for strong kicks with $A > r_U(y_{SN})$, θ_w is always zero and the map does not change shape as A increases further. We use Eqn. (2.9) as the general expression for our kick map.

We stress that there is a fundamental difference between the maps induced by strong and weak kicks. A weak kick always induces expansion in the kick map, as long as it speeds passage ($\tilde{y}_j \neq y_J$) through the Hopf point. Indeed, notice that by construction, $h_P^{-1}(y) > h_S^{-1}(y)$ for any $y \in (y_{SN}, y_J)$ and $h_P^{-1}(y) = h_S^{-1}(y)$ when $y = y_{SN}, y_J$. From expression (2.9), we see that $F_A(\theta) > \theta$ on $(0, \theta_w)$ and $F_A(0) = 0$. It follows from the mean value theorem that $\frac{dF_A}{d\theta} > 1$ on some region contained in $[0, \theta_w)$. We also note that when h_P and h_S have similar shapes, it generally implies expansion of F_A on the whole interval $[0, \theta_w)$. To better illustrate this and other features, we compute expressions of this map for system (2.2).

2.3.5 Computing the kick map for the normal form model

In this section, we derive an analytical approximation of the kick map for the elliptic bursting normal form model. The task at hand is simple: use Eqn. (2.2) to compute the ingredients of expression (2.9): $h_S(\theta)$, $h_S^{(-1)}(\theta)$, $h_P^{-1}(\theta)$, $\tilde{y}_j(y)$ and $\theta_w(A)$.

We first turn to h_S and h_P, which are essentially the y components of a solution to Eqn. (2.2), in silent and spiking modes respectively. In contrast with the previous section, we carry out computations using unscaled time which implies a full burst period $T \neq 1$. One can still think of t as θ in what follows, but the expression of the final map has to be rescaled.

We exploit the separation of timescales in our equation and make the assumption, as in the singular limit, that z evolves exactly on the manifolds S and P. Notice that the y dynamics depend linearly on $|z|^2$. By substituting $|z|^2 = 0$ for h_S, and $|z|^2 = r_P(y)$ for h_P, we obtain two scalar O.D.E.s

$$\dot{y} = \varepsilon(a - by) \qquad \text{when } z \text{ is on } S \tag{2.10}$$

$$\dot{y} = \varepsilon(a - r_P(y)^2 - by) \qquad \text{when } z \text{ is on } P. \tag{2.11}$$

Bursting occurs when the right hand sides of (2.10) and (2.11) are respectively positive and negative, steering the fast dynamics in the required directions along S and P. Here we concentrate on parameter values $a > 0$ and $b \geq 0$ which satisfy this condition. As we will shortly see, $b > 0$ implies that the evolution of y along S follows a saturating exponential ramp while $b = 0$ implies a linear ramp. Both scenarios are found in biological systems, and – as we now show – the resulting kick maps have common characteristics which unify their response to pulsatile perturbations.

For Eqn. (2.10), we can easily solve and get

$$h_S(t) = \varepsilon at + C_S \qquad b = 0 \tag{2.12}$$

$$h_S(t) = \frac{a}{b} + C_S e^{-\varepsilon bt} \qquad b > 0 \tag{2.13}$$

where C_S is an integrating constant. Setting $y = y_{SN}(=-1)$ at $t = 0$, it is easy to see that $C_S = y_{SN}$ for $d = 0$ and $C_S = y_{SN} - \frac{a}{b}$ for $b > 0$. In turn, we have

$$h_S^{-1}(y) = \frac{y - y_{SN}}{\varepsilon a} \qquad b = 0 \tag{2.14}$$

$$h_S^{-1}(y) = -\frac{1}{\varepsilon b}\ln(\varepsilon[a - by]) + \frac{1}{\varepsilon b}\ln(\varepsilon[a - by_{SN}]) \qquad b > 0. \tag{2.15}$$

For Eqn. (2.11), recall that $r_P(y) = \sqrt{1 + \sqrt{y+1}}$ when $y > y_{SN}$. Solving this O.D.E. is not as straightforward; fortunately, we only need the inverse h_P^{-1} (which is a proxy for t in this context) to compute our map. This can be obtained directly via integration:

$$h_P^{-1}(y) = -\frac{2}{\varepsilon}[(a-1)\ln(-a+\sqrt{y+1}+1)+\sqrt{y+1}] + C_P \qquad b=0$$

$$h_P^{-1}(y) = \frac{1}{\varepsilon b}\left[\frac{2\tan^{-1}\left(\frac{2b\sqrt{y+1}+1}{\sqrt{-4(a-1)b-4b^2-1}}\right)}{\sqrt{-4(a-1)b-4b^2-1}} - \ln(-a+by+\sqrt{y+1}+1)\right] + C_P \qquad b>0.$$

Using (2.14), (2.15) it is straightforward to compute the time (T_S) it takes for $h_S(t)$ to reach y_J, and then derive values for C_P such that $h_P^{-1}(y_J) = T_S$ as required by our definition of h_p.

To compute the jump up point y_J, we derive an expression for $\tilde{y}_j(y_i)$ which is also needed in the definition of our kick map. In order to use the integral condition (2.8), we must first write expressions for the y dynamics in the form of Eqn. (2.7). Here we substitute y_{SN} by y_i in the expression of C_S for (2.12) and (2.13) to allow for arbitrary initial conditions and get

$$y(t) = y_i + a\varepsilon t \qquad b=0$$

$$y(t) = y_i + (1-e^{-b\varepsilon t})(\frac{a}{b}-y_i) \qquad b>0$$

which yields

$$g(\varepsilon t) = a\varepsilon t \qquad b=0 \tag{2.16}$$

$$g(\varepsilon t) = (1-e^{-b\varepsilon t})(\frac{a}{b}-y_i) \qquad b>0 \tag{2.17}$$

which in turn give

$$g^{-1}(y) = \frac{y}{a} \qquad b=0 \tag{2.18}$$

$$g^{-1}(y) = -\frac{\ln(1+\frac{y}{y_i-a/b})}{b} \qquad b>0. \tag{2.19}$$

It is easy to compute the extremal eigenvalue for the linearization about $z = 0$ of the fast subsystem in Eqn. (2.2) : $\lambda = y \pm iw$ and therefore $Re(\lambda(y)) = y$. Turning now to the integral condition (2.8), when $b = 0$ we use (2.18) and write

$$0 = \int_{y_i}^{y_j} \frac{y}{a} dy$$

by which we can deduce that

$$y_j = \tilde{y}_j(y_i) = -y_i \qquad b = 0. \tag{2.20}$$

In other words, when the slow variable follows a linear ramp along the silent branch S (see (2.16)), the jump up point y_j is symmetric to the initial point y_i about $y_H = 0$. This can be seen from Fig. 2.2 where $y_{SN} = -1$ and $y_J = 1$.

In the case where $b > 0$, y follows a saturating exponential ramp along S (see (2.17)) which implies that y decelerates as it moves rightwards and thus shortens the slow passage. Using (2.19) in the integral condition (2.8), we get

$$0 = \int_{y_i}^{y_j} \frac{y}{b(1 + \frac{y - y_i}{y_i - a/b})(a/b - y_i)} dy$$

which gives

$$0 = \left[-\frac{1}{b} \frac{a \ln(by - a)}{b} + y \right]_{y = y_i}^{y_j}$$

thus implying the relation

$$y_i - y_j = \frac{a}{b} \ln(\frac{by_j - a}{by_i - a}).$$

We then isolate y_j to get

$$y_j = \tilde{y}_j(y_i) = \frac{a}{b}[W(-\frac{1}{a} e^{\frac{b}{a} y_i - 1}(a - by_i)) + 1] \qquad b > 0 \tag{2.21}$$

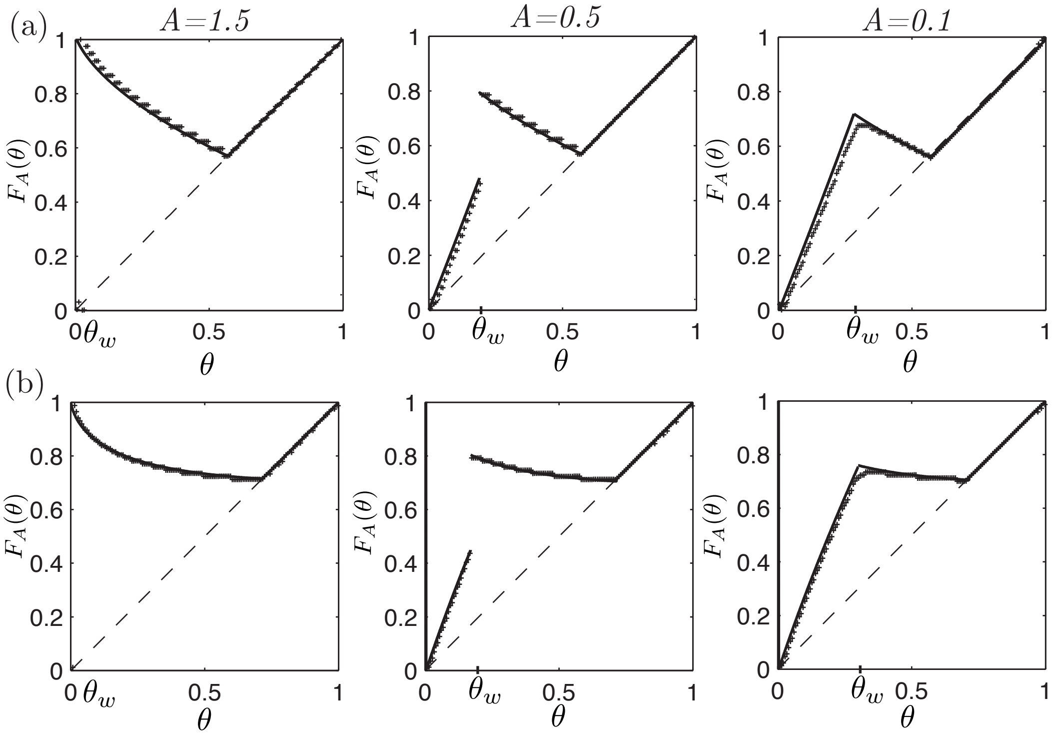

Figure 2.6: Analytically (solid lines) and numerically computed (markers) kick maps $F_A(\theta)$ for three values of kick amplitude A. (a) Model parameters: $\{\varepsilon = 0.01, w = 1, a = 0.8, b = 0\}$. (b) Model parameters: $\{\varepsilon = 0.01, w = 1, a = 0.4, b = 0.5\}$.

where W is the Lambert W function (product logarithm function).

The last ingredient we need is an expression for the cutoff value $y_w(A)$; recall that this marks the y boundary below which a given kick will not clear the separatrix U with radius $r_U(y) = \sqrt{1 - \sqrt{y+1}}$. This quantity does not depend on the slow dynamics and is therefore the same for both our cases. For a kick amplitude A, $y_w(A) = (1 - A^2)^2 - 1$ if $A \in [0, 1]$ (a weak kick). When $A > 1$, the kick is strong and we set $y_w = y_{SN} = -1$.

Using the expressions above we can build our kick map by using (2.9) and rescaling time by the period of a full cycle. To find the period for a given set of parameters, we use h_S^{-1} and h_P^{-1} to derive the silent and active passage times T_S and T_P. We reiterate that the only dependence on a kick's amplitude A is implicitly contained in the expression for $\theta_w = h_S^{-1}(y_w(A))$. As mentioned above, whenever $A > 1$, the kicks are strong ($\theta_w = 0$) and the resulting maps have a fixed shape. On the other hand, as A decreases below 1, the weak kick effect progressively uncovers the left branch of the map ($\theta_w \neq 0$).

To verify our derivation of the kick map, we choose 3 prototypical kick amplitudes: one strong ($A = 1.5$) and two weak ($A = 0.5$ and $A = 0.1$). We then plot the associated maps for two distinct set of model parameters: $\{\varepsilon = 0.01$, $w = 1$, $a = 0.8$, $b = 0\}$ and $\{\varepsilon = 0.01$, $w = 1$, $a = 0.4$, $b = 0.5\}$ in order to better visualize the effects of linear ($b = 0$) and saturating exponential ($b > 0$) ramps for the y dynamics.

In Fig. 2.6, we plot numerically and analytically computed maps, rescaled to the unit circle. Observe that we get very good agreement between the two and that the main features of weak kicks are captured by our phase reduction model. However, numerically computed maps have fine, plateau-like segments. As argued in [11], there are as many of these plateaus as there are spikes in a burst. They appear since a kick can induce bursts with spike counts ranging from one to the number seen in an unperturbed cycle. Since these numbers are integers and we numerically identify phase zero with the last spike of a burst, these plateaus are formed by phases that induce the same number of spikes following a kick. This is not captured by our analytical derivation of the kick map, which is computed from averaged conditions on the fast variable. However, we will see in Sect. 2.5 that the presence of noise in the system tends to diminish these plateaus, and in Sect. 5 that key aspects of synchrony and desynchrony for the original ODEs are predicted by our derived kick map.

We close this section with some remarks concerning the generality of features found in the kick map. We use the normal form model (2.2) for its analytical tractability but the general mechanism responsible for bursting, and hence the associated kick map, have characteristics that span across models. For example, for both linear ($b = 0$) and saturating exponential ($b > 0$) slow dynamics – which imply distinct interactions between the slow and fast subsystems – the maps are qualitatively identical. Specifically, at the end of Sect. 2.3.4, we noted that region of expansion in the left part of the weak kick map is a general feature of elliptic bursters with slow passage effects. The fact that the right branch follows the identity is another general attribute.

The shape of the middle branch (read left branch for strong kick map) is, however, more model dependent. Notice that both of our strong kick maps (for $A = 1.5$) have a left branch that steepens as we move leftwards. This is due to the dependence of h_P^{-1} on $r_P^2(y)$, which grows as $\sqrt{y}$. As a result, for A sufficiently large, $\frac{dF_A(\theta)}{d\theta} < -1$ for $\theta \in (0, \theta_c)$ where θ_c is the root of

$$\frac{d}{d\theta} h_P^{-1} \circ h_S(\theta_c) + 1 = 0. \tag{2.22}$$

For our parameter set with $b = 0$, $\theta_c \simeq 0.0968$ while for the second set with $b > 0$, $\theta_c \simeq 0.0619$. This curvature shrinks as we decrease the parameter a in (2.2) and the silent phase lengthens.

In general, this branch depends on the slow dynamics and the ratio of silent to spiking times T_S/T_P, which impose the following constraint: by construction, a strong kick implies $F_A(0) = 1$ and $F_A(T_S) = T_S$. If we were to approximate the y dynamics by constant velocities (as done in [11]), this map branch would be linear and hence contractive, whenever $T_S > T_P$. In general, as long as the latter is true and the functions h_S, h_P (desribing y dynamics) have small total variation, we can expect this branch to be mostly contractive, as for both cases explored above. We note that we obtain such contraction for the biophysical systems we study in Sect. 2.6.2, meant to model GPe neurons in the Parkinsonian state; [11] draws an interesting contrast with cases having $T_S < T_P$. The generality of these features motivate the analysis of dynamics induced by the kick map as we show in the next section.

In light of these remarks and in the interest of clarity, we use the maps computed above for the parameter set with $b = 0$ to carry out our analysis for the rest of the chapter. We stress that the arguments that will follow hold true for other parameter sets of system (2.2) and any elliptical bursting system having the features described above.

2.4 Dynamics of the kick map

Now that we have an understanding of an elliptic burster's response to input kicks of various strengths A, we turn to the other input parameter of relevance – the period between these kicks τ – and study the iterated dynamics of the map for various combinations of A and τ.

2.4.1 Iterative framework

We now use the kick map to build an iterative dynamical system capturing the evolution of cells subject to periodic stimulation. Let

$$F_{A,\tau}(\theta) \equiv F_A(\theta) + \tau \pmod 1 \tag{2.23}$$

which returns the phase of a kicked cell right before the next kick, τ time units later. The parameter τ translates the map vertically as illustrated in Fig. 2.7. For a chosen pair (A, τ) and some initial phase θ_0, an orbit is defined by $\theta_{n+1} = F_{A,\tau}(\theta_{n-1}) = F^n_{A,\tau}(\theta_0)$.

We note that, in contrast with the map of [11], our kick map does not become rescaled as τ is varied, but is rather translated around the circle (as in related studies [9, 42]). Another difference is the presence of sustained expansion even though $T_S > T_P$ (see above), due to accelerated slow passage effects induced by weak kicks; we will show that this expansion leads to positive Lyapunov exponents for certain values of τ. This phenomenon has been exploited in simpler dynamical systems with slow passage through a supercritical Hopf bifurcation in the context of chaos control [95].

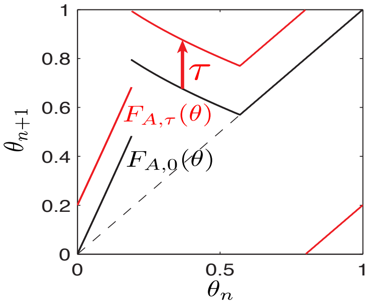

Figure 2.7: Effect of kick period $\tau(\mod 1)$ on the kick map. Original kick map $F_A(\theta)$ in black and τ induced kick map $F_{A,\tau}(\theta)$ in red. τ simply translates the map vertically.

Equation (2.23) assumes that a kick acts on cells located on unperturbed trajectories. As also noted above, the separation of timescales for elliptic bursters implies very fast attraction back to steady state trajectories following a kick, so that this assumption is generally valid. Moreover, the iterated dynamics for small values of τ are relevant in any case, as they can be accessed by longer, equivalent kick periods modulo one.

We next use Eqn. (2.23) to study the response of a population of identical elliptic bursters with different initial conditions to a common, pulsatile signal. For example, globally stable fixed points or periodic orbits represent phase locking regimes towards which the long term behavior of any cell will converge. On the other hand, maps that yield sensitivity to initial conditions and complex orbits are representative of desynchronizing inputs, when delivered to a population. To further explore population behavior, we need to define a metric by which we quantify synchrony of phase points on S^1. We call this our “synchrony measure” and describe it next.

2.4.2 Assessing synchrony

There are many ways one can quantify how closely N points are distributed on S^1. Two natural choices are the binned entropy H and order parameter R (also known as vector strength) :

$$H(\theta_1, ..., \theta_N) = \frac{1}{\log(1/N)} \sum_{j=1}^{N} p_j \log(p_j)$$

$$R(\theta_1, ..., \theta_N) = |\frac{1}{N} \sum_{j=1}^{N} e^{i2\pi\theta_j}|.$$

For H, we divide S^1 into N equal length subintervals, or bins, and take p_j to be the number of phases in bin j over N (using the convention $0 \log 0 = 0$). H takes its maximal value one when there is a phase spread into each bin and its minimum value zero when all are concentrated into a single bin. On the other hand, R takes its minimum value zero when phases are evenly distributed, and one when they are all equal.

Each measure has strengths and weaknesses as a metric of synchrony. For example, R can be zero if the phases are split into two equal, antipodal groups on S^1 – this is hardly an asynchronous state. For a large N, H can take relatively large values even if cells are distributed in close by bins. By taking

$$W(\theta_1, ..., \theta_N) = \frac{1}{2}[R(\theta_1, ..., \theta_N) + (1 - H(\theta_1, ..., \theta_N))].$$

to be the average of R and $1-H$, we can be assured that low measures of W correspond to cases where cells are well distributed across bins and that these bins are broadly spread around S^1. Specifically, we assess synchronization properties of a given map by taking N cells $\{\theta_n\}_{1 \leq n \leq N}$ with some initial distribution on S^1, pushing these states forward through m iterates, and computing $\bar{W}$ as the average over the last k out of these m iterates:

$$\bar{W} = \frac{1}{k} \sum_{i=m-k}^{m} W(F^i(\theta_1), ..., F^i(\theta_N)). \tag{2.24}$$

Throughout the chapter, we take $m \geq 100$ and $k = 20$, having found empirically that values change little with larger values of either.

2.4.3 High period orbits and positive Lyapunov exponents

We next investigate how iterations of our kick maps act on a population of cells for the three prototypical cases of strong ($A = 1.5$) and weak kick maps ($A =$0.5, 0.1), plotted in panel (a) of Fig. 2.6. We note that, while smooth maps on the circle are well characterized [117, 64], the discontinuities in our map introduce a number of distinct phenomena – such as border collision bifurcations with period adding at all orders, and "sharp" transitions to chaos. There is an ongoing effort to build a theory to better understand such systems [10, 13, 53, 60].

We first plot orbit diagrams with respect to the parameter τ for each of the three maps at hand (Fig. 2.8). Specifically, we select 100 cells uniformly distributed on S^1; for various $\tau \in [0, 1]$, we compute the positions of these cells after 150 iterates of $F_{A,\tau}(\theta)$ and "vertically" plot the result. Directly below these orbit diagrams, we plot the synchrony measure $\bar{W}$ of these end states, together with numerically computed Lyapunov exponents λ for each τ, averaged over all trajectories. Finally we compute approximations of invariant measures for each τ, using a variation of Ulam's method developed in [29] (this produces a discretized approximation of fixed densities for a map's Perron-Frobenius operator). The results are plotted in the bottom panels of Fig. 2.8.

We begin by describing results for the strong kick map ($A = 1.5$). Recall that the leftmost part of the strong kick map ,when $\theta \in (0, \theta_c)$ ($\theta_c \simeq$0.0968, derived in Eq. (2.22)) has a derivative greater than one in absolute value. The derivative is less then or equal to one in absolute value everywhere else. It is easy to see that the map

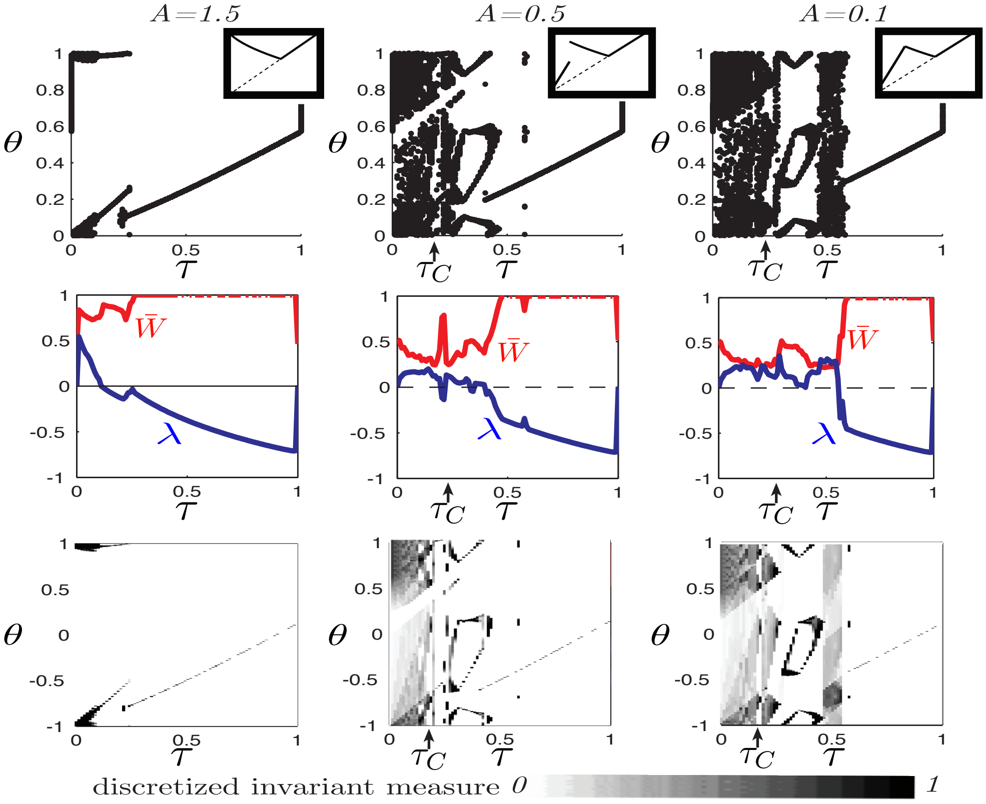

Figure 2.8: Orbit diagrams and related measures for kick maps (Eqn. (2.9)). Top to bottom: orbit diagrams of 100 cells after 150 iterations; synchrony measure $\bar{W}$ (red) and averaged Lyapunov exponent λ (blue); invariant measure approximates. Left to right: strong kick with $A = 1.5$; weak kick with $A = 0.5$; weak kick with $A = 0.1$. Marked values for τ_C below which Lemma 1 applies.

has a fixed point for any τ. If the map intersects the identity at $\theta \in (0, \theta_c)$, the fixed point is unstable and we find that complex dynamics emerge. We can witness this by looking at the orbit diagram of this map for small τ. Nevertheless, we see that cells tend to cluster in small regions and hence are relatively synchronized. For any other $\tau \neq 0$, we have stable fixed points, implying phase locking of cells to the input kicks. Note that for all maps, $\tau = 0$ implies a continuum of neutrally stable fixed points, as the right branches of the maps align perfectly with the identity.

For the weak kick maps ($A = 0.5,\ 0.1$), some values of τ yield stable, discrete attractors as well: fixed points and periodic orbits. More interesting are values of τ which produce thick, chaotic attractor-like objects. These are associated with what appear to be locally absolutely continuous invariant measures and positive Lyapunov exponents. It is in these regimes that our synchrony measures show a greater spread of cells. This is indicative of chaos, the presence of which is consistent with expansive regions of weak kick maps. Interestingly, these regions appear whether or not a map has a gap or not, as we show below.

Rigorously assessing the presence of chaos is, however, not a simple task. This was accomplished for related piecewise smooth maps [14, 20, 65, 17] where various definitions of chaos were used, depending on context. For example, Keener [65] showed that piecewise, surjective and non-decreasing maps with overlap have rotation numbers spanning a non-empty interval, an indication of chaos for circle maps. Unfortunately, our weak kick maps sometimes fail to have surjectivity (e.g. A=0.5) and always fail to be non-decreasing. One can also try to define trapping regions and a family of intervals for which interval images cover at least one other interval and the image of at least one interval covers at least two others. This constructs an shift on a space of sequences, which can characterize a chaotic system. However, building such an interval family for the weak kick map proves to be quite complex as intervals get flipped by decreasing parts of the map and severed by discontinuities. Thus, we do not aim at a complete characterization of the complex dynamics produced by our weak kick maps. However, we next show that, for some τ values, there is a positive lower bound on (sustained) Lyapunov exponents of any trajectory.

In Fig. 2.8, we see that some values of τ ($0 < \tau \lesssim 0.2$) induce dynamics that appear chaotic for both of our weak kick maps. Thus motivated, we state the following lemma:

Lemma 1 *Consider a piecewise defined map $F(\theta)$ on the circle which is smooth on* *three non-intersecting intervals* I_1*,* I_2 *and* I_3 *with* $\bar{I}_1 \bigcup \bar{I}_2 \bigcup \bar{I}_3 = S^1$*. Suppose* $|\frac{dF}{d\theta}|_{I_1}| \geq a > 1$*,* $|\frac{dF}{d\theta}|_{I_2}| \geq b > 0$ *– such that* $\ln(a) > |\ln(b)|$ *– and additionally that* $\frac{dF}{d\theta}|_{I_3} = 1$*. Then if* $F(I_2) \subset I_3$*,* $F(I_3) \bigcap I_2 = \emptyset$ *and* $F(I_3) \neq I_3$*, the Lyapunov exponent associated with the orbit of almost any initial condition* $\theta_0 \in S^1$*, if well defined, will be strictly greater than zero (*$\lambda(\theta_0) > 0$*).*

Proof: Given θ_0 and its forward orbit $\{\theta_n\}_{n=0,1\ldots}$, the local Lyapunov exponent can be written as $\lambda(\theta_0) = \lim_{N\to\infty} \frac{1}{N} \sum_{n=0}^{N} \ln |\frac{d}{d\theta} F(\theta_n)|$. The derivative is defined everywhere in S^1 except the 4 border points of the intervals I_1, I_2, I_3, which is obviously a measure zero set. The condition $F(I_2) \subset I_3$ imply that any point in I_2 is sent to I_3. Since F is smooth on I_3 and $\frac{dF}{d\theta}|_{I_3} = 1$, the condition $F(I_3) \neq I_3$ implies that any point in I_3 must eventually exit it. Let $C = \max_\theta\{n = \min_m\{m \,|\, F^m(\theta) \notin I_3\} \,|\, \theta \in I_3\}$. Then any element of I_3 stays in I_3 at most C iterates. Furthermore, $F(I_3) \bigcap I_2 = \emptyset$ implies that elements of I_3 are eventually sent to I_1. When an orbit point visits I_1, it contributes at least $\ln(a) > 0$ to the sum in $\lambda(\theta_0)$, at least $\ln(b)$ (possibly< 0) if it visits I_2 and 0 when it passes by I_3. By tracking which intervals an orbit visits, any admissible subsequence featuring I_2 must contain $I_2 \to I_3$. The sequence that contributes the least to $\lambda(\theta_0)$ is therefore $I_2 \to I_3 \to \ldots \to I_3 \to I_1$ where I_3 is repeated C times. It follows that for almost every θ_0, $\lambda(\theta_0) \geq \frac{1}{2+C}(\ln(a) + \ln(b) + 0 + \ldots + 0) > 0$. $\square$

We note that weaker conditions could be stated under which a positive Lyapunov exponent results, but the above are sufficient for the map at hand, as we now show. In particular, we show that Lemma 1 can be applied to the weak kick maps for certain values of τ. Clearly, the intervals $(0, \theta_w)$, (θ_w, T_S) and $(T_S, 1)$ will play the roles of I_1,I_2 and I_3. For our prototypical weak kick maps, we have $|\frac{dF_{A,\tau}}{d\theta}|_{(0,\theta_w)}| \geq 2.7$, $|\frac{dF_{A,\tau}}{d\theta}|_{(\theta_w,T_S)}| \geq 0.65$ and $\frac{dF_{A,\tau}}{d\theta}|_{(T_S,1)} = 1$ which fulfills the derivative criteria. It remains to show that the intersection requirements for interval images are met; we take a graphical approach which leads to conditions on τ. In Fig. 2.9, panels (b) and (c) show the map for $A = 0.5$ along with the marked intervals for two distinct values of τ and cobweb diagrams of sample trajectories. One can verify that the Lemma's assumptions are respected as long as the leftmost tip of the middle branch stays smaller than one and the rightmost tip is greater than the identity (panel (c)). This happens when $0 < \tau < \tau_C$ where

$$\tau_C = 1 - \lim_{\theta \to \theta_w^+} F_{A,0}(\theta). \tag{2.25}$$

Although we do not explicitly graph it, the same argument holds for $A \in (\delta, 1)$ for some $\delta > 0$. We must impose a positive lower bound for A in order for this argument to be valid since in the limit where $A \to 0$, the kick map is not well defined (very weak impulses may interact with slow passage effects via mechanisms not explored here). We will study such interactions in a stochastic setting in Sect. 2.5. Typically, A should be taken to be $> O(\varepsilon)$.

For valid weak kicks, we use Eq. 2.25 compute the upper bounds τ_C. Specifically, we get $\tau_C \simeq 0.205$ for $A = .05$ and $\tau_C \simeq 0.26$ for $A = 0.1$. As expected, these are close to 0.2, the rough higher bound we predicted earlier from Fig. 2.8. In addition to positive Lyapunov exponents, $\tau < \tau_C$ imposes a cyclic structure where trajectories visit a large portion of all three intervals in finite time, which is necessary for the population to become widely distributed around S^1.

For $\tau > \tau_C$, various dynamics can be observed. Figure 2.8 shows that positive Lyapunov exponents can still be found sporadically but the regions on which the trajectories accumulate can be considerably smaller. Periodic orbits of various periods are also present; in particular, high τ values seem to be associated with stable fixed points. This motivates a separation of the (A, τ)–space into three regions: I, where Lemma 1 applies; II, where dynamics are complex and transitions between what appears to be periodic orbits and smaller chaotic regions can be seen; III, stable fixed points (1:1 phase locking). Panel (a) in Fig. 2.9 shows these regions. We reiterate that these regions are not well defined when $A \to 0$. Furthermore, we stress that further analysis of region II might yield additional structure but the complexity of our map (circular domain, increasing and decreasing parts, transitions from gaps to discontinuity points, etc.) renders a complete analysis outside of this chapter's scope.

From what was described above, we see that region I is given by

$$\mathrm{I}: \{(A,\tau)|0<\tau<\tau_C(A)=1-\lim_{\theta\to\theta_w(A)^+}F_{A,0}(\theta)\}$$

where we have written the expression for τ_C to highlight its dependence on the kick amplitude A. As A increases, θ_w decreases and consequently, τ_C as well. Region I vanishes altogether when the kick transitions from weak to strong – at $A = 1$, where $\tau_C = 0$.

To define the boundary between regions II and III, we need to derive a condition under which our maps have a stable fixed point. We begin by inquiring about when the middle branch of the map intersects the identity. This happens when $\tau_C + \theta_w < \tau < 1$. The stability of the resulting fixed point depends on the derivative of the branch at the intersection point.

Again, as A increases and both θ_w and τ_C decrease, more of the middle branch of the map is exposed. When $\tau = \tau_C + \theta_w$, the leftmost tip of this branch intersects the identity. If A is sufficiently large, the resulting fixed point will be unstable; recall that for the strong kick map ($A > 1$), $|\frac{dF}{d\theta}| > 1$ when $\theta \in (0, \theta_c)$. It follows that if $\theta_w < \theta_c$, the first fixed points to appear as τ increases are unstable. We include unstable fixed points in region II and get the following definitions

$$\begin{aligned}\mathrm{II}:&\{(A,\tau)|\tau_C(A)<\tau<\tau_C(A)+\max\{\theta_w(A),\theta_c\}\}\\ \mathrm{III}:&\{(A,\tau)|\tau_C(A)+\max\{\theta_w(A),\theta_c\}<\tau<1\}.\end{aligned}$$

What can be taken from our analysis thus far is that to desynchronize cells with a τ-periodic input, the best strategy appears to be weak kicks with $0 < \tau < \tau_C$ (region I). To illustrate this, panels (b) and (c) of Fig. 2.9 show sample trajectories

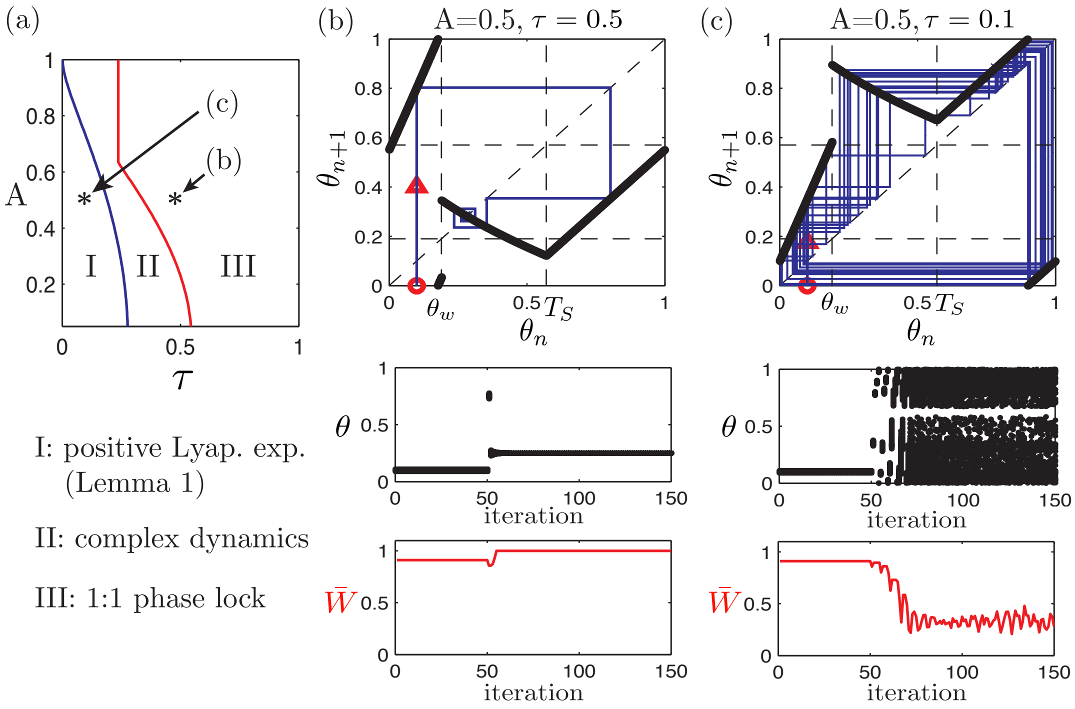

Figure 2.9: (a) Three regions of map dynamics in (A, τ)-space (see text for details). (b) & (c): two sample evolution trajectories for the kick map with $A = 0.5$. Top to bottom: cobweb diagrams and marked intervals $(0, \theta_w)$, (θ_w, T_S) and $(T_S, 1)$ for which Lemma 1 applies; sample trajectories with 50 initial condition randomly chosen close to $\theta = 0.1$ (iterations 50 and above are from kick map); synchrony measure $\bar{W}$. (b) $\tau = 0.5$, cells synchronize; (c) $\tau = 0.1$, cells desynchronize.

for 50 cells under the action of the weak kick map with $A = 0.5$ in both synchronizing (region III) and desynchronizing (region I) regimes. To mimic a synchronous state, our initial phases are drawn from a uniform distribution on an interval of width .01, around $\theta = 1/10$. The first 50 iterates are taken with respect to the identity map, reflecting a preliminary period with no pulsatile inputs. The next iterates are taken with respect to the weak kick map with $\tau = 0.5$ (region III, panel (b)) or $\tau = 0.1$ (region I, panel (c)).

As expected, for $\tau = 0.5$, every cell attracts to a single fixed point and the synchrony measure is maximized. However, for $\tau = 0.1$, the cells quickly become widely distributed. This was foreseeable from the shape of the computed invariant measures at this value of τ. Importantly, the synchrony measure drops substantially.

We close this section with an important remark concerning circle maps and phase locking. Here, our kick map can be seen as a A-perturbation of a τ-rotation. Typically, smooth perturbations of rotations admit Arnold Tongues: well separated wedge like regions where phase locking with rational rotation number occurs (see e.g. [131], Sect. 21.6). In our case, the loss of smoothness introduces sustained region where chaotic dynamics prevail, hereby showing surprising effects of discontinuous circle maps.

2.5 Effects of noise on kick map and synchrony

Up to this point, we developed a phase reduction framework to analyze the dynamics of periodically forced bursters. We now ask: does the phase reduction remain valid in the presence of noise? If so, what qualitative changes in the map occur, and what are the consequences for entrainment of bursters? In this section, we develop answers through a blend of numerical results and analytical approximations.

The effects of stochastic perturbation on elliptic bursters have been previously studied in various contexts [3, 120, 69]. The unifying theme is the effect of noise on slow passage through a Hopf bifurcation.

Here, we build on these results to better understand the role of noise on burst responses to periodic pulsatile inputs. We will comment further on prior results as we progress.

To this end, we introduce a stochastic perturbation in the fast variables of the normal form model, so that Eqn. (2.2) becomes

$$\begin{aligned} \dot{z} &= (y + iw)z + 2z|z|^2 - z|z|^4 + I(t) + \eta\xi(t) \\ \dot{y} &= \varepsilon(a - |z|^2 - by). \end{aligned} \tag{2.26}$$

where $\eta \geq 0$ is a small, real, noise strength parameter and $\xi(t)$ is a time-periodic train of discrete small kicks with normally distributed amplitudes. That is, $\xi(t) = \sum_i \xi_i \delta(t - i\Delta t)$, where the ξ_i are i.i.d. as $N(0, \sqrt{\Delta t})$ and the timestep Δt controls the temporal resolution of the noisy perturbation. We take $\Delta t = 0.05$, the numerical solver's maximal timestep, so that $\xi(t)$ approximates white noise (see Sect. 2.6 for more on numerical methods). Notice that the noise term only acts on the real part of the fast variable z, which mimics a cell's voltage variable.

In [3], the authors show that such noise terms diminish slow passage effects through supercritical Hopf points (i.e., causing cells to jump to the spiking state closer to y_H); in [120], a similar effects was found for elliptic bursters [120, 69]. As we discuss below, there are cases where a phase reduction can still be defined in the presence of such noise, with an interesting and tractable impact on the kick map's shape.

2.5.1 Effects of noise on the phase reduction of elliptic bursters

Our previously derived phase reduction relied on an important assumption: periodicity of the burst cycle. As discussed in Sect. 2.3, elliptic bursters do not necessarily have periodic solutions, but rather a metastability property which guarantees the constancy of cycle's duration T, up to $O(\varepsilon)$. This regularity is what enables our phase reduction.

When noise is added to the fast subsystem, either regular or highly variable burst durations can result, depending on noise strength and type [3, 120, 69]. Below, we will show that there is a wide range of noise strengths that significantly impact the underlying dynamics, but maintain regular burst durations. Specifically, for system

(2.26) ($\varepsilon = 0.01$, $w = 1$, $a = 0.8$, $b = 0$) we compute the coefficient of variation (CV) of these durations as described in Sect. 2.3.3, for noise strengths η ranging from 10^{-17} to 10^{-1}.

Panel (c) of Fig. 2.10 shows our findings. Although the mean period $\langle T \rangle$ decreases with increasing noise strength, the CV remains low – below 10^{-2} – for the range of noise strengths $\eta \leq 10^{-3}$ (recall that $CV \approx 10^{-3}$ for the noiseless case). In other words, for a wide range of noise strengths, random forcing does not introduce substantial variability to the burst period. This is consistent with results from [120] where the authors show in a closely related setting that the silent and spiking times T_S and T_P are related to the log of the noise amplitude.

Despite the fact that they preserve regular burst periods, noise strengths $\eta \leq 10^{-3}$ have a strong impact on the slow passage effect. The integral condition (2.8) reflects cancellation of attraction to S by and repulsion away from it; noise limits the extent of attraction and therefore the duration required for repulsion. This is illustrated in panel (a) of Fig. 2.10, which shows that the jump up point from silent to spiking regimes decreases as η increases within $[0, 10^{-3}]$. In this regime, the averaged y dynamics are relatively unaffected by this stochastic forcing, so that CV remains low. Once $\eta = 10^{-2}$, there is no slow passage and the solutions jump up to spiking as soon as y crosses y_H. For $\eta > 10^{-2}$, the stochastic kicks have accumulated effects comparable to our forcing kicks and we see solutions randomly jumping into spiking before y reaches y_H, which explains the increasing CV for this range of noise strengths [120].

We next pursue phase reduction to an approximate, deterministic circle map for the low CV cases ($\eta \in [0, 10^{-3}]$).

2.5.2 Effect of noise on the kick map

For strong kicks – where responses are not determined by slow passage effects – adding noise does not considerably change the shape of the kick map; the chief effect is that the region where $|\frac{dF_A}{d\theta}| > 1$ shrinks (not shown). This similarity was expected since a strong kick instantaneously translates a bursting solution to the active phase, where noise has little effect since fast dynamics follow large amplitude trajectories.

For the remainder of this section, we concentrate on the considerable changes noise induces for weak kick maps. In panel (b) of Fig. 2.10 we plot numerically computed maps for $A = 0.5$ and $\eta = 10^{-15}$, 10^{-9}, 10^{-3}. Each marker represents the average response of a given initial phase to 10 distinct realizations of stochastic forcing. In what follows, we derive approximations for these maps, plotted in solid lines on the same figure. In order to proceed, we discuss key differences among numerical maps of stochastic bursters with varying noise strength.

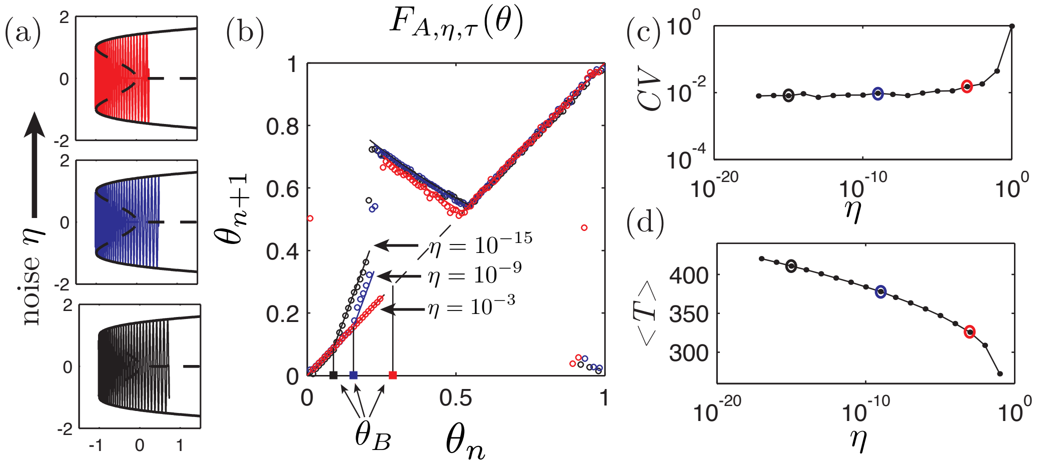

Figure 2.10: (a) Slow passage effect shortens with increasing noise. (b) Numerically and analytically computed kick maps (from Eqn. (2.36)) for noise strengths $\eta = 10^{-15}$, $\eta = 10^{-9}$ and $\eta = 10^{-3}$ (all with kick amplitude $A = 0.5$). (c) CV of burst cycle period (computed using 150 cycles) against η using a log-log scale. (d) Average burst cycle period $\langle T \rangle$ (same sample as in (c)) against η using a log-linear scale.

We can see that the maps are qualitatively similar in almost all aspects except the left branch, which collapses on the identity as noise increases. Recall that the expansion in this branch is due to altered slow passages due to weak perturbations on the stable part of the silent branch S. As discussed above, noise shortens slow passages and one might expect the steepness of the expansive part to decrease as noise increases. Surprisingly, it is not this steepness that changes but rather the onset of the expansive ramp (θ_B defined below) which varies. To explain this phenomenon, we must turn to the concept of buffer points for delayed bifurcations.

When deriving the analytical kick map (2.9), we relied on the integral condition (2.8) which dictates that the further a solution starts (at y_i) from the Hopf point y_H, the longer the slow passage will be. This is true for y_i in a range before y_H, up to a point beyond which this relation fails. In fact, given some y dynamics, one observes that the length of the slow passage ($y_j - y_H$) saturates to a constant value for any initial y_i far enough from y_H. This is called the *maximal delay*. The closest point to the "static" bifurcation point (y_H) to generate a maximal delay is called the *buffer point* of a delayed bifurcation [28]. The techniques used in [3, 120, 69, 4] to analyze deterministic and stochastic slow passages assume that a solution always remains closer to the bifurcation than the associated buffer point. This is also the case for the bursters we study in the absence of noise, where the buffer point is to the left of y_{SN}. Thus, it does not affect the dynamics, enabling us to use condition (2.8).

For noisy bursters, the numerically derived weak kick maps in Fig. 2.10 show that the buffer point can lie to the *right* of y_{SN}, therefore exerting an important effect. If a weak kick is delivered when y_i is to the left of the buffer point, the trajectory retains no memory of the kick and the phase of the cell is left unchanged by the kick. If it is delivered when y_i is to the right of the buffer point, the kick will shorten the slow passage, as for the noiseless case.

To our knowledge, there are no general results in the literature deriving buffer points for noisy delay bifurcations. In what follows, we derive an approximation for them, in the context of weakly kicked trajectories, that holds for Eqn. (2.26). We work in the small Δt limit, so that the stochastic forcing is white noise.

Buffer points and stochastic slow passage through the Hopf point

For a given noise strength η, define y_B to be the buffer point for the delayed Hopf bifurcation in Eqn. (2.26). That is, y_B is the smallest initial value y_i such that a weak kick delivered at y_i will induce a change in the jump up point y_j. Naturally, $y_B < y_H$ and judging by the shape of our weak kick maps in Fig. 2.10, we can expect $y_{SN} < y_B$. We now derive a probabilistic criterion that gives an accurate approximation for y_B.

We begin by assuming that Δt is sufficiently small in Eqn. (2.26) so that the noise term $\eta\xi(t)$ can be approximated by the white noise term $\eta dW(t)/dt$,

where $W(t)$ is a real valued Wiener process. We are interested in solutions following the silent branch S when $y \in (y_{SN}, y_H)$. As done in Sect. 2.3.5, we make the singular limit assumption that z travels on S and therefore that $|z| = 0$. This enables us to decouple the y dynamics and get an expression for $y(t) = y_i + g(\varepsilon t)$, precisely as in the deterministic case (see Eqns. (2.16),(2.17)). These assumptions hold in the limit that ε and $\eta \to 0$, and we will show that they give good approximations for the parameters used here ($\epsilon = 0.01$, $\eta \leq 10^{-3}$).

Since we are interested in solutions near S, which is composed of fixed points of the fast subsystem, we linearize the fast dynamics about $z = 0$. We write the resulting equation in real coordinates $x = (x_1, x_2)^T$ where $z = x_1 + ix_2$:

$$dx = J(t)xdt + BdW(t) \tag{2.27}$$

where

$$J(t) = \begin{pmatrix} y(t) & -w \\ w & y(t) \end{pmatrix}, \quad B = \begin{pmatrix} \eta & 0 \\ 0 & 0 \end{pmatrix}$$

and $W(t)$ is now a two dimensional real valued Wiener process. Notice that $J(t)$ commutes with itself ($J(t)J(s) = J(s)J(t)\ \forall\ t, s$) which enables us to write the noise-free ($\eta = 0$) solution of (2.27) as

$$x(t) = e^{\int_0^t J(s)ds} x_i$$

where $x(0) = x_i$. Using this property, Ito's formula yields explicit expressions for the mean $\mu(t)$ and covariance matrix $\Sigma(t)$ of the time dependent probability distribution for x governed by Eqn. (2.27):

$$\mu(t) = e^{\int_0^t J(s)ds} \mu_i \tag{2.28}$$

$$\Sigma(t) = e^{\int_0^t J(s)ds} \Sigma_i e^{\int_0^t J(s)^T ds} + \int_0^t dt' e^{\int_{t'}^t J(s)ds} BB^T e^{\int_{t'}^t J(s)^T ds} \tag{2.29}$$

where $\mu(0) = \mu_i$ and $\Sigma(0) = \Sigma_i$. See [39], Chap. 4 for details of this derivation. In particular, we will suppose that we have an initial distribution for x that is Gaussian; then, the distribution of x at any time t is fully determined by Eqns. (2.28) and (2.29), as a Gaussian distribution with mean $\mu(t)$ and $\Sigma(t)$. We introduce the following notation $\tilde{p}(\cdot)$ for this distribution, which makes clear the dependence on the initial condition for $y(0) = y_i$ as well as the initial distribution of x and the elapsed time t:

$$x \sim \tilde{p}(x(t)|y_i, \mu_i, \Sigma_i) \ . \tag{2.30}$$

We next study the distribution of our (linearized) fast variable x at the Hopf point y_H when no kick is delivered. This will give us a reference unkicked, or "natural" distribution $p_n(x)$ important in computing the buffer point below. The trajectories of interest jump down from spiking when $y = y_i = y_{SN}$ and take $g^{-1}(y_H - y_{SN})/\varepsilon$ time units to reach y_H. We use Eqn. (2.30) to write the resulting distribution as

$$p_n(x) = \tilde{p}(x(g^{-1}(y_H - y_{SN})/\varepsilon)|y_{SN}, (0,0)^T, \Sigma_{SN}) \tag{2.31}$$

where

$$\Sigma_{SN} = \begin{pmatrix} r_P(y_{SN})^2 & 0 \\ 0 & r_P(y_{SN})^2 \end{pmatrix}$$

and we have used Eqn. (2.7) to substitute in for time in Eqn. (2.31). The natural distribution is therefore defined to have an initial variance equal to the squared radius of the periodic orbits on P when they vanish at y_{SN}, marking the end of the spiking phase. Due to the long timescale of the slow dynamics, however, we find that the choice of initial variance has little effect on p_n. We note that $p_n(x)$ is centered at $x = (0, 0)^T$ with covariance depending on η.

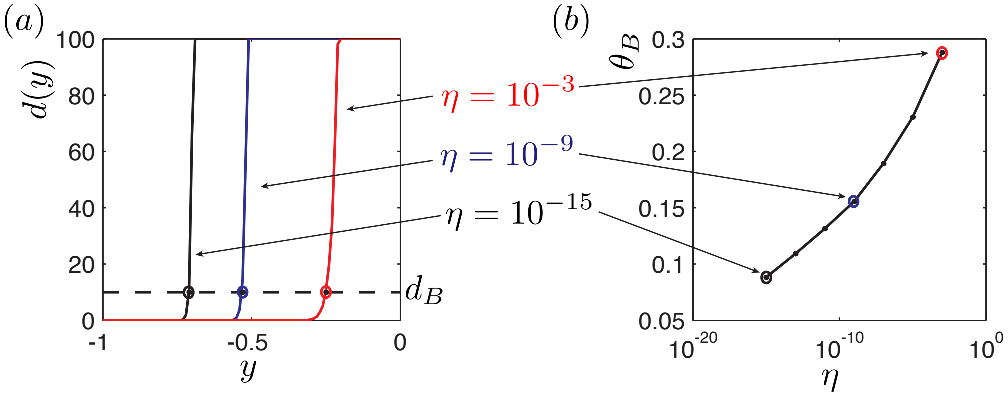

Figure 2.11: (a) Plot of $d(y)$ with respect to y for $\eta = 10^{-15}, 10^{-9}, 10^{-3}$. Dashed black line marks the threshold d_B determining the points y_B at the intersections with the $d(y)$ curve. (b) Plot of buffer phase point θ_B with respect to noise strength η, marking the onset of expansion in the weak kick map. Kick strength is $A = 0.5$, as in Fig. 2.10.

Next, we ask whether a trajectory that has received a weak kick can be expected to undergo comparable slow passage through the Hopf point as for the unkicked trajectories described by $p_n(x)$. Note here that an unkicked trajectory admits a maximal delay going through the Hopf bifurcation, and that some kicked trajectories will also have the same slow passage, as we expect $y_{SN} < y_B$.

If kicked trajectories typically pass through y_H at locations x with high probability density according to $p_n(x)$, we expect that they will have a comparable slow passage times as unkicked trajectories. On the other hand, if these trajectories are typically found where $p_n(x)$ is low, this indicates that they are further away from the branch of equilibria S. Thus, they will tend to escape S (i.e., jump up) sooner than the unkicked solutions. We obtain an approximation for the buffer point y_B by asking when this distinction between kicked and unkicked trajectories at y_H occurs.

To this end, we compute the "kicked" distributions of trajectories $p_{k,y}(x)$ for which a weak kick of amplitude A is applied when $y(t) = y$. Upon their arrival at y_H, we approximate these distributions as

$$p_{k,y}(x) = \tilde{p}(x(g^{-1}(y_H - y)/\varepsilon)|y, (A, 0)^T, \Sigma_n) \tag{2.32}$$

where the mean trajectory is at $(A, 0)^T$ following the kick and Σ_n is the covariance matrix from $p_n(x)$, under the assumption that the trajectory followed the natural burst cycle before the translation induced by the kick. We now assess to what extent $p_{k,y}$ and the natural distribution p_n overlap. We use the symmetrized Kullback-Leibler Divergence between the two distributions

$$d(y) = \frac{1}{2}\left(D_{KL}[p_n(x)\|p_{k,y}(x)] + D_{KL}[p_{k,y}(x)\|p_n(x)]\right) \tag{2.33}$$

where

$$D_{KL}[p\|q] = \int_{\mathbb{R}^2} p(x)\ln\frac{p(x)}{q(x)}dx\ . \tag{2.34}$$

For y sufficiently far from y_H, the distribution $p_{k,y}$ has enough time to converge close to $p_n(x)$ before $y(t)$ reaches y_H. As a consequence, $d(y)$ will be close to zero. We define the A-dependent buffer point y_B to be the first value of y for which $d(y)$ grows beyond a threshold d_B. Since the distributions $p_{k,y}$ and p_n are sharply peaked Gaussians (with variance of order η^2), $d(y)$ quickly explodes – to several orders of magnitude above one – when the two distributions fail to overlap. Therefore, we choose $d_B = 10^1$ as a good indication of separation among kicked vs. unkicked trajectories, as illustrated in Fig. 2.11 (a).

Finally, we determine the phase point θ_B corresponding to y_B, via (2.4):

$$\theta_B = \frac{h_S^{-1}(y_B)}{T} \tag{2.35}$$

where T is the mean period of the unperturbed trajectory. This point marks the onset of expansion for the associated kick map. We find excellent agreement of this prediction with numerically computed kick maps, as seen from Figs. 2.11 (b) and 2.10 (b).

Deriving the kick map for noisy bursters

We next derive an approximate expression for the complete kick map in the presence of weak noise. Our first step is to decouple the y dynamics from the (noisy) fast variables. This is guided by the assumption that, due to weak noise, most trajectories closely follow S and P. We then proceed to derive h_S, h_S^{-1} and h_P^{-1} as done in Sect. 2.3.4, with a single modified value: y_J. Indeed, as described above, the jump up point y_J is closer to y_H for noisy bursters and we numerically compute its value for each noise strength η.

In the presence of a buffer point, a weak kick can now have two outcomes: either it has no effect if it is received when $0 < y < y_B$ as it does not alter slow passage, or it shortens slow passage as in the deterministic case, when $y_B < y < y_w$. To capture the slow passage effects of weak kicks (responsible for the expansion in our map) in the presence of noise, we still use integral condition (2.8). Although this formula was derived for deterministic bursters, it relies in the linearization of the fast dynamics about S, which we assume remains valid even in the noisy case. As a result, numerical simulations show that $\tilde{y}_j(y)$ holds true for $y \in (y_B, y_H)$ except in a short interval to the right of y_B where small errors are observed. Note that these errors diminish with smaller noise for which $\tilde{y}_j(y_B)$ is quite close to the numerically computed y_J. We proceed to write an expression for our new kick map, which now contains an addition piecewise-defined section arising from the presence of θ_B:

$$F_A(\theta) = \begin{cases} \theta & \text{if } \theta \in [0, \theta_B] \\ \theta + h_P^{-1}(\tilde{y}_j(h_S(\theta))) - h_S^{-1}(\tilde{y}_j(h_S(\theta))) & \text{if } \theta \in [\theta_B, \theta_w) \\ h_P^{-1} \circ h_S(\theta) & \text{if } \theta \in [\theta_w, T_S] \\ \theta & \text{if } \theta \in [T_S, 1]. \end{cases} \tag{2.36}$$

We obtain excellent fits as shown in Fig. 2.10 (b). We end by noting that we get similar fits for various kick strengths A as well as distinct parameters sets (i.e. $b > 0$) for the normal form model (not shown).

2.5.3 Effect of noise on iterated dynamics

We now explore the dynamical properties of the kick maps computed in the presence of noise. Figure 2.12 shows orbit diagrams, synchrony measures and averaged Lyapunov exponents three maps (computed as for Fig. 2.8). For $\eta = 10^{-5}, 10^{-9}$, the maps retain some expansion and we see behavior that appears chaotic for small positive values of τ. This range of τ values shrinks as the as the expansive region of the map gives way to neutrality with increasing noise; at the same time, the “support” of the orbit diagrams appears to decrease. Arguments similar Lemma 1 can be formulated for these cases to show the existence of positive Lyapunov exponents (see also bottom panels of Fig. 2.8).

For the map with $\eta = 10^{-3}$, there is no expansive region: although there is still a slow passage effect the kick's amplitude $A = 0.5$ induces a cutoff θ_w small enough such that the system does not retain memory of any kick ($\theta_w < \theta_B$). Thus, we cannot expect positive Lyapunov exponents (see bottom panel in Fig. 2.12). However, the orbit diagram shows a broad spread of points for small positive τ. These are stable, high period orbits, originating from border crossing bifurcations as τ increases. This has been established by Bélair in the context of periodically forced integrate and fire oscillators [9], where a very similar map is studied: he shows that as the map is shifted vertically, stable periodic orbits of a wide range of periods can be found, following a Farey tree sequence.

In sum, small positive values of τ result in either positive Lyapunov exponents or high period orbits for the weak kick maps, depending on the noise level η assumed in deriving the (deterministic) map. In the first case, expansion directly desynchronizes cells; in the second, we will see that the high period of orbits, coupled with additional variability due to the underlying noise, can have a similar effect.

We now introduce stochastic terms into our discrete kick map dynamics to account for the variability in burst periods discussed above (i.e., $CV \neq 0$). If, for a given cycle, a cell has a shorter/longer period than the one used to compute it's kick map, its phase following a kick will be slightly shifted from the phase given by the iteration of the map. To capture this, we introduce *jitters*: additive stochastic terms acting on τ, independent for every cell. The goal is not to capture the exact phase response of cells, but rather to give a qualitative account for the impact of period variability on statistical metrics such as our synchrony measure. We proceed as follows:

Since the construction of our kick maps rescales the period of any burster to be 1, the CV can be interpreted as the standard deviation of a burst cycle's period. We define a *jitter* ζ to be random variable drawn from a normal distribution with zero mean and standard deviation equal to the CV of the case we are considering. Suppose we want to model the phase evolution of M cells subject to a common, periodic kick train of period $\tau(\text{mod } 1)$, of amplitude A, subject to stochastic forcing of strength η. The phase of the m^{th} cell right before the $n+1^{st}$ kick can be written as follows

$$\theta^m_{n+1} = F_{A,\eta,(\tau+\zeta^m_n)}(\theta^m_n) \tag{2.37}$$

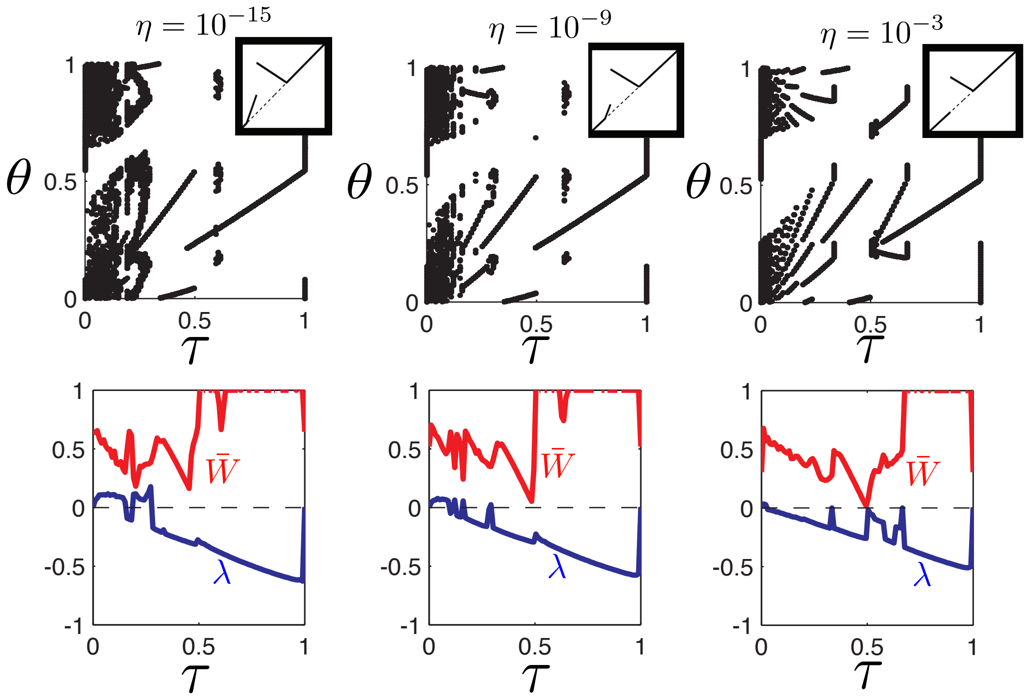

Figure 2.12: Orbit diagrams and related measures for weak kick maps with $A = 0.5$, for various noise strengths η (see Fig. 2.10). Top to bottom: orbit diagrams of 100 cells after 150 iterations; synchrony measure $\bar{W}$ (red) and averaged Lyapunov exponent λ (blue). Left to right: low noise strength $\eta = 10^{-15}$; medium noise strength $\eta = 10^{-9}$; high noise strength $\eta = 10^{-3}$.

where $\zeta_n^m \sim^{iid} N(0, CV_\eta)$. In other words, at every iteration, we draw a different jitter ζ for every cell. Note that we modified our notation to emphasize the map's dependence on noise strength η (Fig. 2.10).

Using (2.37), we again iterate 100 cells 150 times with added jitters and plot the orbit diagrams and synchrony measures in Fig. 2.13, for the same three levels of η as in the preceding figures. Jitters, as expected, "smear" orbit diagrams, with a greater effect for larger η. In particular, note the smoothing of periodic points for small positive τ in the high noise case ($\eta = 10^{-3}$). Interestingly, the twin effects of noise in reducing expansion but increasing cell-to-cell jitter result in comparable levels of the

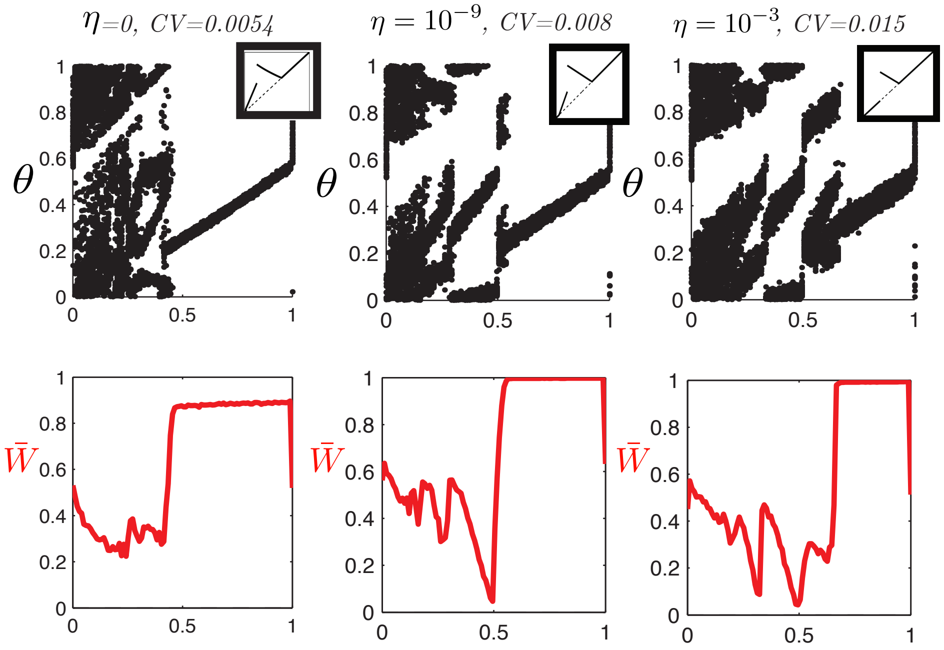

Figure 2.13: Orbit diagrams and synchrony measure for weak kick maps with $A = 0.5$, for various noise strengths η and added jitters $\zeta(CV)$. Top to bottom: orbit diagrams of 100 cells after 150 iterations; synchrony measure $\bar{W}$. Left to right: low noise strength $\eta = 10^{-15}$; medium noise strength $\eta = 10^{-9}$; high noise strength $\eta = 10^{-3}$.

synchrony measure $\bar{W}$ across the three cases.

We reiterate our main conclusion: although the underlying mechanisms differ across a wide range of noise strengths η, pulsatile inputs in the "weak" kick regime – with an input frequency slightly slower than (a multiple of) cells' intrinsic frequencies – will result in desynchrony among a population of recipient cells.

2.6 Validity of phase reduction, O.D.E. simulations, and a neurobiological model

In this section, we explore the validity of our phase reductions in both deterministic and noisy cases – and our analysis of the discrete kick map that follows – by numerically integrating the O.D.E.s themselves. Rather than demonstrating a complete correspondence between the kick map and solutions of the differential equations, we seek to verify that an informed choice of kick amplitude and period, based on the kick maps, does indeed yield the predicted (de)synchrony behavior among solutions to the O.D.E.s. Specifically, we show that small, positive values of τ (i.e., $\tau \in (0, \tau_C)$ in the deterministic case) with amplitudes in the "weak" regime lead to the greatest desynchrony; conversely, large values of τ synchronize cells.

We first consider the normal form system (2.2), and then turn to a biologically detailed neuronal model for which our main findings persist. All numerical computations were carried out in MATLAB. We use the stiff solver `ode15s` with both absolute and relative tolerances set to 10^{-6} to integrate all differential equations; input kicks and additive noise are treated as non-autonomous terms by the solver.

2.6.1 Normal form model

Here, we numerically integrate a population of $N = 30$ uncoupled cells governed by system (2.2) or its stochastic counterpart Eqn. (2.26), taking the "large" noise value $\eta = 10^{-3}$ studied above (with $\{\varepsilon = 0.01,\, w = 1,\, a = 0.8,\, b = 0\}$). We concentrate on one weak kick amplitude, $A = 0.5$. In each case, we implement periodic kicks that correspond to $\tau = 0.1$ and $\tau = 0.8$ for the kick map, to illustrate desynchronizing and synchronizing behavior respectively. More precisely, we use a kick period equal to $(1 + \tau) \times T$ where T is the natural period of the O.D.E.'s burst cycle. This allows trajectories at least one natural period to relax toward the unperturbed cycle in between kicks (similar dynamics occur for periods $T \times (n + \tau)$, $n \in \mathbb{N}$). For $\eta = 0$, $T \simeq 465$ while for $\eta = 10^{-3}$, $T \simeq 337$ (Fig. 2.10(d)).

Figure 2.14 displays the results via *raster plots*: for each cell, a dot is placed at the moment that spiking terminates (corresponding to phase $\theta = 0$). We also plot a synchrony measure for the simulated population. This is done by assigning phases to each cell relative to their most recent spike termination event, as a fraction of elapsed time partitioned in bins of length T. To better illustrate the desynchronizing effect of weak kicks with $\tau = 0.1$, initial conditions are chosen at random with phases at most 2% apart (i.e., an initially synchronized population); to illustrate the synchronizing effect of kicks with $\tau = 0.8$, initial phases are allowed to be more sparse. In all cases, we let the cells evolve without inputs for a few burst cycles, and then begin to apply the pulsatile inputs.

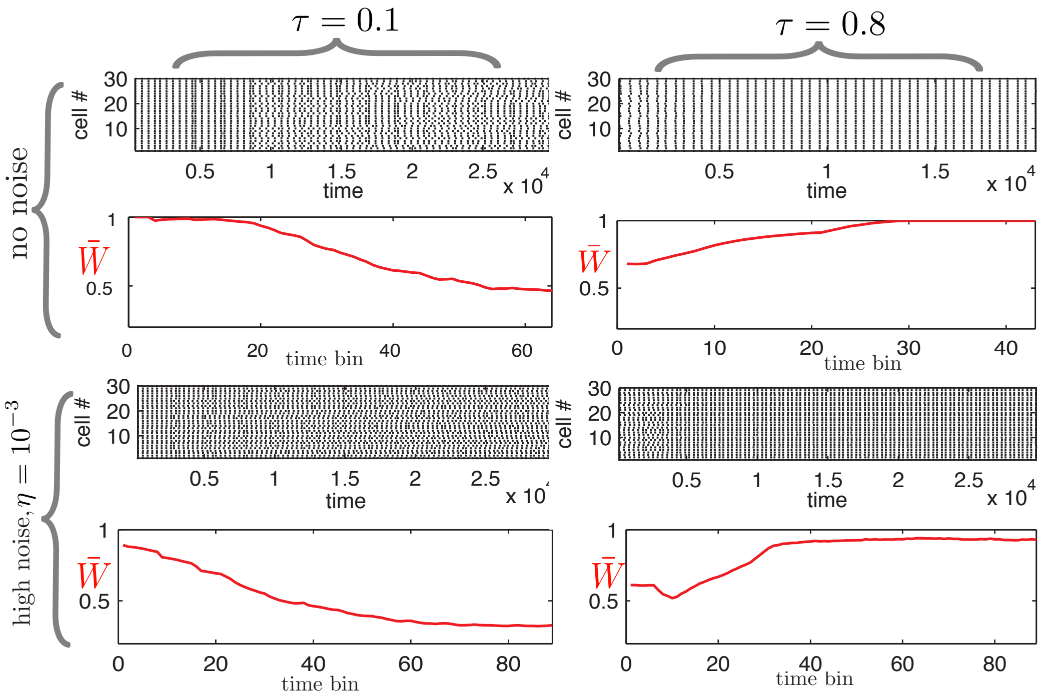

Figure 2.14: A population of 30 numerically integrated solutions of Eqn. (2.2) or (2.26), all receiving a common, periodic weak kick input ($A = 0.5$). Left column: kick period $T \times 1.1$ (equivalent to $\tau = 0.1$) results in population desynchrony. Right column: kick period $T \times 1.8$ (equivalent to $\tau = 0.8$) synchronizes the population. Top row: no noise ($\eta = 0$). Bottom row: high noise ($\eta = 10^{-3}$). Black dots give the raster plot (see text); red curves plot the synchrony measure $\bar{W}$ vs. time (see text).

The results agree well with predictions from the kick map: a weak kick of $A = 0.5$ administered at $T \times 1.1$ successfully spreads cells apart while the same kick with period $T \times 1.8$ synchronizes the population. Note that we chose these values of τ only as informed guesses; other nearby values can achieve similar results in both synchronizing and desynchronizing the population. Moreover, results for various other kick amplitudes also agree well with the behavior predicted from the associated kick maps (not shown).

2.6.2 GPe bursting neuron

We now investigate whether the mechanisms described above will persist for a more biologically detailed model. Specifically, we study a 5-dimensional, Hodgkin-Huxley-type model of a neuron from the GPe basal ganglia nucleus [124, 11]. This model produces elliptic bursting where the onset of spiking is due to a subcritical Hopf bifurcation and a burst termination is due to a saddle node on an invariant circle, in agreement with the normal form system (2.2). In detail, the fast variables are the voltage V, potassium current gating variable n, sodium current gating variable h, and calcium T-current gating variable r. The slow variable is calcium concentration Ca. The equations are as follows:

$$\begin{aligned}
C_m \frac{dV}{dt} &= -I_{Ca} - I_{Na} - I_K - I_L - I_{AHP} - I_T - I_{app} + I(t) + \eta\xi(t) \\
\frac{dn}{dt} &= -\frac{\phi_n(n - n_\infty)}{\tau_n} \\
\frac{dh}{dt} &= -\frac{\phi_h(h - h_\infty)}{\tau_h} \\
\frac{dr}{dt} &= -\frac{\phi_r(r - r_\infty)}{\tau_r} \\
\frac{dCa}{dt} &= -\varepsilon(I_{Ca} + I_T + k_{Ca}Ca)
\end{aligned} \tag{2.38}$$

where the I terms represent membrane currents and are functions of the gating variables and the voltage; all definitions and parameter values are as in [124]. Additionally, the terms $I(t)$ and $\eta\xi(t)$ represent the pulsatile inputs and the noise term, entering as currents.

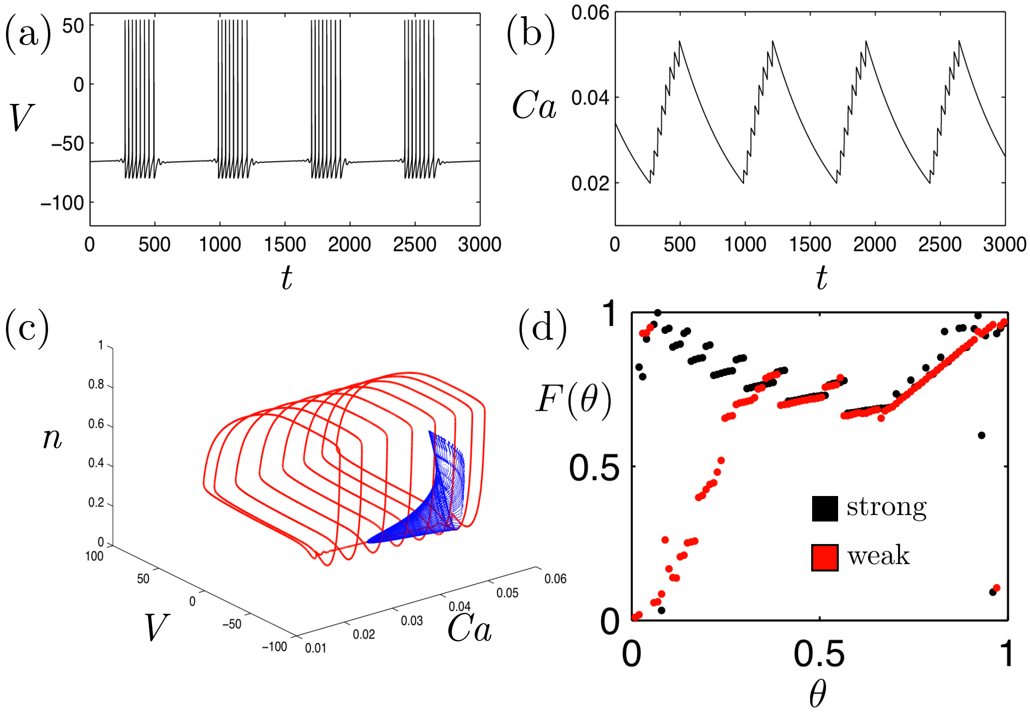

Figure 2.15: Plots from model (2.38). (a) Voltage trace. (b) Calcium trace. (c) Bursting solution in n, V, Ca plane in red and separatrix U in blue. (d) Two numerically computed kick maps for model (2.38) with high noise strength $\eta = 10^{-3}$; strong kick ($A = 30$) in black and weak kick ($A = 3$) in red.

Figure 2.15(a) shows that the shape of action potentials and the timescales differ from those of the normal form model (2.2); nevertheless, the dynamics have a very similar structure. In particular, panel (c) shows a (projected) 3-dimensional plot of a bursting trajectory together with the skewed separatrix U, computed using the MATCONT package [27]. Figure 2.15(d) shows two numerically computed kick maps for both strong and weak kick amplitudes ($A = 30$ and $A = 3$, respectively). These maps were computed in the presence of noise with $\eta = 10^{-3}$, which is the largest noise strength that keeps CV at $O(10^{-2})$ for the simulations; maps represent the average phase response taken over ten runs with different noise realizations.

Overall, the structure of these maps is more complex than for the normal form model. In particular, “small” plateaus and associated discontinuities are promienent. As for the normal form model, there are as many plateaus as there are spikes in an unperturbed burst, and kicked solutions that elicit a certain number of spikes in the subsequent burst accumulate in each plateau. However, for this model, the slow variable (calcium concentration) varies more during a spike and creates bigger gaps between plateaus. As a result, even for a strong kick, certain values of τ yield localized stable periodic orbits, as opposed to only fixed points. These appear via border collision bifurcations due to discontinuities between plateaus (not shown). However, the small amplitude of these periodic orbits keeps the cells attracted to them quite synchronized.

Additionally, the shape of the left part of the weak kick map is also quite distorted compared with maps derived from the normal form model. In particular, notice that there are large discontinuities close to zero. This is due to the skewed cone shape of the separatrix U: since the neuron model does not have the same symmetry as our normal form system, when the solution drops down from spiking, it spirals towards the resting branch and some lobes of this spiral come very close to the separatrix. When the solution is kicked, even weakly, on the upper part of a lobe, it passes the separatrix and jumps to the spiking state; the same weak kick will not have this effect if it is delivered only moments later. The resulting large gaps in the weak kick map add to the complexity of the dynamics for low τ.

Apart from these differences, the prominent features observed in the kick map for the normal form model remain: the neutral/expanding left branch for the weak kick map, and the contracting middle branch and neutral right branch. We repeat the numerical experiment described in Sect. 2.6.1, this time only for the noisy case ($\eta = 10^{-3}$), and plot the results in Fig. 2.16. We see the expected synchronization and desynchronization from weak periodic kicks ($A = 3$) with periods equivalent to $\tau = 0.8$ and $\tau = 0.1$ respectively. While cells do not appear to become as desynchronized for the $\tau = 0.1$ case as in the normal form model, it is reasonable to believe that a

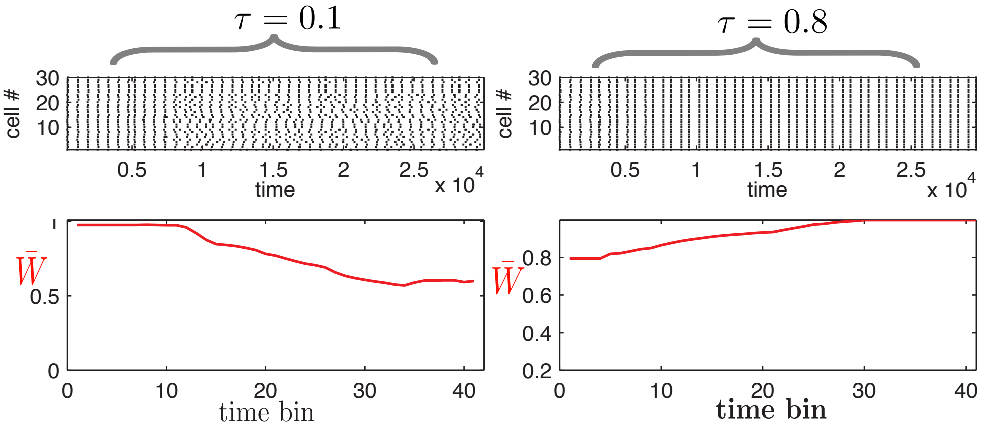

Figure 2.16: A population of 30 numerically integrated solutions of Eqn. (2.38) with noise strength $\eta = 10^{-3}$, receiving a common periodic weak kick input ($A = 3$). Left column: $T \times 1.1$ (equivalent to $\tau = 0.1$) results in population desynchrony. Right column: kick period $T \times 1.8$ (equivalent to $\tau = 0.8$) synchronizes the population. Other plotting details also as for Fig. 2.14.

more detailed analysis of the kick map for the neural model could identify (A, τ) combinations that would further desynchronize cells.

2.7 Composition of multiple periodic inputs, and an application to DBS

Above, we showed how weak, periodic inputs can lead to desynchronization for populations of uncoupled bursting cells. But how well can such inputs compete with other, synchronizing effects? The answer is important in varied applications. A prominent one is Deep Brain Stimulation (DBS) therapy for Parkinson's disease. Here, pathologically high levels of synchrony occur among bursting cells in the basal ganglia (BG). Synchrony in some basal ganglia areas is in large part driven by common, periodic inputs from other areas (see [108] and references therein). A surgically implanted DBS electrode delivers pulsatile electrical signals that are designed to mitigate the effects of this synchrony.

Using the normal form model (2.2), we undertake a brief demonstration of how our results could be applied to this setting, for the GPe basal ganglia nucleus that contains neurons believed to be elliptically bursting. We do not attempt detailed, biologically complete modeling or aim for direct clinical relevance, and as such note several limitations. Nevertheless, we now present some facts from the BG-DBS literature that motivate our simple setup.

Historically, the most widely used target for DBS has been the subthalamic nucleus (STN), where high intensity and high frequency pulsatile stimulation is applied. Such a stimulation strategy is believed to “mask” pathological synchrony by imposing higher frequency activity. However, emerging studies are investigating the use of stimulation signals of varied strength and frequency [50, 49, 25, 37], taking advantage of key physiological instabilities, to alleviate unwanted synchrony. Furthermore, recent results also explore the use of alternate DBS targets [61, 98] such as GPe. Inspired by this research, we explore the impact of stimulating GPe neurons with low intensity and frequency inputs that could harness the instabilities explored above.

Our model will only consider the GPe subpopulation. We motivate this and further modeling simplifications via features of GPe connectivity within the BG. First, while lateral connections between GPe cells have been reported, they are believed to be sparse overall and considerably weakened in Parkinsons (see [108, 98] and references therein). Thus, we will model cells within the GPe as uncoupled. Second, we note that GPe receives excitatory inputs from STN; in Parkinsons, the STN cells become more strongly synchronized and periodic. We will assume, as in many previous modeling studies [108, 98, 124, 11], that synaptic events from the STN are always sufficiently strong to elicit a spiking response in GPe cells (i.e., they are strong kicks). Finally, while GPe cells are coupled to the STN via inhibitory synapses, we do not consider such connections here: we restrict our investigation to the question of whether GPe cells receiving a periodic drive from STN can be desynchronized by DBS inputs. Other effects involving Gpe-STN recurrence remain for future studies.

In light of these remarks, we now study a population of uncoupled elliptic bursters that receives a strong periodic drive, mimicking STN input, entraining the cells into synchronous bursting. We then add a second periodic input, mimicking a DBS signal, designed to compete with the first drive and desynchronize the population. We suppose that a population of bursters receives a first sequence of synchronizing periodic impulses with period τ_1 and "strong" amplitude A_1. The action of these inputs on burst phases is given by the kick map $F_{A_1,\tau_1}(\theta)$. As throughout our chapter, this returns the phase of a cell following a kick, τ_1 time units later. Aiming to counteract the synchrony due to the first kick sequence, we introduce a second series of kicks of strength A_2. We assume that these have the same period, but are delayed by an amount τ_2. That is, the cell receives a A_2-kick τ_2 time units following each A_1-kick. We wish to write the kick map that captures the effect of such doublets of kicks.

In this context, the shift-time following a A_1-kick must be taken to represent the phase of cells right before the A_2-kick and the first application of the map must be $F_{A_1,\tau_2}(\theta)$. Similarly, we must shift the A_2 map by $\tau_1 - \tau_2$ to retrieve the phase of a cell before the next A_1-kick. Note that neither τ_2 nor $\tau_1 - \tau_2$ should be too small for this map to be valid, specifically in the presence of weak kicks when the cell must have time to enter its spiking phase before the following kick, for the map we derive to remain valid. When this restriction is satisfied, the doublet map is given by

$$F_{A_1 A_2,\tau_1 \tau_2} = F_{A_2,\tau_1-\tau_2} \circ F_{A_1,\tau_2} \ . \tag{2.39}$$

An example is shown in Fig. 2.17. Suppose we start with an entraining input of strong kicks with $A_1 = 1.5$ and $\tau_1 = 0.4$. We seek to oppose this synchronizing effect with weak kicks of amplitude $A_2 = 0.5$. We use the two first maps of panel (a) of Fig. 2.6 to build the resulting doublet map $F_{A_1 A_2,\tau_1 \tau_2}$. In panel (a) of Fig. 2.17, we compute the orbit diagram of this map (as done in Sect. 2.4) while treating τ_2 as our variable parameter. Using this diagram, we select $\tau_2 = .375$ (marked by a red arrow), associated with a low synchrony measure. We plot a cobweb diagram of a sample

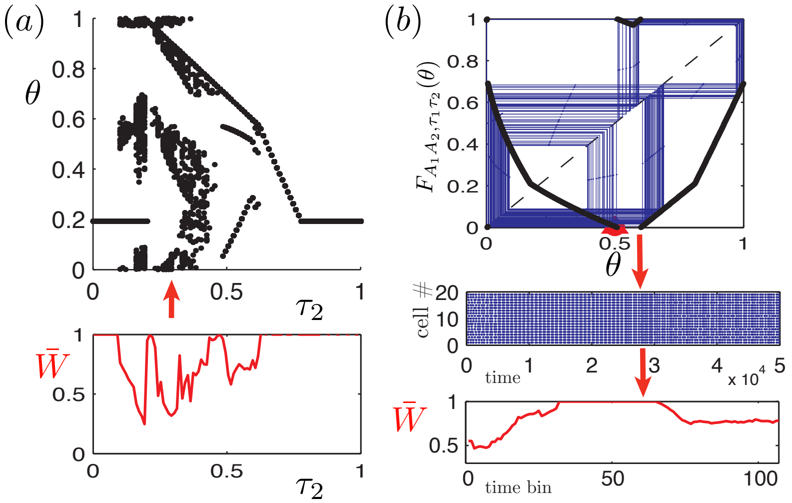

Figure 2.17: (a) Orbit diagram and synchrony measure for $F_{A_1A_2,\tau_1\tau_2}$ while varying τ_2. (b) Top : cobweb diagram of $F_{A_1A_2,\tau_1\tau_2}$ with τ_2 indicated by the red arrow in (a). (b) Bottom : O.D.E. simulation of 20 cells initially synchronized by a strong input and then desynchronized by competing weak kicks (starting at red arrows).

orbit in the top of panel (b) of Fig. 2.17, which clearly demonstrates the destabilizing effects of expansive regions in the doublet map.

We then verify the properties desynchronization predicted by the doublet map by numerically solving the underlying O.D.E.s (2.2), for twenty model cells. We begin with initial conditions such that the phases are desynchronized and apply strong kicks ($A_1 = 1.5$) at $1.4 \times T$, where T is the natural period of the bursters (i.e., corresponding to $\tau_1 = 0.4$). As predicted, the cells synchronize in response; see the binned synchrony measure rising up to one in the bottom of panel (b) of Fig. 2.17, or the raster plots above. After synchrony has developed (red arrows in panel (b)), we “switch on” the sequence of weak kicks, leaving in place the original strong kick sequence. Weak kicks are applied $0.375 \times T$ time units following each strong kick (i.e., $\tau_2 = 0.375$). The desynchronizing impact predicted by the doublet map is clear in both the scatter in raster plots and in the drop in the synchrony metric $\bar{W}$ that develops after the weak input begins to be applied.

2.8 Discussion

We study the behavior of a population of identical elliptic bursters receiving a periodic sequence of pulsatile inputs, or kicks. Our aim is to understand which input sequences will result in desynchronized vs synchronized bursts across the population. Following and extending the approach in [11], we first conduct a phase reduction of the burst dynamics to a circle map, using a slow/fast decomposition. This "kick map" depends on two parameters – the kicks' amplitude A and (relative) period τ – and maps phases from their states just before one input pulse to their states just before the next pulse arrives. We next study the effect of varying A and τ using a normal form model for elliptic bursting (Eqn. (2.2)).

We find that for strong kicks – i.e., with A sufficiently large so that the cell will always be spiking following an input – almost any choice of kick period τ resulted in $1:1$ phase locking, and hence synchrony across the population. For weaker kicks, we find a rich dynamical structure. In particular, the interaction of a weak perturbation with the slow passage effect through a subcritical Hopf point induces an expansive region in the kick map. By varying the kick period, we witness the appearance of stable fixed points, periodic orbits and regimes with positive Lyapunov exponent. As expected, this leads to desynchronization of the population. Overall, we divide the $(A,\ \tau)$ parameter space into the three regions shown in Fig. 2.9(a), corresponding to unstable, desynchronizing dynamics, 1:1 phase locking, and intermediate, complex behavior, The former, desynchronizing regime is associated with relatively weak kicks of periods slightly slower than the natural burst period ($0 < \tau < \tau_C$, see Eqn. (2.25)).

We also study the effect of stochastic perturbation via noise terms. We find that the phase reduction retains its validity but the kick map changes shape, presenting less expansion as the noise increased. Importantly, population desynchrony still results from weak kicks with comparable values of τ in this case, but through a different mechanism than the instabilities that occur for the noise free case. Here, desynchrony follows from a combination of high-period orbits and the noise itself. Overall, this phenomenon is related to the discontinuous nature of the circle map at hand; 1:1 phase locking rather than the complex dynamics observed would be expected for small τ for many smooth maps [42, 41].

We then test the predictions of the reduced circle maps via numerical simulation of the original O.D.E. system, finding qualitative agreement. Additionally, we simulate a more biologically realistic model of a GPe neuron, and continue to find agreement with the general predictions of our maps. Finally, we show that it is possible to use the kick map framework to study the effect of multiple sequences of inputs to a cell population. We build an example showing that carefully timed weak kicks can compete with an entraining strong input to successfully desynchronize a population of bursting cells.

As a closing remark, we note that the kick map studied here can also capture the effect of pulsatile input signals that are neither periodic, nor have a fixed kick amplitude. For any given sequence $\{A_n, \tau_m\}$, where A_n is the amplitude of the n^{th} kick and τ_n is the delay between kicks n and $n+1$, the relevant system is the composition of the maps $F_{A_n,\tau_n}(\theta)$. This gives rise to an iterated function system (IFS) acting on S^1. There is a growing body of literature dealing with these objects and their application to this problem could eventually help us to understand the behavior of bursting cells under arbitrary – and possibly stochastic – stimulation patterns.

Chapter 3

CHAOS AND RELIABILITY IN BALANCED SPIKING NETWORKS WITH TEMPORAL DRIVE

3.1 Overview

In the previous chapter, we addressed signal-induced variability at the level of single cells in the context of artificial stimulation of neurons. Here, we focus on driven dynamics at the population level in the context of networks that are driven by multi-dimensional signals.

Biological information processing is often carried out by complex networks of interconnected dynamical units. A basic question about such networks is that of *reliability:* if the same signal is presented many times with the network in different initial states, will the system entrain to the signal in a repeatable way? Reliability is of particular interest in neuroscience, where large, complex networks of excitatory and inhibitory cells are ubiquitous. These networks are known to autonomously produce strongly chaotic dynamics — an obvious threat to reliability. Here, we show that such chaos persists in the presence of weak and strong stimuli, but that even in the presence of chaos, intermittent periods of highly reliable spiking often coexist with unreliable activity. We elucidate the local dynamical mechanisms involved in this intermittent reliability, and investigate the relationship between this phenomenon and certain time-dependent attractors arising from the dynamics. A conclusion is that chaotic dynamics do not have to be an obstacle to precise spike responses, a fact with implications for signal coding in large networks.

The contents of this chapter are taken in part from a manuscript published in Physical

Review E entitled *Chaos and reliability in balanced spiking networks with temporal drive*, by Guillaume Lajoie, Kevin K. Lin and Eric Shea-Brown [71]. Special thanks go to Lai-Sang Young for helpful insights. This work was supported in part by an NSERC graduate scholarship, an NIH Training Grant, the Burroughs Wellcome Fund Scientific Interfaces, and the NSF under grant DMS-0907927. Numerical simulations were performed on NSF's XSEDE supercomputing platform.

3.2 Introduction

Information processing by complex networks of interconnected dynamical units occurs in biological systems on a range of scales, from intracellular genetic circuits to nervous systems [32, 12]. In any such system, a basic question is the *reliability* of the system i.e., the reproducibility of a system's output when presented with the same driving signal but with different initial system states. This is because the degree to which a network is reliable constrains how — and possibly how much — information can be encoded in the network's dynamics. This concept is of particular interest in computational neuroscience, where the degree of a network's reliability determines the precision (or lack thereof) with which it maps sensory and internal stimuli onto temporal spike patterns. Analogous phenomena arise in a variety of physical and engineered systems, including coupled lasers [128] (where it is known as "consistency") and "generalized synchronization" of coupled chaotic systems [110].

The phenomenon of reliability is closely related to questions of dynamical stability, and in general whether a network is reliable reflects a combination of factors, including the dynamics of its components, its overall architecture, and the type of stimulus it receives [75]. Understanding the conditions and dynamical mechanisms that govern reliability in different classes of biological network models thus stands as a challenge in the study of networks of dynamical systems. An ubiquitous and important class of neural networks are those with a balance of excitatory and inhibitory connections [116]. Such *balanced networks* produce dynamics that match the irregular firing observed experimentally on the "microscale" of single cells, and on the macroscale can exhibit a range of behaviors, including rapid and linear mean-field dynamics that could be beneficial for neural computation [127, 90, 130, 114, 87]. However, such balanced networks are known to produce strongly chaotic activity when they fire autonomously or with constant inputs [130, 79, 87]. On the surface, this may appear incompatible with reliable spiking, as small differences in initial conditions between trials may lead to very different responses. However, that the answer might be more subtle is suggested by a variety of results on the impact of temporally fluctuating inputs on chaotic dynamics [86, 5, 99, 75, 76, 78, 8].

At a more technical level, because of the link between reliability and dynamical stability, many previous theoretical studies of reliability of single neurons and neuronal networks have focused on the *maximum Lyapunov exponent* of the system as an indicator of reliability. This is convenient because (i) exponents are easy to estimate numerically and, for certain special types of models, can be estimated analytically [130, 107, 96, 79, 91, 96, 75]; and (ii) using a single summary statistic permits one to see, at a glance, the reliability properties of a system across different parameter values. However, being a single statistic, the maximum Lyapunov exponent cannot capture all relevant aspects of the dynamics. Indeed, the maximum exponent measures the rate of separation of trajectories in the most unstable phase space direction; other aspects of the dynamics are missed by this metric. Recently, attention has turned to the full Lyapunov spectrum. In particular, [87] compute this spectrum for balanced autonomously spiking neural networks, and suggest limitations on information transmission that result.

In this chapter, we present a detailed numerical study and steps toward a qualitative theory of reliability in fluctuation-driven networks with balanced excitation and inhibition. One of our main findings is that even in the presence of strongly chaotic activity – as characterized by positive Lyapunov exponents – single cell responses can exhibit intermittent periods of sharp temporal precision, punctuated by periods of more diffuse, unreliable spiking. We elucidate the local (meaning cell-to-cell) interactions involved in this intermittent reliability, and investigate the relationship between this phenomenon and certain time-dependent attractors arising from the dynamics (some geometric properties of which can be deduced from the Lyapunov spectrum).

3.3 Model description

We study a temporally driven network of $N = 1000$ spiking neurons. Each neuron is described by a phase variable $\theta_i \in S^1 = \mathbb{R}/\mathbb{Z}$ whose dynamics follow the "θ-*neuron*" model [33]. This models spike generation in so-called "Type I" neurons and are equivalent to the "quadratic integrate-and-fire" (QIF) model after a change of coordinates (see [33, 72] and Appendix A). These models can also be formally derived from biophysical neuron models near "saddle-node-on-invariant-circle" bifurcations; the underlying "normal form" dynamics [33, 34] are found in many brain areas. The θ-neuron model is known to produce reliable responses to stimuli in isolation [75, 107], cf. [81, 16]. Thus, any unreliability or chaos that we find is purely a consequence of network interactions.

Coupling from neuron j to neuron i is determined by the weight matrix $A = \{a_{ij}\}$. A is chosen randomly using an Erdös-Renyi scheme such that 20% of the cells j are inhibitory ($a_{ij} < 0 \ \forall i$) and 80% are excitatory ($a_{ij} > 0 \ \forall i$); we do not allow self-connections, setting $a_{ii} = 0$. Each neuron has *mean* in-degree $K = 20$ from each population (excitatory and inhibitory) and the synaptic weights are $\mathcal{O}(1/\sqrt{K})$ in accordance with the classical balanced-state network architecture [130]. We note that our results appear to be qualitatively robust to changes in N and K, but a detailed study of scaling limits is beyond the scope of this chapter.

A neuron j is said to fire a spike when $\theta_j(t)$ crosses $\theta_j = 1$; when this occurs, θ_i is impacted via the coupling term $a_{ij}g(\theta_j)$ where $g(\theta)$ is a smooth "bump" function with narrow support ($[-1/20, 1/20]$) around $\theta = 0$ satisfying $\int_0^1 g(\theta)d\theta = 1$, meant to model the rapid rise and fall of a pulsatile synaptic variable. In addition to coupling interactions, each cell receives a stimulus $I_i(t) = \eta + \varepsilon\zeta_i(t)$ where η represents a constant current and $\zeta_i(t)$ are aperiodic signals, modeled here (as in [16, 81, 75]) by "frozen" realizations of independent white noise processes, scaled by an amplitude parameter ε. Note that the white noise $\zeta_i(t)$ model external signals, not "noise" (i.e., driving terms that can vary between trials), though such terms can be easily added (as in [76]).

The i^{th} neuron in the network is therefore described by the following stochastic

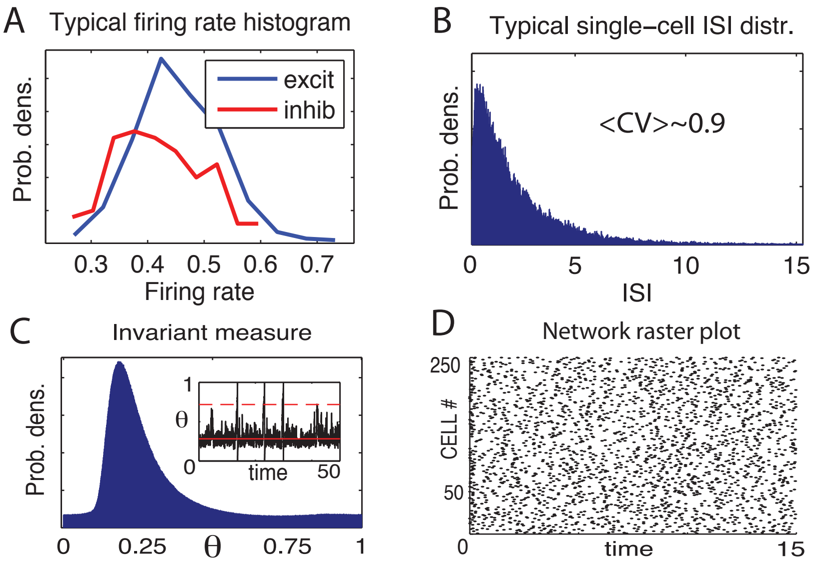

Figure 3.1: (A) Typical firing rate distributions for excitatory and inhibitory populations. (B) Typical inter-spike-interval (ISI) distribution of a single cell. The coefficient of variation (CV) is close to 1. (C) Invariant measure for an excitable cell ($\eta < 0$); inset: typical trajectory trace of an excitable cell where solid and dotted lines mark the stable and unstable fixed points. (D) Network raster plots for 250 randomly chosen cells. For all panels, $\eta = -.5$, $\varepsilon = 0.5$.

differential equation (SDE):

$$
\begin{aligned}
d\theta_i = [F(\theta_i) + Z(\theta_i) \left(\eta + \sum_j a_{ij} g(\theta_j) \right) + \\
\frac{\varepsilon^2}{2} Z(\theta_i) Z'(\theta_i)]dt + \varepsilon Z(\theta_i) \cdot dW_{i,t}
\end{aligned}
\tag{3.1}
$$

where the intrinsic dynamics $F(\theta_i) = 1 + \cos(2\pi\theta_i)$ and the stimulus response curve $Z(\theta_i) = 1 - \cos(2\pi\theta_i)$ come directly from coordinate changes based on the original QIF equations (see Appendix A and [33]). Here, $W_{i,t}$ is the independent Wiener process generating $\zeta_i(t)$; the ε^2 term is the Itô correction from the coordinate change [77]. Finally, η sets the intrinsic excitability of individual cells. For $\eta < 0$, there is a stable and an unstable fixed point, together representing resting and threshold potentials. Thus (contrasting [87] where cells are intrinsically oscillatory), neurons are in the "excitable regime," displaying *fluctuation-driven* firing, as for many cortical neurons [26].

In what follows, we focus on networks in this regime by fixing $\eta = -0.5$, where cells spike due to temporal fluctuations in their inputs (both from external drive and network interactions) rather than being perturbed and coupled oscillators. We study the effect of the amplitude ε of the external drive on the evoked dynamics. Note that in the absence of such inputs, these networks do not produce sustained activity.

Fig. 4.1 illustrates that the general properties of the network dynamics, including a wide distribution of firing rates from cell to cell and highly irregular firing in individual cells, are consistent with many models of balanced-state networks in the literature, as well as general empirical observations from cortex [90, 127]. An additional such property is that our network's mean firing rate scales monotonically with η and ε (data not shown), as in [130, 87].

3.4 Mathematical background

For reliability questions, we are interested in the response of a network to a fixed input signal, but starting from different initial states. Equivalently, we can imagine an *ensemble* of initial conditions all being driven simultaneously by the same signal $\zeta(t)$. If the system is reliable, then there should be a distinguished trajectory $\theta(t)$ to which the ensemble converges. In contrast, an unreliable network will lack such an attracting solution, as dynamical mechanisms conspire to keep trajectories separated. To put these ideas on a precise mathematical footing, it is useful to treat our SDE (3.1) as a *random dynamical system (RDS).* That is, we view the system as a nonautonomous ODE driven by a frozen realization of the Brownian process, and consider the action of the generated family of flow maps on phase space. In this section, we present a brief overview of RDS concepts and their meaning in the context of network reliability.

3.4.1 Random dynamical systems framework

The model network described by (3.1) is a SDE of the form

$$dx_t = a(x_t) + \sum_{i=1}^{N} b(x_t) \cdot dW_t^i \tag{3.2}$$

whose domain is the N-dimensional torus $\mathbb{T}^N$ and W_t^i are standard Brownian motions. We assume throughout that the Fokker-Planck equation associated with (3.2) has a unique, smooth steady state solution μ. Since we are interested in the time evolution of an ensemble of initial conditions driven by a *single, fixed realization* ζ generated by $\{W_t^i\}_i$, this can be done by considering the *stochastic flow maps* defined by the SDE, i.e., the solution maps of the SDE. More precisely, this is a family of maps $\Psi_{t_1,t_2;\zeta}$ such that $\Psi_{t_1,t_2;\zeta}(x_{t_1}) = x_{t_2}$ where x_t is the solution of (3.2) given ζ. If $a(x)$ and $b(x)$ from (3.2) are sufficiently smooth, it has been shown (see, e.g. [67]) that the maps $\Psi_{t_1,t_2;\zeta}$ are well defined, smooth with smooth inverse (i.e., are diffeomorphisms), and are independent over disjoint time intervals $[t_1, t_2]$.

RDS theory studies the action of these random maps on the state space. The object from RDS theory most relevant to questions of reliability is the *sample distribution* μ_ζ^t , defined here as

$$\mu_\zeta^t = \lim_{s \to -\infty} (\Psi_{s,t;\zeta})_* \rho_{init} \ , \tag{3.3}$$

where $(\Psi_{s,t;\zeta})_*$ denotes the propagator associated with the flow $\Psi_{s,t;\zeta}$, i.e., it is the linear operator transporting probability distributions from time s to time t by the flow $\Psi_{s,t;\zeta}$, and ρ_{init} is the initial probability distribution of the ensemble.

The definition above has the following interpretation: suppose the system was prepared in the distant past so that it has a random initial condition (where "random" means "having distribution ρ_{init}"). Then μ_ζ^t is precisely the distribution of all possible states at time t, after the ensemble has been subjected to a given stimulus $\zeta(t)$ for a sufficiently long time (how long is "sufficient" is system-dependent; the limit in the definition sidesteps that question). So if μ_ζ^t were very localized in space, then the system has "forgotten" its initial conditions, and is thus quite reliable, whereas is μ_ζ^t were very non-local then the system is unreliable. Note that μ_ζ^t depends on both ζ and the time t: as time goes by, the system receives more inputs, and μ_ζ^t continues to evolve; it is easy to see that $(\Psi_{t_1,t_2;\zeta})_* \mu_\zeta^{t_1} = \mu_\zeta^{t_2}$. In general, we expect μ_ζ^t to be independent of ρ_{init} so long as ρ_{init} is given by a sufficiently smooth probability density, e.g., the uniform distribution on $\mathbb{T}^N$.

Key quantities that determine the structure of μ_ζ^t are the *Lyapunov exponents* $\lambda_1 \geq \lambda_2 \geq ... \geq \lambda_N$ of the flow. These, as in the deterministic case, measure the rate of separation of nearby trajectories; for a "typical" trajectory, we expect a small perturbation δx_t to grow or contract like $|\delta x_t| \sim e^{\lambda_1 t}$. Note that under very general conditions, the exponents are deterministic, and thus are a function of system parameters but do not depend on the specific input ζ [66].

3.4.2 Linear stability implies reliability

The link between λ_1 and μ_ζ^t is furnished by a pair of theorems. The first is due to Le Jan, with extensions for SDEs by Baxendale:

Theorem 1 (Le Jan; Baxendale [74, 7]) *If $\lambda_1 < 0$ and a number of nondegeneracy conditions are satisfied [7], then μ_ζ^t is a random sink, i.e., $\mu_\zeta^t(x) = \delta(x - x_t)$ where x_t is a solution of the SDE.*

Given the interpretation of μ_ζ^t , this theorem suggests that $\lambda_1 < 0$ is associated with reliability.

A complementary theorem covers the case $\lambda_1 > 0$.

Theorem 2 (Ledrappier and Young [73]) *If $\lambda_1 > 0$, then μ_ζ^t is a random Sinai-Ruelle-Bowen (SRB) measure.*

SRB measures are concepts that originally arose in the theory of deterministic, dissipative chaotic systems [31, 135]. They are singular invariant probability distributions supported on a “strange attractor.” Such attractors necessarily have zero phase volume because of dissipation; nevertheless, SRB measures capture the statistical properties of a set of trajectories of positive phase volume (i.e., the strange attractor has a nontrivial basin of attraction). They are the “nicest” invariant probability distributions for such systems in that they have smooth conditional densities along unstable (expanding) phase directions. Indeed, locally they typically consist of the cartesian products of smooth manifolds with Cantor-like fractal sets; the tangent spaces $E_{u,\zeta}(x)$ to these smooth “leaves” are invariant in the sense that $D\Psi_{s,t;\zeta}(x_s) \cdot E_{u,\zeta}(x_s) = E_{u,\zeta}(x_t)$, where $D\Psi_{s,t;\zeta}(x)$ denotes the Jacobian of the flow map at x. Moreover, these subspaces are readily computable as a by-product of estimating Lyapunov exponents (see Appendix A).

Random SRB measures share many of the same properties as SRB measures in the deterministic setting, but are time-dependent. While in principle they may be localized to small regions of phase space, we have found that for our systems this is generally not the case. We thus associate $\lambda_1 > 0$ with unreliability, and hereafter use the terms "chaotic" and "unreliable" interchangeably. (Random SRB measures have also been used to model the distribution of "pond scum"; in that context they are known as "snapshot attractors" [89].)

Although the SRB measure μ_ζ^t evolves with time, it possesses some time-invariant properties because (after transients) it describes processes that are statistically stationary in time. Among these is the dimension of the underlying attractor; another is the number of unstable directions, i.e., the number of positive Lyapunov exponents, which give the dimension of the unstable manifolds of the attractor. The latter will be useful in what follows; we denote it by M_λ .

To summarize, these two theorems allow us to reach global conclusions on the structure of random attractors (singular or extended) using only the maximum Lyapunov exponent λ_1, a measure of linear stability. This has a number of consequences in what follows: first, because λ_1 is a single summary statistic determined only by system parameters (and not specific input realization), it allows us to see quickly the reliability properties of a system across different parameters. Second, it can be computed easily in numerical studies via simulating single trials. Additionally, we note that the Lyapunov exponents for our models are insensitive to the specific realization of the connection matrix A (see numerical methods in Appendix A), consistent with the findings in [87, 76]. However, as we shall discuss later, λ_1 can only tell us about reliability properties in an asymptotic sense (i.e., on sufficiently long timescales).

3.5 Maximum Lyapunov exponents and asymptotic reliability

In line with previous studies [130, 79, 87, 76, 107, 91, 96, 75], we say that a network is *asymptotically reliable* if $\lambda_1 < 0$ and *asymptotically unreliable* if $\lambda_1 > 0$. In principle, even when $\lambda_1 < 0$, distinct trajectories could take very long times to converge to the random sink. However, we note that for all asymptotically reliable networks we

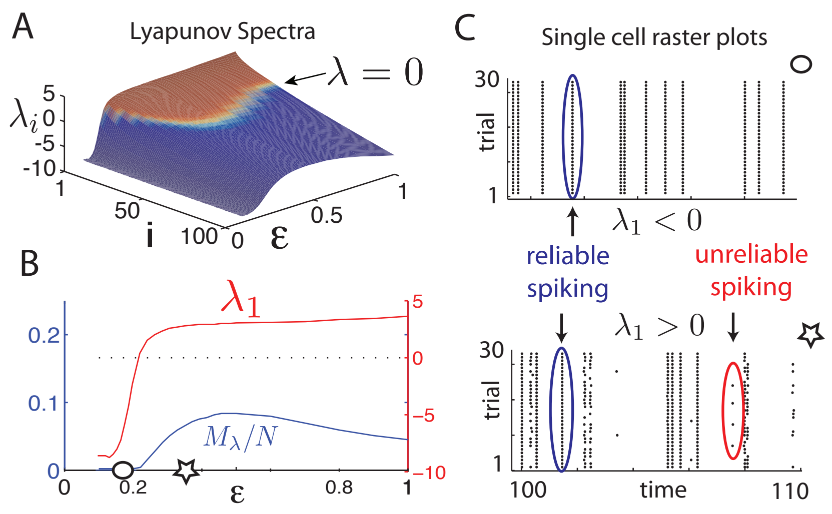

Figure 3.2: (A) First 100 Lyapunov exponents of network with fixed parameters as in Fig. 4.1, as a function of ε. (B) Plot of λ_1 (right scale), M_λ/N: the fraction of $\lambda_i > 0$ (left scale) vs ε. (C) Raster plots show example spike times of an arbitrarily chosen cell in the network on 30 distinct trials, initialized with random ICs. Circle and star markers indicate ε values of 0.18 and 0.5, respectively, shown in panel (B). For all panels, $\eta = -0.5$.

considered, convergence is typically achieved within about 10 time units. For the remainder of the chapter, we will concentrate on "steady state" dynamics and we adopt the point of view that ensembles of solutions for all systems considered were initiated in the sufficiently distant past. The question of transient times, although very interesting, falls outside of the scope of this chapter.

We begin by studying the dependence of the $\lambda_i's$ on the input amplitude ε. Even in simple and low-dimensional, autonomous systems, analytical calculations of λ_i's often prove to be very difficult if not impossible. We therefore numerically compute (see Appendix A for details) the Lyapunov spectra of our network for various values of input drive amplitude ε. Figure 3.2 (A) shows the first 100 Lyapunov exponents of these spectra. This demonstrates that, at intermediate values of ε, there are several positive Lyapunov exponents, and that the trend in this number is nonmonotonic in ε. Panel (B) gives another view of this phenomenon, as well as the dependence of λ_1 on ε. In particular, for sufficiently small ε, the networks produce a negative λ_1. However, as ε increases λ_1 becomes positive, indicating chaotic network dynamics and thus asymptotic unreliability. Consistent with RDS theory, the transition to $\lambda_1 > 0$ is accompanied by the emergence of a random attractor with nontrivial unstable manifolds.

Since the networks we study are randomly connected and each cell is nearly identical, the underlying dynamics are fairly stereotypical from cell to cell. This enables us to focus on a randomly chosen cell for illustrative purposes and further analysis. Figure 3.2 (C) shows two sample raster plots where the spike times of a single cell from 30 distinct trials (initiated at randomly sampled ICs) are plotted. The top plot is produced from an asymptotically reliable system ($\lambda_1 < 0$) and as expected, every spike is perfectly reproduced on all trials. In the bottom plot, where $\lambda_1 > 0$, the spike times are clearly unreliable across different trials, as RDS theory predicts. For the remainder of this chapter, we routinely refer to the parameter sets used in Fig 3.2 (C) as testbeds for stable and chaotic networks respectively, and make use of them for illustrative purposes (see caption of Fig 3.2 for details).

Finally, spike trains from the chaotic network also show an interesting phenomenon: there are many moments where spike times align across trials, i.e., the system is (temporarily) reliable. We now investigate this phenomenon.

3.6 Single-cell reliability

Let us define the i^{th} *neural direction* as the state space of the ith cell, which we identify with a circle S^1 . The degree of reliability of the ith cell is given by the corresponding marginal distribution, i.e., we define a projection $\pi_i(\theta_1, \cdots, \theta_N) = \theta_i$, and denote the corresponding projected single-cell distribution by $p^t_{i,\zeta}(\theta_i) \equiv \pi_i \mu^t_\zeta(\theta)$. Note that when $\lambda_1 > 0$, we expect $p^t_{i,\zeta}$ to be nonsingular, i.e., corresponds to a smooth probability density function (though it may be more or less concentrated); an exception is when the random attractor is aligned in such a way that it projects to a point onto the ith direction. If $p^t_{i,\zeta}$ is singular at time t, then the state of cell i is reproducible across trials at time t; geometrically, trajectories from distinct trials are perfectly aligned in the i^{th} subspace. On the other hand, if $p^t_{i,\zeta}$ has a broad density on S^1, then the state of cell i at time t can vary greatly across trials, and the ith components of distinct trajectories are separated.

This is illustrated in Fig 3.3(A) where snapshots of 1000 randomly initialized trajectories are plotted in two neural subspaces (θ_1, θ_2) at distinct times $t_1 < t_2 < t_3$. The upper snapshots are taken from an asymptotically reliable system ($\lambda_1 < 0$) where μ^t_ζ is singular and supported on a single point (random sink) which evolves on $\mathbb{T}^N$ according to $\zeta(t)$. The bottom snapshots are taken from the $\lambda_1 > 0$ regime and clearly show that distinct trajectories accumulate on "clouds" that change shape with time. These changes affect the spread of $p^t_{i,\zeta}$.

To quantify the effective separation of points in a given neural subspace, we turn to the differential entropy of a projection at time t: $h(p^t_{i,\zeta}) = -\int_{S^1} dp^t_{i,\zeta} \log_2 p^t_{i,\zeta}$. Recall that the differential entropy of a uniform distribution on S^1 is 0, and that the more negative h is, the more singular a distribution. In our context, the more orthogonal the attractor is to the i^{th} direction in $\mathbb{T}^N$, the lower is its projection entropy, as illustrated in Fig 3.3(B). We emphasize again that the shape of $p^t_{i,\zeta}$ is time-dependent and so is its entropy.

3.6.1 Uncertainty in single cell responses

We would like to predict $h(p^t_{i,\zeta})$ from properties of the underlying dynamics. Our first step in doing so is to validate our intuition about the orientation of μ^t_ζ. Following and somewhat generalizing an approach of [87], we use a quantity which we call the *support score* $s_i(t)$ to represent the contribution of a neural direction to the unstable directions of the strange attractor at time t.

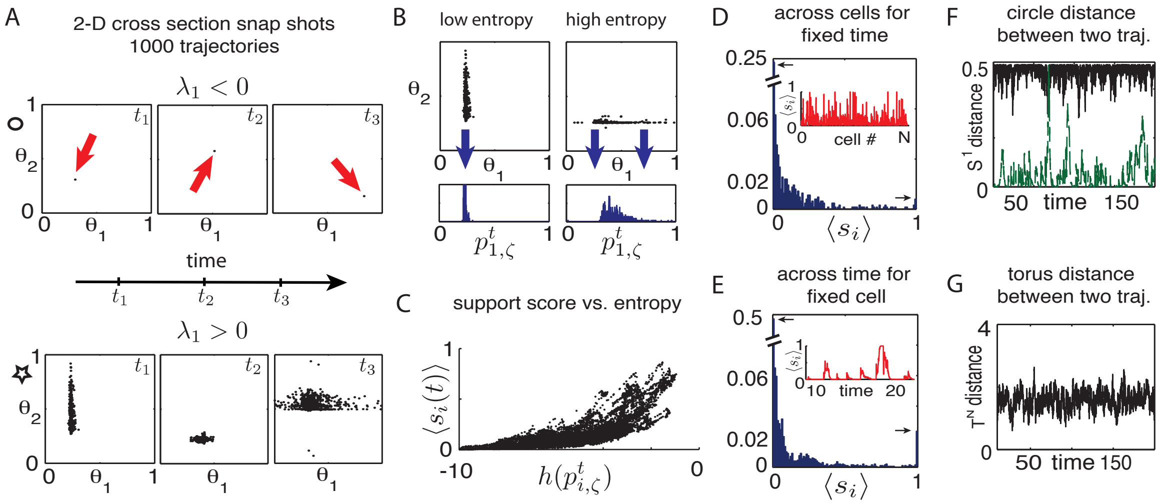

Figure 3.3: (A) Snapshots of 1000 trajectories projected in two randomly chosen neural directions at three distinct times. Upper and lower rows with the same parameters as in Fig 3.2 (C) and show a random sink and random strange attractor respectively. (B) Projection of the sample measure μ^t_ζ in the θ_1 neural subspace. (C): Scatter plot of $\langle s_i(t) \rangle$ vs. $h(p^t_{i,\zeta})$ sampled over 2000 time points and 30 distinct cells. (D): Sample histogram of $\langle s_i \rangle$ sampled across all cells in the network at a randomly chosen moment in time. Inset: snapshot of $\langle s_i \rangle$ vs. cell number i. (E): Sample histogram of $\langle s_i(t) \rangle$ sampled across 2000 time points from a randomly chosen cell. Inset: sample time trace of $\langle s_i(t) \rangle$ vs. time. (F) and (G): Time evolution of distance between two distinct trajectories $\theta^1(t)$, $\theta^2(t)$ (F) Green dashed (bottom): $\|\theta^1_i(t) - \theta^2_i(t)\|_{S^1}$ in randomly chosen θ_i subspace. Black solid (top): $\max_j\{\|\theta^1_j(t) - \theta^2_j(t)\|_{S^1}\}$. (G) $\|\theta^1(t) - \theta^2(t)\|_{\mathbb{T}^N}$. For all panels except A (top), network parameters: $\eta = -0.5$, $\varepsilon = 0.5$ with $\lambda_1 \approx 2.5$.

We first define this quantity locally for a single trajectory $\theta(t)$. For this trajectory, we expect that there exists a decomposition of the tangent space into stable (contracting) and unstable (expanding) invariant subspaces: $E_{s,\zeta}(\theta(t))$ and $E_{u,\zeta}(\theta(t))$. Since the dimension of $E_{u,\zeta}(\theta(t))$ must be M_λ, let $\{v_1, v_2, ..., v_{M_\lambda}\}$ be an orthonormal basis for the unstable subspace at time t (i.e. $v_i \in \mathbb{R}^N$). We define cell i's *support score* as

$$s_i(t) = \|V r_i\| \tag{3.4}$$

where V is the $M_\lambda \times N$ matrix with v_i's as rows and r_i is the (N-dimensional) unit vector in the i^{th} direction. Note that $0 \leq s_i(t) \leq 1$, and that s_i measures the absolute value of the cosine of the angle between the neural and unstable direction. Thus, s_i represents the extent to which the i^{th} direction contributes to state space expansion. The vectors $\{v_1, v_2, ..., v_{M_\lambda}\}$ are computed simultaneously with the λ_i's (see numerical methods in Appendix A).

In order to use the support score to quantify the orientation of the attractor, we need to extend the definition above, which is for a single trajectory, to an ensemble of trajectories governed by μ_ζ^t. However, $s_i(t)$ could greatly vary depending on which trajectory we choose — as we might expect if μ_ζ^t consisted of complex folded structures. Our numerical simulations show that this variation is limited in our networks: the typical variance of an ensemble of $s_i(t)$ values across an ensemble of trajectories with randomly chosen initial conditions is $\mathcal{O}(10^{-2})$ (for a fixed cell i and a fixed time t). This suggests that unstable tangent spaces about many trajectories are similarly aligned. Therefore, we extend the idea of support score to $p_{i,\zeta}^t$ by taking the average $\langle s_i(t) \rangle$ across μ_ζ^t. We numerically approximate this quantity by averaging over 1000 trajectories.

Figure 3.3 (C) shows a scatter plot of $\langle s_i(t) \rangle$ vs. $h(p_{i,\zeta}^t)$ for a representative network that is asymptotically unreliable. This clearly shows that the contribution of a neural direction i to state space expansion results in a higher entropy of the projected measure $p^t_{i,\zeta}$. This phenomenon is robust across all values of ε tested. Once again, we note that this correspondence is not automatic for any dynamical system: there is no guaranteed relationship between the orientation of the unstable subspace and the entropy of the projected density. For example, the restriction of μ^t_ζ to unstable manifolds could be very localized, thus having low entropy for even perfectly aligned subspaces.

3.6.2 Temporal statistics

Next, we inquire about the distributions of $\langle s_i(t) \rangle$ across time and neural directions. That is, again following [87], we study the number of cells that significantly contribute to unstable directions at any moment as well as the time evolution of this participation for a given cell.

Figure 3.3 (D) shows a typical distribution of support scores across all cells in the network at a fixed moment in time. The inset shows a trace of $\langle s_i \rangle$ across cells at that moment. The important fact is that this is distribution is very uneven across neurons, being strongly skewed towards low values of $\langle s_i \rangle$. In panel (E) of the same figure, we see a typical distribution of support scores across time for a fixed cell. The inset shows a sample of the $\langle s_i(t) \rangle$ time trace for that cell. We emphasize that the uneven shape of these distributions implies that at any given moment in time, only a few cells significantly support expanding directions of the attractor and moreover, that the identity of these cells change as time evolves. A similar mechanism was reported for networks of autonomously oscillating cells [87], although only the maximally expanding direction was used to compute $s_i(t)$. In both cases, neurons in the network essentially take turns participating in the state space expansion that is present in the chaotic dynamics.

This leads to trajectories that are unstable on long timescales ($\lambda_1 > 0$), yet alternate between periods of stability and instability in single neural directions on short timescales. To directly verify this, Fig. 3.3 (F) shows a sample time trace of

$\|\theta_i^1(t)-\theta_i^2(t)\|_{S^1}$: the projection distance between two randomly initialized trajectories $\theta^1(t)$ and $\theta^2(t)$ in a single neural direction i. Also shown is $\max_j\{\|\theta_j^1(t)-\theta_j^2(t)\|_{S^1}\}$: the maximal projection distance out of all neural directions. While the maximal S^1 distance is almost always close to its maximum 0.5, the two trajectories regularly collapse arbitrarily close in any given S^1-subspace. This leads to a global separation $\|\theta^1(t)-\theta^2(t)\|_{\mathbb{T}^N}$ that is relatively stable in time (Fig. 3.3 (G)) yet produces temporary local convergence. In what follows, we will see that this mechanism translates into spike trains that retain considerable temporal structure from trial to trial.

3.7 Reliability of spike times

Thus far, we have been concerned in general with the separation of trajectories arising from distinct trials (i.e. different ICs but fixed input $\zeta(t)$). However, of relevance to the dynamical evolution of the network state are spike times: the only moments where distinct neural directions are effectively coupled. Indeed, coupling between cells of this network is restricted to a very small portions of state space, namely to a small interval around $\theta_i = 0 \sim 1$ when a cell spikes (see Model section). This property is ubiquitous in neural circuits and other pulse-coupled systems [51] and is central to the time-evolution of μ_ζ^t.

3.7.1 Spike reliability captured by probability fluxes

From the perspective of spiking, what matters is the time evolution of projected measures on S^1 in relation to the spiking boundary. This is captured by the *probability flux* of $p_{i,\zeta}^t$ at $\theta_i = 0 \sim 1$: $\Phi_i(t)$. For our system, we can easily write down the equation for the flux since inputs to a given cell have no effect at the spiking phase (ie. $Z(0) = 0$ in (3.1)). From (3.1), $\frac{d\theta_i}{dt}|_{\theta_i=0} = 2$ and we have $\Phi_i(t) = 2p_{i,\zeta}^t(0)$. We emphasize that this probability flux is associated with μ_ζ^t, and differs from the usual flux arising from the Fokker-Planck equation. Here, the source of variability between trajectories leading to wider $p_{i,\zeta}^t$ is due to chaotic network interactions, rather than from noise that differs from trial to trial. Overall, $\Phi_i(t)$ is modulated by a complex interaction of the stimulus drive $\zeta(t)$, the vector field of the system itself, and "diffusion" originating from chaos; as we have seen, the latter depends in a nontrivial way on the geometric structure of the underlying strange attractor.

In the limit of infinitely many trials, $\Phi_i(t)$ is exactly the normalized cross-trial spike time histogram, often referred to as the *peri-stimulus time histogram* (PSTH) in the neuroscience literature. A PSTH is obtained experimentally by repeatedly presenting the same stimulus to a neuron or neural system and recording the evoked spike times on each trial. Figure 3.4 (A) illustrates the time evolution of Φ_i. Perfectly reliable spike times (repeated across all trials) are represented by a time t^* such that for an open interval $U \ni t^*$, $\Phi_i(t)|_U = \delta(t - t^*)$. Equivalently, finite values of $\Phi_i(t)$ indicate various degrees of spike repeatability. Of course, $\Phi_i(t) = 0$ implies cell i is not currently spiking on any trial.

3.7.2 Spike events: repeatable temporal patterns

Our next goal is to use $\Phi_i(t)$ to derive a metric of spike time reliability for a network. Intuitively, given a spike observed on one trial, we seek the expected probability that this spike would be present on any other trial. This amounts to asking to what extent the function $\Phi_i(t)$ is "peaked" on average.

To develop a practical assessment of this extent, we begin by approximating $\Phi_i(t)$ from a finite number of trajectories. To do so, we modify the definition of the flux from a continuous to a discrete time quantity. For practical reasons we say that $\Phi_i^{approx}(t)$ represents the fraction of a μ_ζ^t-ensemble of trajectories that crosses the $\theta_i = 1 \sim 0$ boundary within a small time interval $t + \Delta t$. As a discrete quantity, we now have $0 \leq \Phi_i^{approx}(t) \leq 1$. Borrowing a procedure from [125], we convolve this discretized flux with a gaussian filter of standard deviation σ to obtain a smooth waveform (see Fig 3.4 (B)). We then define *spike events* as local maxima (peaks) of this waveform. A spike is assigned to an event if it falls within a tolerance window of the event time,

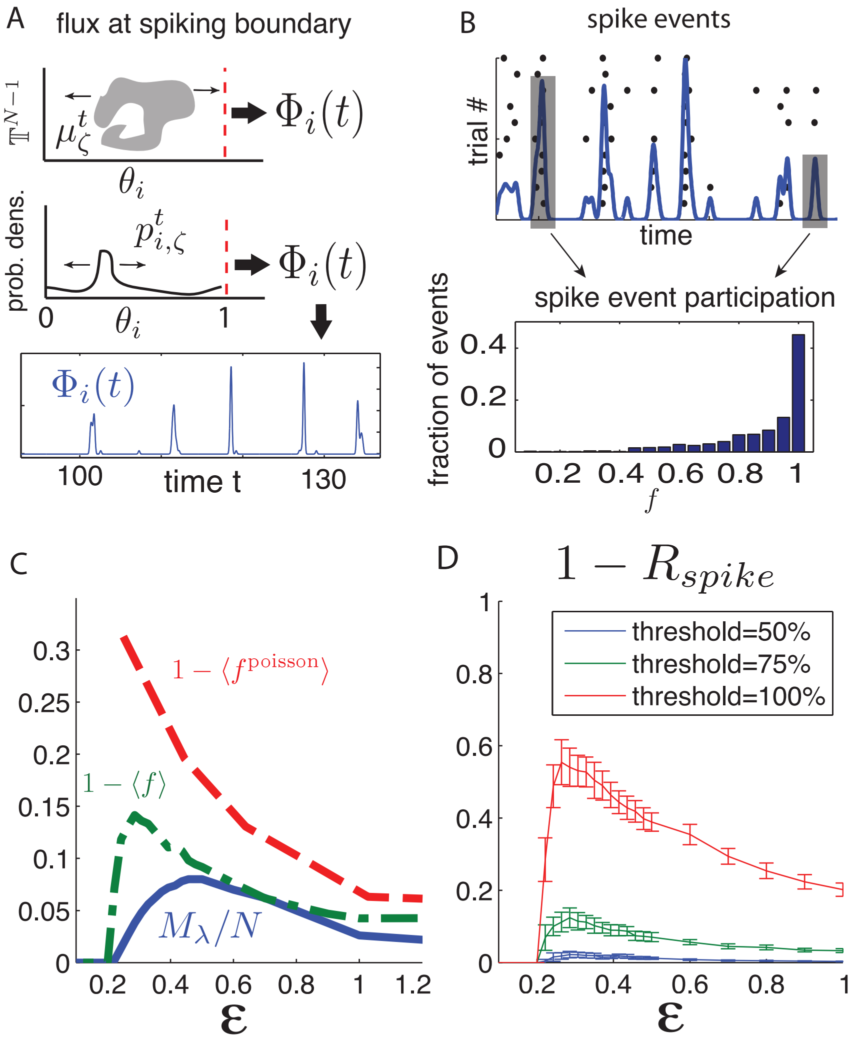

Figure 3.4: (A) Top: cartoon representation of the flux $\Phi_i(t)$. Bottom: sample Φ_i time trace for a randomly chosen cell approximated from 1000 trajectories ($\eta = -0.5$, $\varepsilon = 0.25$, $\lambda_1 \simeq 1.5$) (B) Top: Illustration of spike event definition. Bottom: Distribution of spike event participation fraction f. ($\eta = -0.5$, $\varepsilon = 0.5$, $\lambda_1 \simeq 2.5$) (C) Curves of $1 - \langle f\rangle$ (network) and $1 - \langle f^{poisson}\rangle$ (single cell with random poisson spike inputs) vs. ε. Also shown is the fraction of $\lambda_i > 0$, M_λ/N vs. ε. (D) Mean $1 - R_{\text{spike}}$ vs. ε curves for three threshold values. Error bars show one standard deviation of mean R_{spike} across all cells in the network. ($\eta = -0.5$)

defined by the width of the peak at half height. If the spikes contributing to an event are perfectly aligned, the tolerance is σ. However, if there is some variability in the spike times, the tolerance grows as the event's peak widens. This procedure ensures that spikes differing by negligible shifts are members of the same event. For our estimates, we used $\Delta t = 0.005$ (time step of the numerical solver) and found that $\sigma = 0.05$ was big enough to define reasonable event sizes and small enough to discriminate between most consecutive spikes from the same trial. However, we note that the following results are robust to moderate changes in σ.

Each spike event is then assigned a *participation fraction* f: the fraction of trials participating in the spike event. Figure 3.4 (B) shows the distribution of f's for the events recorded from all cells of our chaotic network testbed, using 2500 time unit runs with 30 trials and discarding the initial 10% to avoid transient effects. There is a significant fraction of events with $f = 1$ and a monotonic decrease of occurrences with lesser participation fractions. The mean $\langle f \rangle$ of this distribution is the finite-sampling equivalent of the average height of Φ_i peaks and therefore represents an estimate of the expected probability of an observed spike being repeated on other trials.

Finally, we compare $\langle f \rangle$ to the number of unstable directions of the chaotic attractor μ_ζ^t for a range of input amplitude ε. Figure 3.4 (C) shows both ε-dependent curves $1-\langle f \rangle$ and M_λ/N (previously shown in Fig 3.2 (B)). For weak input amplitudes ($\varepsilon < 0.2$), networks are asymptotically reliable and thus, $M_\lambda/N = 0$ and every event has full participation fraction ($1 - \langle f \rangle = 0$). As ε increases, the network undergoes a rapid transition from stable to chaotic dynamics. Most interestingly, both $1 - \langle f \rangle$ and M_λ/N follow the same trend, suggesting that the dimension of the underlying strange attractor plays an important role in the expected reliability of spikes. While this relationship is not perfect, it shows that the number of positive Lyapunov exponents serves as a better predictor of average spike reproducibility than the magnitude of λ_1 alone.

The shapes of $1-\langle f \rangle$ and M_λ/N show an initial growth followed by a gradual decay, suggesting that following a transition from stable to chaotic dynamics, higher input fluctuations induce more reliable spiking. In the limit of high ε, this agrees with the intuition of an entraining effect by the input signal. This raises an important question about the observed dynamics: Is spike repeatability simply due to large deviations in the input? Or equivalently, is the role of chaotic network interactions comparable to "noise" in the inputs to individual neurons? That this may not be the case for moderate input amplitudes is suggested by the concentration of trajectories in the sample measures μ_ζ^t. We now seek to demonstrate the difference.

3.8 Relevant local mechanisms

3.8.1 Network interactions vs. stimulus

A natural question about the dynamical phenomena described above is: to what extent are they caused by network interactions, compared to direct effects of the stimulus? In our system, each cell receives an external stimulus $\zeta_i(t)$ as well as a sum of inputs from other cells. Because of network interactions, the latter inputs are highly structured even when $\lambda_1 > 0$, and can be correlated across multiple trials. Indeed, all else being equal, the more singular and low-dimensional μ_ζ^t is, the more cross-trial correlation there will be. The question is whether we would still observe the same spiking behavior when inputs from the rest of the network are replaced by more random inputs.

To test this, we compare the response of cell i in a network driven by the stimulus $\zeta(t)$ with that of a single "test cell" driven by (i) the ith component $\zeta_i(t)$ of the given stimulus, plus (ii) excitatory and inhibitory poisson-distributed spike trains designed to mimic network inputs, but are independent across trials. More precisely, the poisson spike trains are adjusted to the network firing rate (modulated by ε) and have inter-spike interval distributions matching those of network-embedded cells (see Fig 4.1 (B)). The number of poisson spike trains received by the test cell matches the mean in-degree K of the network and the balance between excitation and inhibition is conserved. Importantly, all trains are independent (both within and across trials). The average spike event participation fraction $\langle f^{poisson} \rangle$ is then computed.

Fig 3.4 (C) shows $1 - \langle f^{poisson} \rangle$ alongside $1 - \langle f \rangle$. For moderate values of ε, these two curves differ by a factor of two and slowly converge as ε increases. This confirms that two dynamical regimes are present: When the input strength is very high, inputs tend to entrain neurons into firing regardless of synaptic inputs, as was intuitively stated above. However, for moderate input amplitudes, network interactions play a central role in the repeatability of spike times. Importantly, we note that many repeatable spike events in chaotic networks are not present in the surrogate poisson-driven cell presented with the same stimulus.

A second, closely related question is whether the reliable spiking events we see are solely due to large fluctuations in the stimulus, or if network mechanisms play a significant role. The above results, which show that structured network interactions can have a significant impact on single-cell reliability, suggest the answer is no. Here we provide a second, more direct test of this question.

To proceed, we first classify each spike fired in the network as either reliable or not by defining a quantity R_{spike}: the fraction of spikes belonging to an event with a participation fraction f greater or equal to some threshold. R_{spike} is the cumulative density of events with f greater than the chosen threshold. Equivalently, we say a spike event is *reliable* if its f is greater than that threshold and *unreliable* otherwise. Individual spikes inherit the reliability classification of the event of which they are a member.

For visual comparison with Fig 3.4 (C), Fig 3.4 (D) shows $1 - R_{\text{spike}}$ as a function of ε for three threshold values (0.5, 0.75 and 1). These curves show the fraction of unreliable spikes, out of all spikes fired, for a given threshold. The error bars show the standard deviation of the value across all cells in the network. As expected for small ε, $1 - R_{\text{spike}} = 0$ since $\lambda_1 < 0$. Notice that as in the case of $1 - \langle f \rangle$, the distinct choices of threshold do not affect overall trends, but they greatly impact the fraction of spikes labeled reliable (or unreliable). For what follows, we adopt a strict definition of spike time reliability by fixing the R_{spike} threshold at 1 (i.e. a spike is reliable if it is present in all trials). However, the subsequent results are fairly robust to the choice of this threshold.

We can now address the question raised above via *spike-triggered averaging* (STA). As the name describes, this procedure takes quantities related to a given cell's dynamics (i.e. stimulus, synaptic inputs, etc.) in the moments leading to a spike, and averages them across an ensemble of spike times. In other words, it is a conditional expectation of the stimulus in the moments leading up to a spike; it can also be interpreted as the leading term of a Wiener-Volterra expansion of the neural response [102]. In what follows, we will distinguish between reliable and unreliable spikes while taking these averages in an effort to isolate dynamical differences between the two.

For illustration, we turn to our chaotic network testbed. Figure 3.5 (A) and (B) shows the STA of both excitatory and inhibitory network interactions as well as the external input leading to reliable and unreliable spikes. More precisely, say we consider spike times $\{t_i^1, t_i^2, ...\}$ from cell i. Then the network interactions used in the STA is the ensemble of time traces $\{Z(\theta_i(t)) \sum_j a_{ij} g(\theta_j(t)) | t_i^* - 2 \leq t \leq t_i^*\}$ where $Z(\theta)$ and $g(\theta)$ are as in (3.1) where we differentiate between excitatory and inhibitory inputs according to the sign of a_{ij}. Similarly, the external input are taken from $\{\varepsilon Z(\theta_i(t)) \zeta_i(t) | t_i^* - 2 \leq t \leq t_i^*\}$.

There are two main points to take from these STAs. First, note that the spike-triggered recurrent excitation is stronger than the spike-triggered stimuli, giving further evidence that recurrent interactions shape the dynamics with which the spikes themselves are elicited — rather than spikes being primarily driven by the external stimuli alone. Second, note that these STAs are qualitatively similar for both reliable and unreliable spikes. This suggests that we look for further effects on stability that distinguish these two cases, a task to which we now turn.

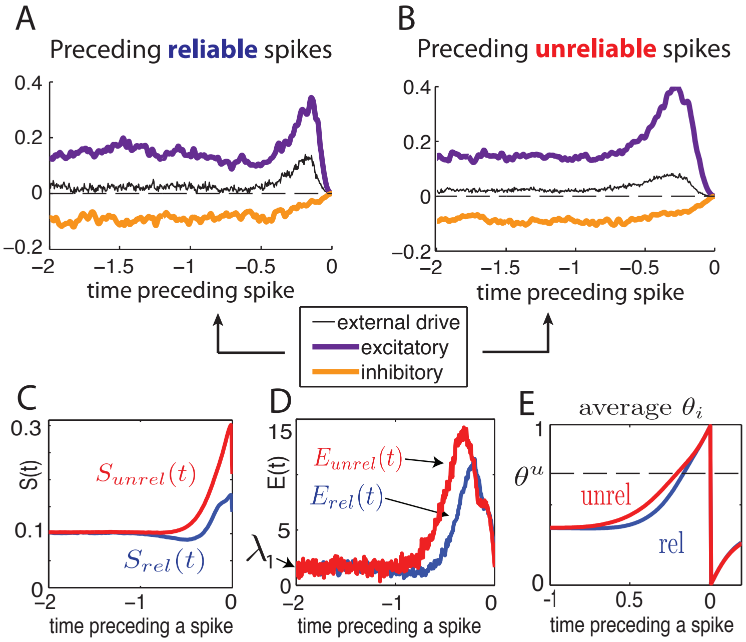

Figure 3.5: For (A) through (E), $t = 0$ marks the spike time and rel/unrel indicates the identity of the spike used in the average. (A) and (B), Spike triggered averaged external signal $\varepsilon Z(\theta_i)\zeta_i(t)$ (black), excitatory (purple) and inhibitory (orange) network inputs $Z(\theta_i)\sum_j a_{ij}g(\theta_j)$. (A) Triggered on reliable spikes. (B) Triggered on unreliable spikes. (C) Spike triggered support score S. (D) Spike triggered local expansion measure E. (E) Spike triggered average phase θ_i. For all panels: $\eta = -0.5$, $\varepsilon = 0.5$ with $\lambda_1 \approx 2.5$.

Recall that the support score $s_i(t)$ measures the contribution of a single cell's subspace to tangent unstable directions of a trajectory. Consider the corresponding STA $S(t)$, i.e., the expected values of $s_i(t)$ in a short time interval preceding each spike in the network. Fig. 3.5 (C) shows the resulting averages for both reliable and unreliable spikes. Moments before a cell fires an unreliable spike, $S(t)$ is considerably larger than in the reliable spike case, thus indicating that global expansion is further aligned with a spiking cell's direction in unreliable spike events. We now investigate properties of the flow leading to this phenomenon.

3.8.2 Source of local expansion

To better capture space expansion in a given neural direction, consider $v(t)$, the solution of the variational equation

$$\dot{v} = J(t)v \tag{3.5}$$

where $J(t) = D\Psi_{0,t;\zeta}$ is the Jacobian of the flow evaluated along a trajectory $\theta(t)$. If we set $v(0)$ to be randomly chosen but with unit length, then $v(t)$ quickly aligns to the directions of maximum expansion in the tangent space of the flow about $\theta(t)$; moreover, because of ergodicity $\lambda_1 = \lim_{t\to\infty} \frac{1}{t}\log(\|v(t)\|)$. We can equivalently write a discretized version of this expression for small Δt: $\lambda_1 = \lim_{T\to\infty}\langle e(t)\rangle_T$ where $\langle\cdot\rangle_T$ denotes the time average up to time T and $e(t) = \frac{1}{\Delta t}\log\left(\frac{\|v(t+\Delta t)\|}{\|v(t)\|}\right)$ is analogous to a finite time Lyapunov exponent. For our network, $e(t)$ fluctuates rapidly and depends on many factors such as number of spikes fired, the pattern of the inputs, and the phase coordinate of each cell over the time Δt. Its coefficient of variation is typically $\mathcal{O}(10)$ for $\Delta t = 0.005$ which is consistent with the fact that stability is very heterogeneous in time. To better understand the impact of the flow on a single cell's subspace, we define the *local expansion coefficient*

$$e_i(t) = \frac{1}{\Delta t} \log\left(\frac{|v_i(t+\Delta t)|}{|v_i(t)|}\right). \tag{3.6}$$

Note that $e_i(t)$ is a local equivalent of $e(t)$ and directly measures the maximum expansion in a neural subspace.

Consider the corresponding STA $E(t)$, shown in Fig. 3.5 (D). Notice that $E_{\text{unrel}}(t)$'s peak is much broader than $E_{\text{rel}}(t)$'s with $\int_{-2}^{0} E_{\text{unrel}}(t) - E_{\text{rel}}(t)dt \simeq 2.5$ which indicates that prior to an unreliable spike, trajectories are subject to an accumulated infinitesimal expansion rate higher than in the reliable spike case.

In contrast to $s_i(t)$, $e_i(t)$ is directly computable in terms of contributions from different terms in the flow. We refer the reader to Appendix A for a detailed treatment of input conditions leading to reliable or unreliable spikes. Importantly, the source of "local" expansion $e_i(t)$ is dominated by the effect of a single cell's vector field $F(\theta_i)$ (from Eqn. (3.1)) which directly depends on the phase trajectory $\theta_i(t)$ prior to a spike.

If $\theta_i(t) < \frac{1}{2}$, $F'(\theta_i(t))$ is negative, and becomes positive for $\theta_i(t) > \frac{1}{2}$ — in the absence of fluctuating inputs from network or external source. When an uncoupled cell is driven by ζ_i, we know that on average, it spends more time in its contractive region ($\theta_i < \frac{1}{2}$) and is reliable as a result [75, 107]. While inputs may directly contribute to $J(t)$, their effect is generally so brief that their chief contribution to $e_i(t)$ is to steer $\theta_i(t)$ in expanding regions of its own subspace (see Appendix A). Fig 3.5 (C) confirms that on average, the phase of a cell preceding an unreliable spike spends more time in its expanding region. Such a phenomenon has previously been reported in the form of a threshold crossing velocity argument [6].

The key feature of this driven system, likely due to sparse and rapid coupling, is a sustained balance between inputs leading to contraction/expansion in local neural subspaces. A bias toward more occurrences of "expansive inputs" yields positive Lyapunov exponents ($M_\lambda > 0$) and implies on average, more growth than decay.

What is perhaps surprising is that this state space expansion remains confined to subspaces supported by only a few neural directions, which creates this coexistence of chaos and highly reliable spiking throughout the network.

3.9 Discussion

In this chapter, we explored the reliability of fluctuation-driven networks in the excitable regime — where model single cell dynamics contain stable fixed points. We showed that these networks can operate in stable or chaotic regimes and demonstrated that spike trains of single neurons from chaotic networks can retain a great deal of temporal structure across trials. We have found that an attribute of random attractors that directly impacts the reliability of single cells is the orientation of expanding subspaces, and that the evolving shape of the random attractor is reflected in the intermittent reliability of single neurons. We have also performed a detailed numerical study to analyze the local (i.e., cell-to-cell) interactions responsible for reliable spike events.

What remains to be understood is the role of larger-scale network structures, and how unreliable spike events propagate through the network in a self-sustaining fashion in networks with $\lambda_1 > 0$. This is a target of our future work.

Throughout this work, we have found the qualitative theory of random dynamical systems to be a useful conceptual framework for studying reliability. Though the theory is predicated on a number of idealizations, we expect most of them (e.g., the assumption that the stimuli are white noise rather than some other type of stochastic process) can be relaxed.

Finally, we note that the phenomena observed here may have consequences for neural information coding and processing. In particular, unreliable spikes are a hallmark of sensitivity to initial conditions and may therefore carry information about previous states of the system (or, equivalently, previous inputs). In contrast, reliable spikes carry repeatable information and computations about the external stimulus

$\zeta(t)$ (either via directly evoked spikes or propagated by repeatable network interactions). We showed that both unreliable and reliable spike events coexist in chaotic regimes of the system explored. Preliminary results indicate that correlation across external drives greatly enhances a network's spike time reliability and will be the object of an upcoming publication. The resulting implications for the neural encoding of signals are an intriguing avenue for further investigation.

Chapter 4

STRUCTURED CHAOS SHAPES SPIKE-RESPONSE NOISE ENTROPY OF DRIVEN BALANCED NETWORKS

4.1 Overview

Chapter 3 presented an analysis of spike-time reliability in driven chaotic networks. There, we focussed on the expected variability of single spikes, leaving open the question of the statistical properties of joint spike patterns involving multiple neurons.

In this chapter, we derive a bound for the entropy of joint spike pattern distributions, in the same setting as before – that is, large recurrent networks of theta neurons in response to a fluctuating temporal signal. The analysis is based on results from random dynamical systems theory and complemented by detailed numerical simulations. We find that despite very weak conditional correlations between neurons, the resulting joint variability of network responses is much lower than what would be extrapolated from estimates based on single neurons or cell pairs. This result provides insight into potential mechanisms by which neuronal networks in the brain may encode information about temporally structured stimuli.

The contents of this chapter are taken in part from a manuscript entitled *Structured chaos shapes neuronal spike-response noise entropy of driven balanced networks*, by Guillaume Lajoie, Jean-Philippe Thivierge and Eric Shea-Brown and is submitted for review. Special thanks go to Fred Wolf, Yu Hu and Kevin K. Lin for helpful insights. This work was supported in part by an NSERC graduate scholarship, an NIH Training Grant from the University of Washington's Center for Computational Ceuroscience, the Burroughs Wellcome Fund Scientific Interfaces, and the NSF under grant DMS-0907927. Numerical simulations were performed on NSF's XSEDE supercomputing platform.

4.2 Introduction

If a temporally fluctuating signal is presented to a network whose dynamics are chaotic, how much variability can one expect in its responses — given that initial states are unknown? This question is central to questions of stimulus encoding by large recurrent networks of neurons in the brain. Here, the conditional distributions, which describe the joint activity of many connected neurons in response to an input, are often extremely complex. In this chapter, we present results that leverage properties of high-dimensional chaotic attractors to approximate the entropy of these distributions. This bypasses the need for statistical sampling of network outputs, which is an exponentially complex problem. The conclusions provide insight into how large networks may carry and encode information about temporal features of driving signals.

Some sensory systems depend on the precise timing of spikes — large and rapid changes in a neuron's membrane potential — to process stimuli that contain temporal cues [45]; and isolated neurons are known to respond to fluctuating input currents with reliable spike patterns [16, 81]. However, variability in stimulus-evoked spikes is increasingly pronounced in deeper, more recurrently connected brain areas such as cortex [63]. How much of this variability is intrinsic to the network? How might this constrain spiking features relevant for coding? These remain important open questions.

In vivo experiments where fluctuating sensory stimuli are repeatedly presented to an animal reveal that cortical neurons can produce spikes with a wide range of variability, and that some are repeatedly evoked with millisecond precision but not others [134, 101]. Information-theoretic methods based on temporal spike binning suggest that this type of "intermittent noise" may still allow spike-timing based information to be encoded by single cortical cells [101]. However, recent studies suggest that the impact of noise on network coding cannot be understood by considering single-cell responses in isolation [113, 30, 136]. Rather, it is essential to understand the simultaneous, *joint* statistics of many cells, and the network mechanisms that shape these statistics.

Cortical networks produce sustained, irregular spikes across neurons [18], a phenomenon which is believed to arise from a balance between excitatory and inhibitory connections [116]. *Balanced state* network models produce irregular spiking, generating chaotic dynamics when activity is driven by constant external excitation [130, 87]. Moreover, this chaos induces high sensitivity to small perturbations even in the absence of external noise. This sensitivity is an obvious threat to encoding of signals based on precise spike times [79]. However, recent work shows that temporally driven balanced networks can have chaotic attractors of limited dimension and geometric properties leading to intermittent periods of reliable spiking (see Chapter 3).

Attractor dimension is intimately linked to dynamical entropy production in chaotic systems. Entropy production is a measure of uncertainty in the predictability of trajectories in the state space of network models. This type of trajectory "noise" is what leads to spike variability in balanced network models [87]. To link this concept with neural coding, we need to make a quantitive link between levels of entropy production in state space, and the variability (entropy) in stimulus-evoked spike patterns — also called *noise entropy* [102].

In this chapter, we use random dynamical system theory and numerical estimates to develop an approximate bound for the noise entropy of spike trains in stimulus driven, balanced networks of spiking neurons. We show that: (i) Joint spike train noise entropy is surprisingly lower than what one would obtain by extrapolating estimates based on single neurons or cell pairs considered separately. (ii) This phenomenon is network-size invariant, a feature arising from the extensive nature of chaos in balanced networks [87]. (iii) Entropy production, and hence bounds on spike train noise entropy, strongly depends on the level of temporal structure and mean values of input signals. Overall, our results describe dynamical properties of balanced, chaotic networks that limit variability in their joint spike train responses, raising the possibility that these responses could carry information about stimuli in a wide range of network scales.

4.3 Network model

We study large random networks of N θ-neurons as in [87] and Chapter 3. The state of each cell is represented by a phase variable $\theta_i(t) \in [0,1]$ where 0 and 1 are identified (i.e. S^1) and a spike is said to occur when $\theta_i = 1 \sim 0$. This model has non-dimensionalized units but is equivalent to the Quadratic Integrate-and-fire model after a smooth change of coordinates [33] (see also Appendix A). In addition, the network receives a temporally structured input $I(t)$ described below. As in Chapter 3, the dynamics of the i^{th} cell in the network is given by a random dynamical system represented by

$$\begin{aligned} d\theta_i = &\left[F(\theta_i) + Z(\theta_i) \sum_{j=1}^{N} a_{ij} g(\theta_j) + \frac{\varepsilon^2}{2} Z(\theta_i) Z'(\theta_i) \right] dt... \\ &+ Z(\theta_i) \underbrace{[\eta dt + \varepsilon dW_i]}_{I_i(t)} . \end{aligned} \tag{4.1}$$

Here, $F(\theta_i) = 1 + \cos(2\pi\theta_i)$, $Z(\theta_i) = 1 - \cos(2\pi\theta_i)$ and $g(\theta_j)$ is a smooth coupling function with small support around $\theta_j = 1 \sim 0$ ($[-1/20, 1/20]$) mimicking the rapid rise and fall of a synaptic current (see Appendix B for details). The ε^2 term comes from an Ito correction [77]. We assign 20% of the N neurons to be inhibitory and 80% to be excitatory, meaning that outgoing weights of neuron j are either $a_{ij} \leq 0$ or $a_{ij} \geq 0$ respectively. The coupling matrix $A = \{a_{ij}\}_{i,j=1,\dots,N}$ is chosen randomly with mean *in-degree* κ such that each neuron receives on average κ incoming connections from independently chosen neurons from each excitatory or inhibitory population. For the rest of this chapter, we ensure that $\kappa \ll N$ and that $|a_{ij}| \sim \mathcal{O}(1/\sqrt{\kappa})$ when nonzero, in accordance with the classical *balanced state* architecture [130]. Throughout, we set $\kappa = 20$ and find that as long as $\kappa \ll N$, our results are qualitatively robust.

The network input $I = \{I_i\}_{i=1}^N$, represented by the last term in (4.1), mimics a temporally varying vector-valued stimulus. It is a collection of N independent signals $I_i(t) = \eta + \varepsilon\omega_t^i$ driving each neuron, where the ω_i are "frozen" or "quenched" white noise realizations arising from the independent Wiener processes W_i. We emphasize that $I = \{I_i\}_{i=1}^N$ is a signal with Gaussian statistics but not stochastic noise. In what follows, we study the behavior of many trajectories of (4.1) driven by the same input I but starting from distinct initial conditions.

Parameters η and $\varepsilon \geq 0$ are constant across all cells and represent the mean and fluctuation amplitude of I respectively. Note that η controls the network's "excitability" and can take negative values. When $\eta < 0$, we say the network is in the *excitable* regime as intrinsic single-cell dynamics contain a stable equilibrium (rest) and an unstable one (threshold). When $\eta > 0$, the network is in the *oscillatory* regime as each neuron has an intrinsic firing frequency that grows as $\sqrt{\eta}$. We begin by investigating network (4.1) in the excitable regime with parameters $\eta = -0.5$ and $\varepsilon = 0.5$.

4.4 Spike response noise entropy

In order to quantify spike pattern variability, it is convenient to treat spike trains as binary time series. We discretize time in bins of width Δt that are not infinitesimally small, but are small enough so that for a given cell, each bin contains at most a single spike. Let us first define finite binary words for K neurons over L time bins starting at time $t_l = l\Delta t$ for some integer l: $S_{KL}(t_l) = \{S_l^k, ..., S_{l+L-1}^k\}_{k=k_1,...,k_K}$ with $S_j^k \in \{0,1\}$ (see Figure 4.1 (a)). The variability of the evoked spike response $S_{KL}(t_l)$ is captured

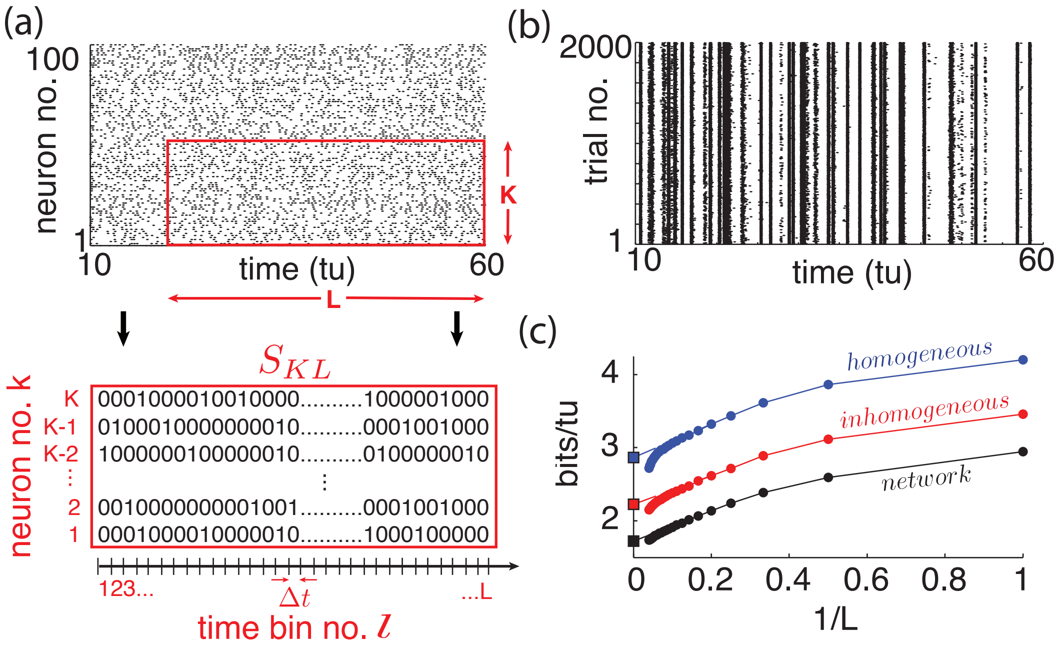

Figure 4.1: (a) Top: Raster plot of spike output for 100 randomly selected neurons for 50 time-units (tu) on a single trial (dots are spikes). Bottom: Illustration of binary S_{KL}-word. (b) Raster plot of a randomly selected cell's spike output on 2000 trials, where only network initial conditions change from trial to trial. (c) Single cell H^{1L}_{noise} estimates for different surrogate noise test. From top to bottom: homogeneous poisson (blue), inhomogeneous poisson (red), network interactions (black). The word length is plotted in inverse, $1/L$, to better visualize extrapolation of extensive regime to $L \to \infty$ (left square markers). For all panels: $\eta = -0.5$, $\varepsilon = 0.5$, $N = 500$.

by the conditional *noise entropy* given the input I

$$H^{KL}_{noise}(t_l) = \frac{-1}{KL\Delta t} \sum_{S_{KL}} P(S_{KL}(t_l)|I) \log_2 P(S_{KL}(t_l)|I), \tag{4.2}$$

where $P(\cdot)$ denotes probability given a random initial state of the network. This quantity is normalized to have units of bits per neuron per time unit ($bits/neuron/tu$) and thus represents an entropy rate. Since the inputs I and network dynamics are statistically stationary processes (see Chapter 3), it follows that the expected noise entropy rate of KL words conditioned on any I from the same input distribution — controlled by the parameters η and ε — can be obtained from an average for a single I, provided the time-average is sufficiently long (see eg. [119, 102]):

$$H_{noise}^{KL} = \lim_{T \to \infty} \frac{1}{T} \sum_{l=0}^{T-1} H_{noise}^{KL}(t_l). \tag{4.3}$$

As demonstrated in [119] and reviewed below, (4.3) can be used to estimate the true entropy rate of the K neurons considered when $L \to \infty$. Our goal is to better understand this quantity for entire networks ($K = N$) as network size N grows.

4.5 Empirical estimates of noise entropy in spike trains

Our first goal is to generate empirical estimates of noise entropy rates from simulated network data. To this end, we numerically integrate Equation (4.1) to generate ensembles of solutions driven by the same input I, but starting from distinct initial conditions (IC). We want to choose such ICs so that they represent the most likely states in which one may find an active network at any moment.

As described in more detail below (see Section 4.6), the network is expected to have a stationary probability distribution. This distribution describes the likelihood of finding the system in a particular state, given any input history sharing the same statistics. To sample random ICs from this distribution, we first select seed ICs uniformly over the state space, and evolve each of these for a “burn in” period of 50 time units, for which different inputs I are presented. After this transient period, the resulting endpoints of these trajectories represent a new IC ensemble that approximates the stationary distribution. We make sure to sample from the stationary distribution to be consistent with technical requirements in Section 4.6. However in practice, the initialization details make little difference. Indeed, after short transients (about 10 time units), the quantities we compute below seem insensitive to IC statistics, as long as they are reasonably spread over the state space.

With the stationary IC ensemble, we simulate network (4.1) in response to a fixed I for 10000 time units and 2000 trials — where trials are distinguished only by their ICs (see Appendix B for computational details). We discretize time in bins of width $\Delta t = 0.05$ time units and extract the binarized spike outputs S_{NL} on all trials. Note that a detailed study of temporal resolution of spike trains falls outside the scope of this study. Nevertheless, we found that a slightly different time-bin resolution did not significantly affect our results. We now have ensembles of binarized network spike patterns S_{NL} in response to a long input I, which we use to probe characteristics of chaos-induced noise entropy rate in various contexts.

4.5.1 Chaos-induced single neuron variability

When considered in isolation, the uncoupled θ-neuron model of a single cell is known to produce reliable spike responses to frozen-noise inputs I_i. In other words, after short transient periods, the spike trains produced from different initial conditions are all the same [75, 107]. Therefore, any variability observed in the responses of single neurons that are part of coupled networks is a result of chaotic network interactions. To better understand this mechanism, we compare the chaotic variability induced by network interactions with commonly used noise paradigms at the single cell level.

As the number of inbound connections to each cell is the same on average, the dynamics of any single neuron in a balanced network are stereotypical, and its statistics are representative of any other cell's. Thus, we randomly select a neuron i from our network and numerically estimate its noise entropy rate H^{1L}_{noise}. Using the simulated network dynamics, we extract the binarized spike output of our selected cell on all trials (see Figure 4.1 (b)). For a fixed L, we use the normalized cross-trial counts of S_{1L} words in consecutive, non-overlapping L-windows as estimates of the probabilities $P(S_{1L}(t_l|I))$ in equation (4.2). We repeat this process for word lengths up to $L = 20$ and plot the results in Figure 4.1 (c) as a function of $1/L$.

A system with finite autocorrelation timescales is expected to produce entropy rates that behave extensively as L gets large enough. This is readily apparent in the linear decreasing trend in H_{1L} as L grows, until a point where the estimate quickly drops due to insufficient sampling. Following [119], we use the point of least fractional change in slope to extrapolate this extensive trend and obtain an estimate for $\lim_{L\to\infty} H^{1L}_{noise}$ (intersections with ordinate in Figure 4.1 (c)). This approximates the noise entropy for spike trains of single cells drawn from within the chaotic network.

We repeat the process of estimating noise entropy in the spike trains of single cells. However, rather than doing this for a single neuron drawn from an entire chaotic (but deterministic) network, we compute the noise entropy for cells driven with different noise models. The point is to compare variability produced by chaotic networks to that produced by "typical" noise models. Specifically, we model a single neuron keeping the input I_i intact but replacing the incoming spike trains it receives from upstream cells by two surrogate ensembles meant to isolate distinct "noisy" statistical features of network activity. First we consider (i) *homogeneous* noise surrogates: independent, Poisson distributed spike trains with rates that match the mean firing rate of the cells providing input to the neuron at hand. Next we consider (ii) *inhomogeneous* noise surrogates, produced by independently drawing a binary random variable in each Δt-bin, according to the time-dependent probabilities (PSTHs) of upstream cells, measured from the original network simulations. For each new trial, we draw independent surrogates.

Figure 4.1 (c) shows the results. Compared with the noise entropy produced by the cell when embedded in the chaotic network, there is a 66% increase in noise entropy rate when instead, it receives noisy inputs according to the homogeneous surrogates, and about 30% for the inhomogeneous case. These sizable differences indicate that while chaotic dynamics produce variable responses, these contain a significant structure which is not entirely explained by instantaneous firing rates across the network.

4.5.2 Noise entropy and network interactions

We investigate how statistical dependencies in spike trains from different cells may affect the variability of the joint network spike output. Because our network is sparsely connected ($\kappa \ll N$), dynamical interactions are limited, raising the question of whether such interactions impact the "global" multi-cell spike entropy rate $\lim_{L\to\infty} H_{noise}^{NL}$ at all. As a first investigation into this matter, we consider the Pearson correlation coefficient $c_{ij}(t_l)$ between the spiking probability of two cells i and j in time-bin t_l. This measures the instantaneous *noise correlation* in their spike outputs.

Figure 4.2 (a) shows a typical histogram of $c_{ij}(t_l)$ across all neuron pairs in a network with $N = 500$ for a fixed t_l, where pairs with zero spiking probability were discarded. This gives one view into spike correlations across the network. However, we note that correlations are not static in the sense that a high correlation between two cells in one time-bin does not guarantee that they are correlated in the future. This is illustrated in Figure 4.2 (b) showing a histogram of $c_{ij}(t_l)$ across 10000 time units, for two randomly chosen (connected) cells. Notice that both histograms in Figure 4.2 are strikingly similar, suggestive of ergodic network dynamics. Importantly, the average $\langle c_{ij}(t_l)\rangle$, computed over 4950 random pairs and 500 time units, is of the order of 10^{-5} while $\langle |c_{ij}(t_l)|\rangle$ is about 10^{-2}. Thus, we can see that correlated variability among neurons is fairly small, at least according to these averages.

These limited and evolving pairwise spike correlations are attributable to the shape and size of chaotic attractors that describe network trajectories originating from distinct ICs. Indeed, it was shown in [87] and Chapter 3 that for chaotic balanced networks, only a few cells contribute to state space expansion at any given moment and that the identity of these neurons changes with time. It is not clear, however, whether such limited dependencies collaborate to significantly lower the noise entropy rate of the network spike trains as a whole — i.e., across many cells, and across time.

To begin to address this, we first note that the entropy of a multivariate dis-

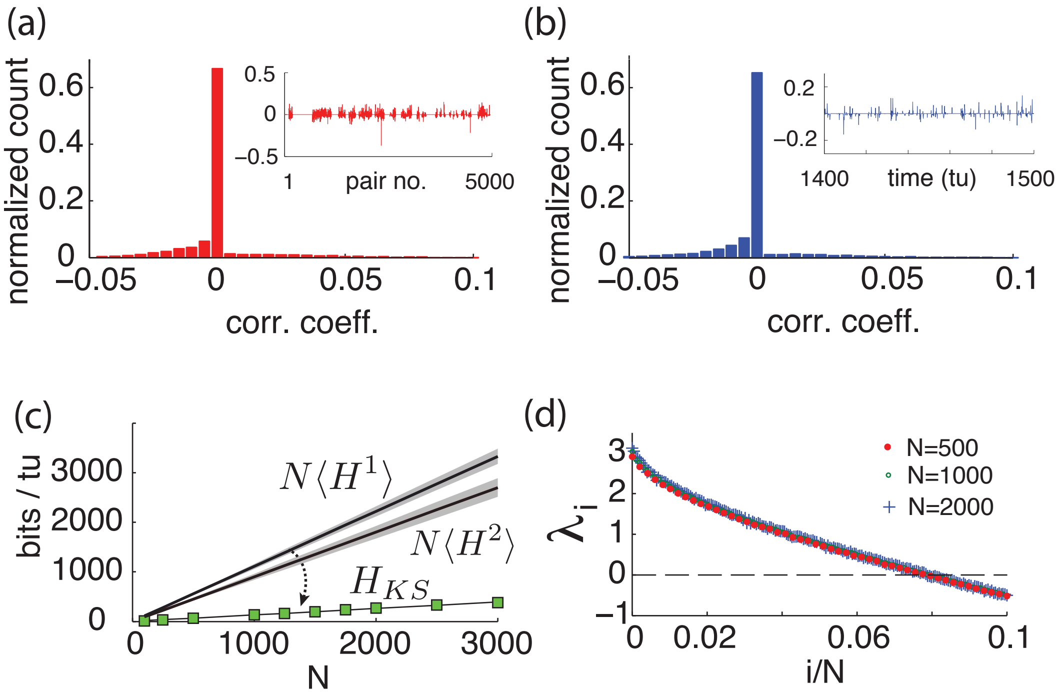

Figure 4.2: (a) Typical histogram of noise correlation coefficients $c_{ij}(t_l)$ between all neuron pairs for a fixed time. Inset shows $c_{ij}(t_l)$ for the first 5000 pairs. (b) Histogram of noise correlation coefficient $c_{ij}(t_l)$ between two connected cells across 10000 tu. Inset shows $c_{ij}(t_l)$ for 100 tu. (c) Network-wide noise entropy estimates in $bits/tu$. Estimate from single cell noise entropies $\langle H^1\rangle$ (averaged over 20 random cells), estimate from two-cells noise entropy $\langle H^2\rangle$ (averaged over 45 random cell pairs) with shaded area showing one standard error of the mean ($N = 500$). KS-entropy estimate H_{KS}: markers shows estimates from Lyapunov spectra for a range of N; black line is a linear fit. (d) Plot of first 10% of Lyap spectrum for $N = 500$, 1000 and 2000. For all panels: $\eta = -0.5$, $\varepsilon = 0.5$.

tribution is always greater than or equal to the sum of the marginal distributions' entropies. It follows that a "naive" extrapolation of entropy estimated from one or a few cells at a time can produce nested upper bounds on the joint network entropy rate. Specifically, if $\langle H^K\rangle$ denotes the average of $\lim_{L\to\infty} H^{KL}_{noise}$ over all K-tuples, then $\langle H^1\rangle \geq \langle H^2\rangle \geq ... \geq \langle H^N\rangle$, all with units of bits per time unit per neuron.

However, since connectivity is small compared to network size, it is reasonable to expect that these decreasing estimates saturate for K large enough. Indeed, this has to be the case if noise entropy rate is extensive in N. Assuming this is true, $N\langle H^K\rangle$, for sufficiently large K, serves as an upper bound on the total noise entropy rate of networks when N is large. Figure 4.2 (c) shows estimates of such bounds for $K = 1, 2$ as a function of N. Here, the slopes $\langle H^1\rangle$ and $\langle H^2\rangle$ are sampled over 20 randomly selected neurons and 45 neuron pairs in a network with $N = 500$, using the same extrapolation techniques as in the previous section. $K = 2$ marks the limit of what we could empirically sample and gives little insight about the trend of this bound as K grows.

The differences between $N\langle H^1\rangle$ and $N\langle H^2\rangle$ suggest that the joint entropy of spike trains produced by multiple cells at once must be considered. As this is impossible to do by direct sampling due to computational limitations, another approach is needed. This is what we do next. Specifically, in what follows we leverage dynamical systems tools to arrive at a better understanding of global noise entropy production across the network.

4.6 From chaos to noise entropy

We begin by investigating the full network trajectories $\theta(t) = (\theta_1(t), ..., \theta_N(t))$ from (4.1), which evolve on the N-dimensional torus $\mathbb{T}^N$. Recall that a spike from cell i occurs when $\theta_i(t) = 1$, and corresponds to $S^i_l = 1$ in the appropriate time-bin. Notice that the phase response curve $Z(\theta_i)$ in (4.1) modulates the effect of I and upstream spikes on neuron θ_i, and that $Z(\theta_i)$ vanishes at $\theta_i(t) = 1$. This means that a neuron becomes insensitive to any inputs when it is about to spike. Indeed, the Taylor expansion of neuron i's dynamics about $\theta_i = 1$ is $d\theta_i = [2 + \mathcal{O}((\theta_i - 1)^2)]dt + \mathcal{O}((\theta_i - 1)^2)dW_{i,t}$.

Based on this observation — and the assumption that Δt is sufficiently small — we have the approximate conclusion that neuron i spikes in the time bin $[t, t + \Delta t]$ if and only if $\theta_i(t) \in [1 - 2\Delta t, 1)$. See Appendix B for more details about the validity of this assumption for the finite Δt we use. Now consider the partition of $\mathbb{T}^N$: $\Gamma^* = \{\gamma_0, \gamma_1\}^N$, built of cartesian products of intervals $\gamma_0 = [0, 1-2\Delta t)$ and $\gamma_1 = [1-2\Delta t, 1)$, across all θ_i's. At any time $t_l = l\Delta t$, the Γ^*-address of $\theta(t_l)$ determines the binarized spiking state of the network in time bin $[t_l, t_l + \Delta t]$: $\theta_i(t_l) \in \gamma_0 \Rightarrow S_l^i = 0$ and $\theta_i(t_l) \in \gamma_1 \Rightarrow S_l^i = 1$.

In order to describe L-long spike trains in terms of Γ^*-addresses, we must understand how solutions $\theta(t)$ evolve with respect to Γ^*. To this end, consider the discretized dynamics given by the transition maps $\Phi_{t;I}$ that send $\mathbb{T}^N$ onto itself according to the flow of (4.1) from t to $t + \Delta t$. If $\theta(t)$ is a solution of (4.1), then $\Phi_{t;I}(\theta(t)) = \theta(t + \Delta t)$ where Δt refers to the resolution of our binary spike trains S_{NL}. Note that the maps $\Phi_{t;I}$ depend on both t and I. They are expected to be smooth with smooth inverses (diffeomorphisms) [67], and together form a *random dynamical system* (RDS). For detailed geometric properties of the RDS defined by system (4.1), we refer the reader to Chapter 3.

For what follows, it is convenient to reverse time and consider spike trains and trajectories starting in the distant past and leading up to $t = 0$. This representation is statistically equivalent to one in forward time, since our networks have statistically stationary dynamics (see Chapter 3). Consider the s-step inverse map $\Phi_{0;I}^{-s}$. For any set A in the partition Γ^*, its pre-image $\Phi_{0;I}^{-s}(A)$ denotes the set of all points in $\mathbb{T}^N$ at time $-s\Delta t$ that will be mapped to A, and consequently have the same spiking state at $t = 0$. Similarly, if both A_0 and A_1 are sets in Γ^*, the intersection $\Phi_{0;I}^{-s}(A_0) \bigcap \Phi_{0;I}^{-s+1}(A_1)$ describes all points that will be mapped to A_1 at $t = -\Delta t$ and A_0 at $t = 0$. It follows that any subset of the form $B = \bigcap_{s=0}^{L} \Phi_{0;I}^{-s}(A_s)$ where $A_s \in \Gamma^*$ captures all past network states at time $t = (-L)\Delta t$ leading to the same spiking sequence $\{S_{-L}^i, ..., S_{-1}^i, S_0^i\}_{i=1,..,N}$, when the same I is presented. Moreover, it is easy to show that the collections of all possible sets constructed as B, named the *join* of pre-images of Γ^* and denoted $\vee_{s=0}^{L} \Phi_{0;I}^{-s}\Gamma^*$, is itself a partition of $\mathbb{T}^N$.

It follows that this new partition offers a one-to-one correspondence between its member sets and the space of all S_{NL} spike trains. Note that many sets in this partition are empty since not all spike sequences are accessible by the network. In fact, the number of non-empty sets remaining in $\vee_{s=0}^{L}\Phi_{0;I}^{-s}\Gamma^*$ as $L \to \infty$ represents the number of allowed infinite spike sequences. Furthermore, for a given S_{NL} and its associated set $B \in \vee_{s=0}^{L}\Phi_{0;I}^{-s}\Gamma^*$, the probability $P(S_{NL}|I)$ is equivalent to the probability of finding the network's state in B in the distant past, given that I was presented — i.e. $P(\theta \in B|I)$.

As discussed in Chapter 3, we assume that our RDS possesses an ergodic stationary probability measure μ, which is the steady state solution of the Fokker-Planck equation associated with (4.1). Thus, μ is the probability measure on $\mathbb{T}^N$ describing how likely we are to find the network in a particular state at any moment in time, given any input I drawn with the statistics of the signal distribution. As a result, selecting a random IC θ for the network amounts to drawing from μ. If we let

$$h_\mu(\Phi_{t;I}, \Gamma^*) = \lim_{n\to\infty} -\frac{1}{n} \sum_{B\in\vee_{s=0}^{n}\Phi_{0;I}^{-s}\Gamma^*} \mu(B)\ln\mu(B), \tag{4.4}$$

it follows that

$$\lim_{L\to\infty} H_{noise}^{NL} = \frac{\Delta t}{N\ln 2} h_\mu(\Phi_{t;I}, \Gamma^*). \tag{4.5}$$

For any dynamical system, expression (4.4) measures the amount of uncertainty produced by chaotic dynamics per unit time, if we can only observe the system with the precision given by the partition Γ^*. This concept is generalized by the *Kolmogorov-Sinai entropy* h_μ, also called *dynamical* or *metric* entropy [44, 109], defined by

$$h_\mu = \sup_{\Gamma} h_\mu(\Phi_{t;I}, \Gamma), \tag{4.6}$$

where the supremum is taken over all finite partitions Γ. The Kolmogorov-Sinai entropy is related to the Lyapunov spectrum $\lambda_1 \geq \lambda_2 \geq ... \geq \lambda_N$ of a dynamical system; this spectrum measures rates of exponential divergence or convergence between trajectories. Lyapunov exponents λ_i are expected to be well defined for our RDS in the sense that they depend on system parameters but not on any particular choices of input I [66] (see also Chapter 3). The authors of [73] showed that although the join of a partition Γ depends on I, h_μ does not and under some ergodicity assumptions, the following entropy formula holds:

$$h_\mu = \sum_{\lambda_i > 0} \lambda_i. \tag{4.7}$$

If λ_i are the Lyapunov exponents of the original system (4.1) computed over time units instead of Δt time-steps, we get from (4.4) , (4.5) and (4.7) the following upper bound for noise entropy rate :

$$H_{KS} \equiv \frac{1}{\ln 2} \sum_{\lambda_i > 0} \lambda_i \geq N \lim_{L \to \infty} H^{NL}_{noise}, \tag{4.8}$$

which has units of bits per time unit.

In summary, this bound relies on the assumption that spike trains are equivalent to a partition address of trajectories, constructed from linearizing the flow of the system close to spiking. While this correspondence may fail in isolated instances, we argue that H_{KS} accurately captures statistical trends of spiking dynamics, and we refer the reader to Appendix B for detailed verifications of this approximation.

To compute H_{KS}, we numerically calculate the exponents λ_i of system (4.1) (see Appendix B) and find that, as originally observed in [87] for autonomous networks, our driven system has a size-invariant Lyapunov spectrum (see Figure 4.2 (d)) which is insensitive to particular choices of the coupling matrix A. This leads to a spatially extensive behavior of the bound H_{KS} as shown in Figure 4.2 (c), a fact compatible with the assumption that noise entropy rate is extensive in system size. Importantly, we find that H_{KS} is considerably smaller than the $N\langle H^1\rangle$ and $N\langle H^2\rangle$ bound estimates. This implies that – even though spike correlations are limited and variable – there is considerably less noise entropy produced by our chaotic network than is predicted by only observing single cells or pairs of cells at a time (cf. [113]).

4.7 Mean vs fluctuation driven regimes for large nets shape the level of noise entropy production.

Now that we know the level of noise entropy in our network to be bounded above by H_{KS}, we use this quantity to investigate how response variability depends on statistical attributes of the input stimuli I — specifically the stimulus mean η and fluctuation amplitude ε. As a preliminary step, we numerically compute the mean firing rate (i.e., network-averaged spiking frequency) of (4.1) for a range of these parameter values. Figure 4.3 (a) shows the result for a network with $N = 500$. Here the black line indicates the level curve obtained by fixing the firing rate to match the benchmark parameter set used above ($\eta = -0.5$, $\varepsilon = 0.5$). We investigate network dynamics at different points along this curve.

Figure 4.3 (b) shows the first 200 Lyapunov exponents of (4.1) for a set of points along the level curve, parametrized so that η grows while ε decreases. Thus, as we travel along this curve, the dynamics gradually shift from an excitable ($\eta < 0$), fluctuation-driven regime to an oscillatory ($\eta > 0$), mean-driven one. In particular, the last point on this curve corresponds to a purely autonomous regime ($\varepsilon = 0$) where the input I has no fluctuating component and network activity is solely due to the oscillatory nature of neurons receiving a constant current as in [87]. Figure 4.3 (c) shows the corresponding H_{KS} estimates.

A clear trend emerges: the noise entropy bound H_{KS} monotonically increases as the strength of stimulus fluctuations decreases. Moreover, Figure 4.3 (d) shows that, for spikes produced in the highly oscillatory as well as the highly excitatory regime, this bound reveals that spike train noise entropy continues to be much lower for the network as a whole than predicted by extrapolating single-cell entropy. The relative values of H^1 and H_{KS} also appear to vary in similar ways as the network switches

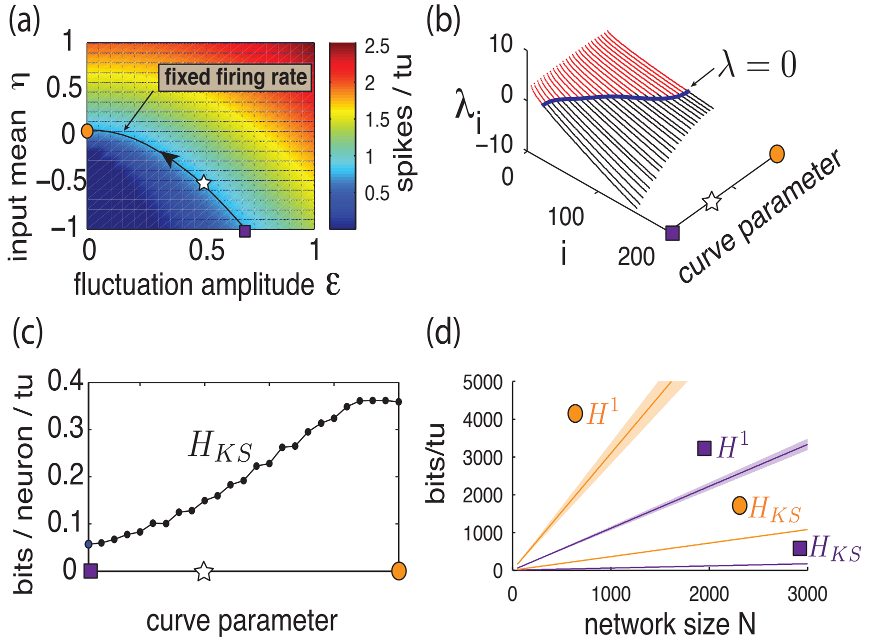

Figure 4.3: (A) Heat map of excitatory population mean firing rate for a range of input amplitude ε and input mean η. The line is the level-set curve for a fixed firing rate of 0.820 $spikes/tu \pm 0.003$ (computed via interpolation); arrow shows direction of parametrization along this curve. Square marker: $\eta = -1$, $\varepsilon = 0.69$; star: $\eta = -0.5$, $\varepsilon = 0.5$; circle: $\eta = 0.07$, $\varepsilon = 0$. (B) Lyapunov spectra along the curve from (a). (C) H_{KS} bounds evaluated along contour curve from (a). (D) Network noise entropy H^1 and H_{KS} bound extrapolations as a function of network size N, for parameter values indicated by the square and circle markers in (a). For all panels, $N = 500$.

from more excitable to more oscillatory firing. As both these values significantly differ between oscillatory and excitable regimes, this suggests that while large balanced networks are expected to be chaotic, noise entropy production strongly depends on the temporal content of the input driving them.

4.8 Discussion

Noise entropy is an indicator of the resolution with which signals can be encoded in spike patterns. Our study aims to quantify this resolution in chaotic, balanced state networks. We found that noise entropy in these networks is bounded to be significantly lower that one would estimate by extrapolating from single cells. Moreover, this entropy decreases systematically with the strength of temporal fluctuations in input signals to the networks. The extensive nature of this phenomenon suggests that this mechanism is scalable with network size (cf. [87]).

We expect that the key tool in our study, a bound based on H_{KS}, can be adapted to other neuron models. The key step is using a state space partition that links trajectories to spike patterns. Further extensions would investigate how noise entropy depends on other network attributes such as connectivity, learning rules or “spatial” structure (i.e., correlations) in network inputs.

We close by recalling that spike train noise entropy is one term in an expression for the mutual information between network inputs and the system’s response. In order to estimate this quantity, one needs to compute the *total entropy* [102] of spike patterns. This term quantifies how many distinct spike outputs can be produced by the network, for any input I. This quantity once again depends on both network connectivity and single neuron dynamics, and will be the subject of future work.

Chapter 5

CONCLUSION

5.1 Summary

Throughout this dissertation, I present various mathematical results relevant to the field of theoretical neuroscience. While the specific motivations and potential applications of these results are varied, each is centered on a common theme. This is the joint activity of non-autonomous ensembles of simple dynamical systems, representing neurons and neural networks. Specifically, I focus on the dynamics of many identical units, coupled and uncoupled, subject to external forcing.

In all cases, the characteristics of the underlying models of single neurons were well understood in isolation. My chief contributions are to expand the understanding of how they respond to inputs when arranged in large groups or networks. Analysis of such systems is highly challenging, and required a wide array of techniques from classical dynamical and stochastic systems, probability theory, as well as the modern theory of random dynamical systems. Moreover, purely analytical treatments of these high-dimensional dynamics were often limited, and a blend of analytical and large-scale numerical approaches proved most fruitful. While the development of new mathematics is undoubtedly required to treat network dynamics, I believe that similar hybrid approaches will continue to drive advances in the field in the future.

Chapter 2 deals with the synchrony and desynchrony of identical elliptic bursting neurons in response to periodic pulsatile inputs. In general, one might intuitively expect identical oscillatory systems to entrain to a common input. However in this case, a burst cycle is generated by slow/fast dynamics which create instabilities that dramatically change this outcome. Indeed, it is shown that a specific range of input frequencies and strengths lead to chaotic dynamics, which in turn generate *asynchronous*, rather than entrained, dynamics within a population. Furthermore, it is demonstrated that this mechanism is robust to moderate amounts of noise and can be generalized to cases where more than one periodic input "compete" with one another. Finally, while this result is developed for a simplified model, its validity is verified for a higher dimensional, biophysically realistic model of a neuron. A potential application to a treatment for Parkinson's disease, deep brain stimulation, is discussed.

Chapter 3 presents the analysis of large random networks of θ-neurons in the balanced state. This network model generates irregular spiking activity among neurons and generally operates in a chaotic dynamical regime. Building on existing literature, it is shown that when such networks are perturbed by rapidly fluctuating inputs, representing driving signals, chaotic dynamics persist but produce surprisingly structured spike outputs. Indeed, when the same signal is presented but the network's initial state is randomly chosen on multiple trials, a majority of evoked spikes are reliably reproduced despite inherent dynamical instabilities emerging from the chaos. Such a phenomenon is studied with a random dynamical systems framework, and is shown to be a product of low-dimensional chaotic attractors. The implications of this mechanism for neural coding in cortical networks is briefly discussed.

Chapter 4 builds on Chapter 3, and focuses on the joint variability of entire spike trains produced by stimulus-driven balanced networks. Here, the concept of variability describes the breadth of spike train distributions conditioned on an input. As above, these distributions describe the possible spike outputs one may observe if a fixed input is presented but initial network states are chosen randomly. How varied are these evoked spike responses is quantified by the entropy of these conditional distributions, often called *noise entropy.* In general, this quantity is hard to estimate directly from sample data sets when one considers more than just a few cells at the time. This is because the space of joint spike patterns grows exponentially with network size. Here, it is shown that an estimate of the noise entropy for driven networks could be obtained from the dynamical entropy production of these large systems. This quantity is related to the Lyapunov exponent spectrum and requires much less data to estimate. Furthermore, this result illustrates that the joint noise entropy of large networks can be much lower than what could be predicted by only observing and quantifying partial subsets of cells. Finally, the dependence of this entropy on input attributes is explored, and the implication for neural coding performed by such sparse networks is discussed.

5.2 Future work

This dissertation fuels a broad interest in the use of theoretical tools to approach questions related to dynamics and coding in large spiking neuronal networks. Specifically, this opens the door to further work on problems at the interface of mathematics and neuroscience. These are characterized by both simplified models that can lead to results which impact our understanding of general, high-dimensional dynamical systems, and problems directly motivated by neurophysiology. I give examples of these open questions next.

5.2.1 Theoretical study of Deep Brain Stimulation on networks of bursting neurons

While Chapter 2 deals with uncoupled bursting neurons, it is important to understand the impact of pulsatile inputs on coupled neural populations. As bursting neurons from *globus pallidus externa* (GPe) are weakly coupled to one another and recurrently coupled to neurons in the *subthalamic nucleus* (STN) (see [124] and references therein), I am interested in applying techniques developed in this dissertation to this more realistic context. Preliminary numerical results show that appropriate pulsatile inputs may be able to desynchronize networks. This research was conducted with Megan Lacy, an undergraduate researcher at the University of Washington.

Furthermore, recent findings from unpublished work of Dr. Charles Wilson (Univ. Texas San Antonio) suggest that in Parkinson's disease, neurons in GPe may not be intrinsically bursting as previously thought. Rather, bursting dynamics may be an emergent phenomenon at the network level. This raises interesting possibilities for future work where I intend to adapt the discrete dynamics framework described in Chapter 2 to a more realistic BG physiology, guided by experimental results and in a possible collaboration with Dr. Wilson.

5.2.2 Impact of network architecture and single cell properties on spike pattern variability

Using the framework developed in Chapters 3 and 4, I am interested in exploring the impact of network architecture on the spike-time reliability of temporally driven spiking networks. For example, the use of non-normal coupling matrices has been studied in the context of rate-based network models [100] but little is known about their spiking equivalent, let alone in the presence of a temporal drive. The presence of connectivity motifs is also an important source of structure which is known to impact pairwise correlations between cells in a network. I am interested in the impact of such local network architecture on the broader structure of spike train outputs. As a first step, I intend to adapt the approach developed in Chapters 3 and 4 to networks inspired from cortical regions, implementing architectures where the activity evoked by a stimulus is propagated through recurrently coupled layers.

Furthermore, I intend to study the impact of single cell dynamics on driven network variability. Preliminary results from myself, Eric Shea-Brown and Kevin K. Lin indicate that the *excitable* neurons whose intrinsic dynamics contain a resting point and a threshold behave very differently than *oscillatory* neurons, where intrinsic dynamics contain a limit cycle. A better understanding of such differences, in concert with experimental measurements of neuron dynamics, may lead to new perspectives on stimulus encoding in recurrently coupled networks.

BIBLIOGRAPHY

[1] S Asmussen and P W Glynn. *Stochastic simulation : algorithms and analysis*, volume 57 of *Stochastic modelling and applied probability.* New York: Springer, 2007.

[2] A Azad and P Ashwin. Within-burst synchrony changes for coupled elliptic bursters. *SIAM Journal on Applied Dynamical Systems*, 9:261–281, 2010.

[3] SM Baer, T Erneux, and J Rinzel. The slow passage through a hopf bifurcation: delay, memory effects, and resonance. *SIAM Journal on Applied Mathematics*, 49(1):55–71, 1989.

[4] SM Baer and E Gaekel. Slow acceleration and deacceleration through a hopf bifurcation: Power ramps, target nucleation, and elliptic bursting. *Physical Review E*, 78, 2008.

[5] A Banerjee, P Seriès, and A Pouget. Dynamical constraints on using precise spike timing to compute in recurrent cortical networks. *Neural Computation*, 20(4):974–993, 2008.

[6] Arunava Banerjee. On the sensitive dependence on initial conditions of the dynamics of networks of spiking neurons. *J. Comp. Neuro.*, 20(3):321–348, 2006.

[7] Baxendale. Statistical equilibrium and two-point motion for a stochastic flow of diffeomorphisms. *Spatial stochastic processes, Progress in Probability, Springer*, 19(4):189–218, 1991.

[8] Maxim Bazhenov, Nikolai Rulkov, Jean-Marc Fellous, and Igor Timofeev. Role of network dynamics in shaping spike timing reliability. *Physical Review E*, 72(4):041903, Oct 2005.

[9] J Bélair. Periodic pulsatile stimulation of a nonlinear oscillator. *Journal of Mathematical Biology*, 24:217–232, Jan 1986.

[10] M Di Bernardo, M Budd, C Champneys, and A.R Kowalczyk. Piecewise-smooth dynamical systems: theory and applications. *Springer*, 163:234, Jan 2008.

[11] Janet Best, Choongseok Park, David Terman, and Charles Wilson. Transitions between irregular and rhythmic firing patterns in excitatory-inhibitory neuronal networks. *J Comput Neurosci*, 23(2):217–235, Aug 2007.

[12] W Bialek, F Rieke, RR de Ruyter Van Steveninck, and D Warland. Reading a neural code. *Science*, 252(5014):1854–1857, 1991.

[13] A Boyarsky and P Gora. *Laws of chaos: invariant measures and dynamical systems in one dimension*. Birkhauser- Boston, Jan 1997.

[14] P Bressloff and J Stark. Neuronal dynamics based on discontinuous circle maps. *Physics Letters A*, 150(3,4):187–195, Oct 1990.

[15] E Brown, J Moehlis, and P Holmes. On the phase reduction and response dynamics of neural oscillator populations. *Neural Computation*, 16(4):673–715, 2004.

[16] HL Bryant and JP Segundo. Spike initiation by transmembrane current: a white-noise analysis. *Journal of Physiology*, 260:279–314, 1976.

[17] GIL Bub and L Glass. Bifurcation in a discontinuous circle map: a theory for a chaotic cardiac arrhythmia. *International Journal of Bifurcation and Chaos*, 5(2):359–371, 1995.

[18] B Burns and AC Webb. The spontaneous activity of neurones in the cat's cerebral cortex. *Proceedings of the Royal Society of London. Series B. Biological Sciences*, 194(1115):211–223, 1976.

[19] R Calin-Jageman and M Tunstall. Parameter space analysis suggests multi-site plasticity contributes to motor pattern initiation in tritonia. *J Neurophysiol*, 98:2382–2398, Jan 2007.

[20] S Coombes and S Doole. Neuronal population dynamics with post inhibitory rebound: a reduction to piecewise linear discontinuous circle maps. *Dynamics and Stability of Systems*, 11(3):193–217, 1996.

[21] Stephen Coombes and Paul C. Bressloff. Bursting: the genesis of rhythm in the nervous system. *World scientific publishing, Singapore*, page 401, Jan 2005.

[22] H Croisier, M Guevara, and P Dauby. Bifurcation analysis of a periodically forced relaxation oscillator: Differential model versus phase-resetting map. *Phys. Rev. E*, 79(016209):1–20, Jan 2009.

[23] Jane Cronin and Robert E. O'Malley. Analyzing multiscale phenomena using singular perturbation methods. *American Mathematical Society*, page 187, Jan 1999.

[24] G Cymbalyuk, Q Gaudry, M Masino, and R.L Clabrese. Bursting in leech heart interneurons: cell-autonomous and network-based mechanisms. *Journal of Neuroscience*, 15(22(24)):10580–10592, Jan 2002.

[25] P Danzl, J Hespanha, and J Moehlis. Event-based minimum-time control of oscillatory neuron models. *Biological cybernetics*, 101:387–399, Dec 2009.

[26] Alain Destexhe, Michael Rudolph, and Denis Paré. The high-conductance state of neocortical neurons in vivo. *Nat Rev Neurosci*, 4(9):739–751, Sep 2003.

[27] A Dhooge, W Govaerts, and Y Kuznetsov. Matcont: a matlab package for numerical bifurcation analysis of odes. *ACM Transactions on Mathematical Software*, 29(2):141–164, Jan 2003.

[28] F Diener and M Diener. Maximal delay. *Dynamic Bifurcations*, Jan 1991.

[29] J Ding and Z Wang. Parallel computation of invariant measures. *Annals of Operations Research*, 103:283–290, 2001.

[30] A. S. Ecker, P. Berens, A. S. Tolias, and M. Bethge. The effect of noise correlations in populations of diversely tuned neurons. *The Journal of Neuroscience*, 31(40):14272–14283, Sep 2011.

[31] J. P. Eckmann and D. Ruelle. Ergodic theory of chaos and strange attractors. *Rev. Mod. Phys.*, 57:617–656, Jul 1985.

[32] M Eigen, W Gardiner, P Schuster, and R Winkleroswatitsch. The origin of genetic information. *Scientific american*, 244(4), 1981.

[33] B Ermentrout. Type i membranes, phase resetting curves, and synchrony. *Neural Computation*, 8(5):979–1001, 1996.

[34] B Ermentrout and D Terman. *Mathematical foundations of neuroscience*, volume 35. Springer, Interdisciplinary applied mathematics, 2010.

[35] GB Ermentrout and N Kopell. Frequency plateaus in a chain of weakly coupled oscillators, i. *SIAM J. Math. Anal.*, 15:215–237, 1984.

[36] Xiao-Jiang Feng, Brian Greenwald, Herschel Rabitz, Eric Shea-Brown, and Robert Kosut. Toward closed-loop optimization of deep brain stimulation for parkinson's disease: concepts and lessons from a computational model. *J. Neural Eng.*, 4(2):L14–L21, Feb 2007.

[37] Xiao-Jiang Feng, Eric Shea-Brown, Brian Greenwald, Robert Kosut, and Herschel Rabitz. Optimal deep brain stimulation of the subthalamic nucleus—a computational study. *J Comput Neurosci*, 23(3):265–282, Oct 2007.

[38] M Filion, L Tremblay, and P J Bédard. Abnormal influences of passive limb movement on the activity of globus pallidus neurons in parkinsonian monkeys. *Brain Res*, 444(1):165–76, Mar 1988.

[39] Crispin W Gardiner. *Handbook of stochastic methods : for physics, chemistry and the natural sciences.* Springer series in synergetics, 2002.

[40] K Geist, U Parlitz, and W Lauterborn. Comparison of different methods for computing lyapunov exponents. *Prog. Theor. Phys*, 83(5):875–893, 1990.

[41] L Glass and J Bélair. Universality and self-similarity in the bifurcations of circle maps. *Physica D*, 16:143–154, 1985.

[42] L Glass, MR Guevara, A Shrier, and R Perez. Bifurcation and chaos in a periodically stimulated cardiac oscillator. *Physica D: Nonlinear Phenomena*, 7(1-3):89–101, 1983.

[43] M Golubitsky, K Josic, and E Shea-Brown. Winding numbers and average frequencies in phase oscillator networks. *Journal of Nonlinear Science*, 16(3):201–231, Jun 2006.

[44] A Greven, G Keller, and G Warnecke. *Entropy.* PrincetonUniversity Press, 2003.

[45] B Grothe, M Pecka, and D McAlpine. Mechanisms of sound localization in mammals. *Physiological Reviews*, Jan 2010.

[46] J Guckenheimer. Isochrons and phaseless sets. *J. Math. Biol.*, 1:259–273, 1975.

[47] Philip J Hahn, Gary S Russo, Taka Hashimoto, Svjetlana Miocinovic, Weidong Xu, Cameron C McIntyre, and Jerrold L Vitek. Pallidal burst activity during therapeutic deep brain stimulation. *Exp Neurol*, 211(1):243–51, May 2008.

[48] T Hashimoto, C Elder, M Okun, and S Patrick. Stimulation of the subthalamic nucleus changes the firing pattern of pallidal neurons. *Journal of Neuroscience*, Jan 2003.

[49] C Hauptmann and P Tass. Cumulative and after-effects of short and weak coordinated reset stimulation: a modeling study. *J. Neural Eng.*, 6(016004):1–13, Jan 2009.

[50] Christian Hauptmann, Oleksandr Popovych, and Peter A Tass. Desynchronizing the abnormally synchronized neural activity in the subthalamic nucleus: a modeling study. *Expert review of medical devices*, 4(5):633–50, Sep 2007.

[51] AV Herz and JJ Hopfield. Earthquake cycles and neural reverberations: collective oscillations in systems with pulse-coupled threshold elements. *Phys. Rev. Lett.*, 75:1222–1225, 1995.

[52] A Hodgkin and A Huxley. . . . Measurement of current-voltage relations in the membrane of the giant axon of loligo. *The Journal of physiology*, Jan 1952.

[53] S Hogan, L Higham, and T Griffin. Dynamics of a piecewise linear map with a gap. *Proceedings of the Royal Society A*, 463:49–65, 2007.

[54] J Hunter, J Milton, P Thomas, and J Cowan. Resonance effect for neural spike time reliability. *J. Neurophysiol.*, 80:1427–1438, 1998.

[55] E Izhikevich. Neural excitability, spiking and bursting. *International Journal of Bifurcation and Chaos*, 10(6):1171–1266, 2000.

[56] E Izhikevich. Phase equations for relaxation oscillators. *SIAM Journal on Applied Mathematics*, 60(5):1789–1804, May 2000.

[57] E Izhikevich. Subcritical elliptic bursting of bautin type. *SIAM Journal on Applied Mathematics*, 60(2):503–535, Feb 2000.

[58] E Izhikevich. Synchronization of elliptic bursters. *SIAM Review*, 43(2):315–344, Jun 2001.

[59] EM Izhikevich. Dynamical systems in neuroscience. *MIT Press, Cambridge, MA*, page 505, 2007.

[60] P Jain and S Banerjee. Border collision bifurcations in one-dimensional discontinuous maps. *International Journal of Bifurcation and Chaos*, 13(11):3341–3352, 2003.

[61] M Johnson, J Vitek, and C Mcintyre. Pallidal stimulation that improves parkinsonian motor symptoms also modulates neuronal firing patterns in primary motor cortex in the mptp-treated monkey. *Exp Neurol*, May 2009.

[62] C KRT Jones and Alexander I Khibnik. Multiple time scale dynamical systems (the ima volumes in mathematics and its applications). *Springer*, 122, 2000.

[63] P Kara, P Reinagel, and R.C Reid. Low response variability in simultaneously recorded retinal, thalamic, and cortical neurons. *Neuron*, 27(3):635–646, 2000.

[64] A Katok and B Hasselblatt. Introduction to the modern theory of dynamical systems. *Cambridge University Press*, Jan 1995.

[65] J Keener. Chaotic behavior in piecewise continuous difference equations. *Transactions of the American Mathematical Society*, 261(2):589–604, Oct 1980.

[66] Yu Kifer. *Ergodic Theory of Random Transformations.* 1986.

[67] H Kunita. *Stochastic Flows and Stochastic Differential Equations*, volume 24. 1990.

[68] R Kuske. Probability densities for noisy delay bifurcations. *Journal of Statistical Physics*, 96(3/4):797–816, 1999.

[69] R Kuske and SM Baer. Asymptotic analysis of noise sensitivity in a neuronal burster. *Bulletin of mathematical biology*, 64:447–481, 2002.

[70] G Lajoie and E Shea-Brown. Shared inputs, entrainment, and desynchrony in elliptic bursters: From slow passage to discontinuous circle maps. *SIAM Journal on Applied Dynamical Systems*, 10:1232, 2011.

[71] Guillaume Lajoie, Kevin K Lin, and Eric Shea-Brown. Chaos and reliability in balanced spiking networks with temporal drive. *Phys. Rev. E*, 87(5):052901, May 2013.

[72] P E Latham, B J Richmond, P G Nelson, and S Nirenberg. Intrinsic dynamics in neuronal networks. i. theory. *J. Neurophysiol.*, 83:808–827, 2000.

[73] F Ledrappier and L-S Young. Entropy formula for random transformations. *Probab. Th. and Rel. Fields*, 80:217–240, 1988.

[74] Y LeJan. Équilibre statistique pour les produits de difféomorphismes aléatoires indépendants. *Ann. Inst. Henri Poincaré*, 23(1):11–120, 1987.

[75] K Lin, E Shea-Brown, and L-S Young. Reliability of coupled oscillators. *J. Nonlin. Sci.*, 19(5):497–545, 2009.

[76] Kevin K Lin, Eric Shea-Brown, and Lai-Sang Young. Spike-time reliability of layered neural oscillator networks. *J Comput. Neuro.*, 27(1):135–160, Aug 2009.

[77] B Lindner, A Longtin, and A Bulsara. Analytic expressions for rate and cv of a type i neuron driven by white gaussian noise. *Neural Comput.*, 15(8):1761–1788, 2003.

[78] Ashok Litwin-Kumar, Anne-Marie M Oswald, Nathaniel N Urban, and Brent Doiron. Balanced synaptic input shapes the correlation between neural spike trains. *PLoS Comput. Biol.*, 7(12):e1002305, 2011.

[79] Michael London, Arnd Roth, Lisa Beeren, Michael Häusser, and Peter E Latham. Sensitivity to perturbations in vivo implies high noise and suggests rate coding in cortex. *Nature*, 466(7302):123–127, Jul 2010.

[80] Z Mainen and T Sejnowski. Reliability of spike timing in neocortical neurons. *Science*, 268:1503–1506, 1995.

[81] Z.F Mainen and T.J Sejnowski. Reliability of spike timing in neocortical neurons. *Science*, 268(5216):1503–1506, 1995.

[82] N Mallet, A Pogosyan, L. F Marton, J. P Bolam, P Brown, and P. J Magill. Parkinsonian beta oscillations in the external globus pallidus and their relationship with subthalamic nucleus activity. *Journal of Neuroscience*, 28(52):14245–14258, Dec 2008.

[83] C Mcintyre, C Butson, and J Hall. Brain stimulation models, systems, devices, and methods. *US Patent App. 12/008,760*, Jan 2008.

[84] Cameron C McIntyre, Marc Savasta, Benjamin L Walter, and Jerrold L Vitek. How does deep brain stimulation work? present understanding and future questions. *Journal of clinical neurophysiology : official publication of the American Electroencephalographic Society*, 21(1):40–50, Jan 2004.

[85] GS Medvedev and N Kopell. Synchronization and transient dynamics in the chains of electrically coupled fitzhugh-nagumo oscillators. *SIAM Journal on Applied Mathematics*, 61(5):1762–1801, 2001.

[86] L. Molgedey, J. Schuchhardt, and H. G. Schuster. Suppressing chaos in neural networks by noise. *Phys. Rev. Lett.*, 69:3717–3719, 1992.

[87] Michael Monteforte and Fred Wolf. Dynamical entropy production in spiking neuron networks in the balanced state. *Phys. Rev. Lett.*, 105(26):268104, Dec 2010.

[88] Hiroya Nakao, Ken-Suke Arai, Ken Nagai, and Yoshiki Kuramoto. Synchrony of limit-cycle oscillators induced by random external impulses. *Phys. Rev. E*, 72(2):1–13, Aug 2005.

[89] A Namenson, E Ott, and TM Antonsen. Fractal dimension fluctuations for snapshot attractors of random maps. *Phy. Rev. E*, 53(3):2287–2291, 1996.

[90] H Noda and W.R Adey. Firing variability in cat association cortex during sleep and wakefulness. *Brain Res.*, 18(3):513–526, 1970.

[91] K Pakdaman and D Mestivier. External noise synchronizes forced oscillators. *Physical Review E*, Jan 2001.

[92] L Paninski. Maximum likelihood estimation of cascade point-process neural encoding models. *Network: Computation in Neural Systems*, Dec 2004.

[93] L Paninski, J Pillow, and J Lewi. Statistical models for neural encoding, decoding, and optimal stimulus design. *Progress in brain research*, 165:493, 2007.

[94] A Parent and L N Hazrati. Functional anatomy of the basal ganglia. ii. the place of subthalamic nucleus and external pallidum in basal ganglia circuitry. *Brain Res Brain Res Rev*, 20(1):128–54, Jan 1995.

[95] M Perc and M Marhl. Chaos in temporarily destabilized regular systems with the slow passage effect. *Chaos, Solitons and Fractals*, 27:395–403, 2006.

[96] A Pikovsky, M Rosenblum, and J Kurths. *Synchronization: A Universal Concept in Nonlinear Sciences.* 2001.

[97] JW Pillow, L Paninski, VJ Uzzell, EP Simoncelli, and EJ Chichilnisky. Prediction and decoding of retinal ganglion cell responses with a probabilistic spiking model. *Journal of Neuroscience*, 25(47):11003–11013, 2005.

[98] Marco Pirini, Laura Rocchi, Mariachiara Sensi, and Lorenzo Chiari. A computational modelling approach to investigate different targets in deep brain stimulation for parkinson's disease. *J Comput Neurosci*, 26(1):91–107, Feb 2009.

[99] K Rajan, L Abbott, H Sompolinsky, and D Proment. Stimulus-dependent suppression of chaos in recurrent neural networks. *Physical Review E*, Dec 2010.

[100] Kanaka Rajan and L Abbott. Eigenvalue spectra of random matrices for neural networks. *Phys. Rev. Lett.*, 97(18):188104, Nov 2006.

[101] P Reinagel and R.C Reid. Temporal coding of visual information in the thalamus. *Journal of Neuroscience*, 20(14):5392–5400, Jul 2000.

[102] F Rieke, D Warland, R de Ruyter van Steveninck, and W Bialek. *Spikes: Exploring the Neural Code*. 1996.

[103] J Rinzel and G Ermentrout. Analysis of neural excitability and oscillations. *From "Methods in Neuronal Modelling: From synapses to Networks", MIT Press*, pages 135–169, Jan 1989.

[104] J Rinzel and Y Lee. Dissection of a model for neuronal parabolic bursting. *Journal of Mathematical Biology*, 25:653–675, Jan 1987.

[105] J Rinzel and W Troy. Bursting phenomena in a simplified oregonator flow system model. *The Journal of Chemical Physics*, 76(4):1775–1789, Jan 1982.

[106] John Rinzel. A formal classification of bursting mechanisms in excitable systems. pages 1578–1593, 1987.

[107] Jason Ritt. Evaluation of entrainment of a nonlinear neural oscillator to white noise. *Phys. Rev. E*, 68(4):1–7, Oct 2003.

[108] JE Rubin and D Terman. High frequency stimulation of the subthalamic nucleus eliminates pathological thalamic rhythmicity in a computational model. *J Comput Neurosci*, 16(3):211–235, 2004.

[109] D Ruelle. *Chaotic Evolution and Strange Attractors*. Cambridge University Press, 1989.

[110] N Rulkov, M Sushchik, L Tsimring, and H Abarbanel. Generalized synchronization of chaos in directionally coupled chaotic systems. *Physical Review E*, 51(2):980–994, Jan 1995.

[111] S Santaniello, G Fiengo, L Glielmo, and W.M Grill. Closed-loop control of deep brain stimulation: A simulation study. *Neural Systems and Rehabilitation Engineering, IEEE Transactions on*, (99):1–1, 2011.

[112] T Schlaepfer, M Cohen, C Frick, and M Kosel.... Deep brain stimulation to reward circuitry alleviates anhedonia in refractory major depression. *Neuropsychopharmacology*, 33:368–377, Jan 2008.

[113] Elad Schneidman, Michael J Berry, Ronen Segev, and William Bialek. Weak pairwise correlations imply strongly correlated network states in a neural population. *Nature*, 440(7087):1007–1012, Apr 2006.

[114] M N Shadlen and W T Newsome. The variable discharge of cortical neurons: implications for connectivity, computation, and information coding. *J. Neurosci.*, 18:3870–3896, 1998.

[115] Andrey Shilnikov, Rene Gordon, and Igor Belykh. Polyrhythmic synchronization in bursting networking motifs. *Chaos: An Interdisciplinary Journal of Nonlinear Science*, 18(3):037120, 2008.

[116] Y Shu, A Hasenstaub, and D.A McCormick. Turning on and off recurrent balanced cortical activity. *Nature*, 423(6937):288–293, 2003.

[117] S Strogatz. Nonlinear dynamics and chaos: With applications to physics, biology, chemistry, and engineering. *Perseus books- Cambridge*, Jan 1994.

[118] SP Strong, R Koberle, RR de Ruyter Van Steveninck, and W Bialek. Entropy and information in neural spike trains. *Phys. Rev. Lett.*, 80(1):197–200, 1998.

[119] S.P Strong, R Koberle, R.R de Ruyter van Steveninck, and W Bialek. Entropy and information in neural spike trains. *Physical Review Letters*, 80(1):197–200, 1998.

[120] J Su, J Rubin, and D Terman. Effects of noise on elliptic bursters. *Nonlinearity*, 17:133–157, Jan 2004.

[121] Peter A Tass. Desynchronization of brain rhythms with soft phase-resetting techniques. *Biological Cybernetics*, 87(2):102–115, Aug 2002.

[122] D Terman. Geometric singular perturbation analysis of neuronal dynamics. *Methods and models in neurophysics, Elsevier*, 3:73–121, Jan 2005.

[123] D Terman, S Ahn, X Wang, and W Just. Reducing neuronal networks to discrete dynamics. *Physica D: Nonlinear Phenomena*, 237(3):324–338, 2008.

[124] D Terman, JE Rubin, AC Yew, and CJ Wilson. Activity patterns in a model for the subthalamopallidal network of the basal ganglia. *Journal of Neuroscience*, 22(7):2963, 2002.

[125] Paul Tiesinga, Jean-Marc Fellous, and Terrence J Sejnowski. Regulation of spike timing in visual cortical circuits. *Nat Rev Neurosci*, 9(2):97–107, 2008.

[126] G Tkačik, JS Prentice, V Balasubramanian, and E Schneidman. Optimal population coding by noisy spiking neurons. *Proceedings of the National Academy of Sciences*, 107(32):14419, 2010.

[127] G.J Tomko and D.R Crapper. Neuronal variability: non-stationary responses to identical visual stimuli. *Brain Res.*, 79(3):405–418, 1974.

[128] A Uchida, R McAllister, and R Roy. Consistency of nonlinear system response to complex drive signals. *Physical review letters*, 93, 2004.

[129] C van Vreeswijk and H Sompolinsky. Chaos in neuronal networks with balanced excitatory and inhibitory activity. *Science*, 274:1724–1726, 1996.

[130] C van Vreeswijk and H Sompolinsky. Chaotic balanced state in a model of cortical circuits. *Neural Comput.*, 1998.

[131] Stephen Wiggins. *Introduction to applied nonlinear dynamical systems and chaos*. Springer, Jan 2003.

[132] Charles J Wilson, Bryce Beverlin, and Theoden Netoff. Chaotic desynchronization as the therapeutic mechanism of deep brain stimulation. *Front. Syst. Neurosci.*, 5:1–11, Jan 2011.

[133] A Winfree. *The geometry of biological time, 2nd edition*. Springer-Verlag, Jan 2001.

[134] Y Yang, M DeWeese, G Otazu, and A Zador. Millisecond-scale differences in neural activity in auditory cortex can drive decisions. *Nature neuroscience*, Jan 2008.

[135] L Young. What are srb measures, and which dynamical systems have them? *Journal of Statistical Physics*, 108(5/6), Sep 2002.

[136] J Zylberberg and E Shea-Brown. Input nonlinearities shape beyond-pairwise correlations and improve information transmission by neural populations. *arXiv preprint arXiv:1212.3549*, Jan 2012.

Appendix A

CHAPTER 3 SUPPLEMENTAL MATERIAL

A.1 Model and coordinate transformations from QIF

We study the dynamics of a temporally driven network of θ-neurons where a neuron's membrane potential is represented by a phase variable on the unit circle S^1. This model has the advantage of being one of the simplest to capture the nonlinear spike generating mechanisms of Type I neurons with solutions that remain smooth in state space. Moreover, the θ-neuron is equivalent, after a smooth change of coordinates, to the dynamics of the quadratic-integrate-and-fire (QIF) model [72, 33] which uses meaningful physical units. We now review this change of coordinates and equivalences between the two models.

The variable v represents the membrane potential of a single neuron and its dynamics are described by the following equation:

$$\tau \frac{dv}{dt} = \frac{(v - v_R)(v - v_T)}{\Delta v} + I_a + I_d(t) \tag{A.1}$$

where τ is the cell membrane time constant, v_R and v_T are rest and threshold voltages respectively and $\Delta v = v_T - v_R$ is the gap between reset and threshold. I_a is an applied constant current, and $I_d(t)$ is a time varying input drive. If $v(t)$ crosses the threshold v_T, its trajectory quickly blows up to infinity where it is said to fire a spike. The voltage $v(t)$ is then reset to its resting point v_r. In absence of other inputs ($I_d = 0$), the baseline current

$$I_a = I^* = \frac{(v_T - v_R)^2}{4\Delta v} = \frac{\Delta v}{4}$$

places the system at a saddle node bifurcation, responsible for the onset of tonic (periodic) firing. Therefore, if $I_a < I^*$, the neuron is said to be in *excitable regime* whereas if $I_a > I^*$, it is in *oscillatory regime*.

Let us suppose that the input term $I_d(t)$ is a realization of a white noise process scaled by a constant ρ. We can rewrite (A.1) as a stochastic differential equation (SDE)

$$\tau dv = \left(\frac{(v - v_R)(v - v_T)}{\Delta v} + I_a \right) dt + \rho dW_t \tag{A.2}$$

where W_t is a standard Wiener process. We treat (A.2) as an SDE of the Itô type [77] as it is more convenient for numerical simulations and carry out the change of variables accordingly.

Let us introduce a new variable θ defined by

$$v(\theta) = \frac{v_T + v_R}{2} + \frac{\Delta v}{2} \tan((2\pi\theta - \pi)/2) \tag{A.3}$$

along with a rescaling of time

$$t \mapsto \frac{t}{4\pi\tau}. \tag{A.4}$$

Equation (A.2) now reads

$$d\theta = \left[F(\theta) + \eta Z(\theta) + \frac{\varepsilon^2}{2} Z(\theta) Z'(\theta) \right] dt + \varepsilon Z(\theta) dW_t \tag{A.5}$$

where $F(\theta) = 1 + \cos(2\pi\theta)$, $Z(\theta) = 1 - \cos(2\pi\theta)$ and

$$\eta = \frac{4}{\Delta v} I_a - 1$$

$$\varepsilon = \frac{2\rho}{\Delta v \sqrt{\tau\pi}}$$

which is the θ-model on $[0, 1]$ we want. In absence of stochastic drive and for $\eta < 0$, the two fixed points are given by

$$\theta^{s,u} = \frac{1}{2\pi} \arccos(\frac{\eta+1}{\eta-1})$$

which for $\eta = -1$ yields $\theta^s = 1/4$ and $\theta^u = 3/4$. For $\eta > 0$, the neuron fires periodically at a frequency of $\sqrt{\eta}/2$.

Typical parameter choices for the QIF model are

$$\begin{aligned} \tau &= 10ms \\ v_R &= -65mV \\ v_T &= -50mV \end{aligned} \tag{A.6}$$

with time in units of milliseconds. Expression (A.4) implies that one time unit in θ-coordinates corresponds to about 125 milliseconds. In the absence of applied current I_a, we get $\eta = -1$.

A.1.1 Network architecture and synaptic coupling

In the main manuscript, we explore the dynamics of Erdös-Renyi type random networks of $N = 1000$ cells of which 80% are excitatory and 20% inhibitory. Each cell receives on average $K = 20$ synaptic connections from each excitatory and inhibitory subpopulation. We implement a classical balanced state architecture and scale synaptic weights of these connections by $1/\sqrt{K}$ which ensures that fluctuations from network interactions remain independent of K in the large N limit [130] (as long as $K << N$ and cells fire close to independently). Although we do not systematically explore the scaling effects of N and K, preliminary results for combinations of $K =$ 50, 100, 200 and N =2500, 5000 indicate that our findings are qualitatively robust to system size.

As mentioned earlier, one of the advantages of the θ-neuron model is the continuity of dynamics in phase space. We can therefore easily implement synaptic interaction between two neurons with differentiable and bounded terms. Synaptic interactions between θ-neurons are modeled using a smooth function

$$g(\theta) = \begin{cases} d\left(b^2 - \left[\left(\theta + \frac{1}{2}\right) \bmod 1 - \frac{1}{2}\right]^2\right)^3 & ; \theta \in [-b, b] \\ 0 & ; \text{else} \end{cases} \tag{A.7}$$

where $b = \frac{1}{20}$ and $d = \frac{35}{32}$.

For example, for two cells coupled as $2 \to 1$, we have

$$\dot{\theta}_1 = F(\theta_1) + Z(\theta_1)\left(\eta + a_{12} g(\theta_2)\right) \tag{A.8}$$

in which a_{12} is the synaptic strength from neuron 2 to neuron 1. Neuron 2 only affects θ_1 when $\theta_2 \in [-b, b]$, mimicking a rapid rise and fall of a synaptic variable in response to presynaptic potential fluctuation during spike generation. We follow the approach of Latham et al. [72] to assess the effective coupling strength from neuron θ_2 to neuron θ_1 in the form of evoked post synaptic potentials (PSP). Specifically, we first derive a relationship between the value of a_{12} and the evoked PSP following a presynaptic spike from θ_2 in the θ coordinates. We then translate this to the voltage coordinates.

We assume that $\eta = -1$ (equiv. to $I_a = 0$), and that θ_1 sits at rest $\theta_R = \frac{1}{4}$, and compute the value $\theta_S = \theta_R + \theta_{PSP}$. As the support of g is quite small, let us linearize (A.8) for θ_2 when it crosses $0 \sim 1$. We obtain neuron 2's phase velocity at spike time, $\dot{\theta}_2 = 2$, and hold this velocity constant in the calculation that follows. Suppose that at $t = 0$, θ_2 is at the left end of g's support, then

$$\theta_2(t) = 2t - b$$

which gives us the non-autonomous equation for θ_1

$$\dot{\theta}_1 = F(\theta_1) + Z(\theta_1)[-1 + a_{12} g(2t - b)] \quad , \quad \theta_1(0) = \theta_R = 1/4. \tag{A.9}$$

We make a final assumption for small PSPs and assume that the behavior of (A.9) is linear about the resting phase ($\theta_1 = \theta_R$). This yields $\dot{\theta}_1 = a_{12} g(2t - \beta)$ which in turn gives us

$$\int_{\theta_R}^{\theta_S} d\theta_1 = a_{12} \int_0^{t=\beta} g(2t - \beta) dt$$

Notice that $\int_{-b}^{b} g(\theta) d\theta = 1$, which gives the relationship

$$a_{12} = 2(\theta_S - \theta_R).$$

Although we have made fairly strong assumptions about the θ-dynamics in deriving this expression, we tested it numerically and found that predictions of post synaptic θ variations were accurate up to the third significant digit, for the range of PSPs of interest. Using (A.3), we get the equivalent expression:

$$v_{PSP} = \frac{v_T + v_R}{2} + \frac{\Delta v}{2} \tan((\pi a_{12} - \pi)/2).$$

For $K = 20$ and $a_{ij} = 1/\sqrt{K}$, we get the following approximations for excitatory and inhibitory PSPs: $v_{EPSP} \simeq 4.0mV$ and $v_{IPSP} \simeq -8.4mV$.

Finally, we note that all synaptic couplings, when present between two cells, are of the same strength throughout the network (only the sign changes to distinguish between excitatory and inhibitory connections). Additionally, while both η and ε are network-wide constants, we introduce $\mathcal{O}(10^{-2})$ perturbations randomly chosen for each cell in order to avoid symmetries in the system.

A.2 Lyapunov spectrum approximation

In the main manuscript, we present approximations of the Lyapunov spectrum $\lambda_1 \geq \lambda_2 \geq ... \geq \lambda_N$ and related quantities for the network described by (3.1). Under very general conditions, the λ_i are well defined for system (3.1) and that they do not depend on the choice of IC or $\zeta(t)$. However, the Lyapunov exponents generally cannot be computed analytically and we therefore use Monte-Carlo simulations to approximate them. We numerically simulate system (3.1) using a Euler-Maruyama scheme with time steps of 0.005. At each point in time, we simultaneously solve the corresponding variational equation

$$\dot{S} = J(t)S \tag{A.10}$$

where $J(t)$ is the Jacobian of the flow evaluated along the simulated trajectory and $S(0)$ is the $N \times N$ identity matrix. The solution matrix $S(t)$ is then orthogonalized at each time step in order to extract the exponential growth rates associated with each Lyapunov subspace. See [40] for details of this standard algorithm.

All reported values of λ_i have a standard error less than 0.002, estimated by the method of batched means [1] (batch size = 500 time units) and cross-checked using several realizations of white noise processes and random connectivity matrices. We have also verified, by spot checks, that varying the batch window size does not affect the error estimate significantly.

Numerical simulations were implemented in Python and Cython programming languages and carried out on NSF's XSEDE supercomputing platform.

A.3 Spike triggered flow decomposition

We take a closer look at the single-cell flow in an attempt to better understand the origin of reliable and unreliable spikes. We concentrate on the effect of inputs on the

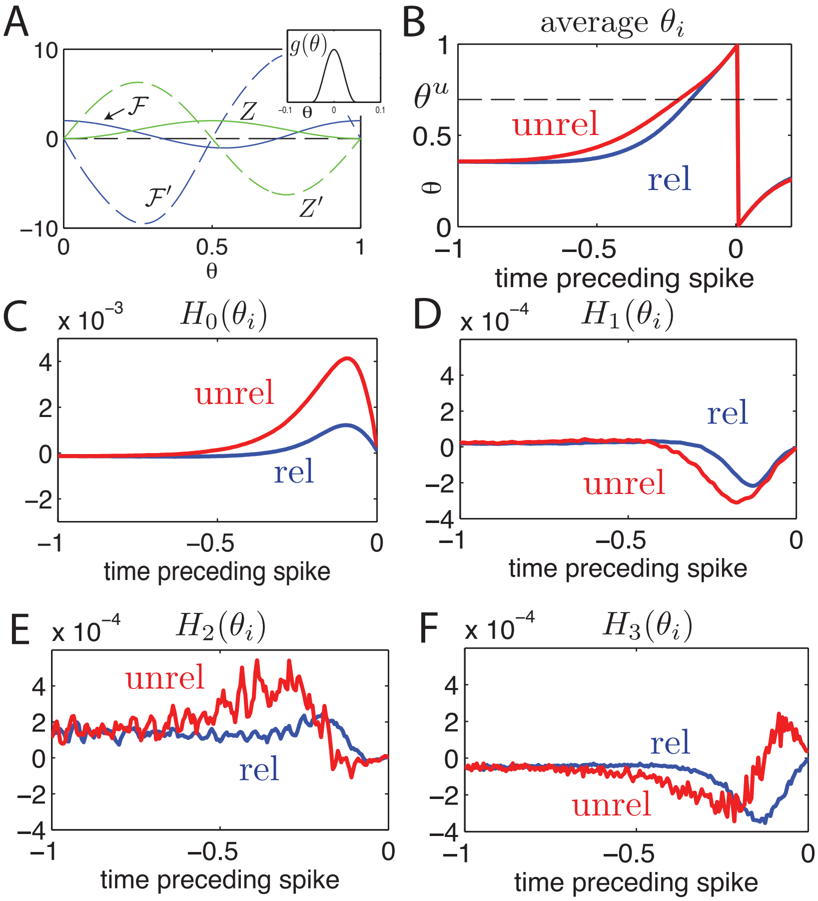

Figure A.1: (A) Distinct terms of the single cell flow and Jacobian. Inset : synaptic coupling function. For panels (B-F), $t = 0$ marks the spike time and rel/unrel indicate the identity of the spike used in the average. (B) Spike triggered average phase θ_i (same as in Fig 3.5 E). (C-F) Spike triggered average terms $H_0(\theta_i)$, $H_1(\theta_i)$, $H_2(\theta_i)$ and $H_3(\theta_i)$. Network parameters: $\eta = -0.5$, $\varepsilon = 0.5$, yielding $\lambda_1 \simeq 2.5$.

local expansion coefficient $e_i(t)$ (see Eqn. (3.6)). Consider the time evolution of $v_i(t)$ by unpacking the i^{th} component of the discretized version of (3.5):

$$\begin{aligned} v_i(t+\Delta t) = v_i(t) + v_i(t)[\Delta t \mathcal{F}(\theta_i) + \Delta t Z'(\theta_i)\sum_j a_{ij} g(\theta_j) \\ + \sqrt{\Delta t}\xi_t \varepsilon Z'(\theta_i)] + \Delta t Z(\theta_i)\sum_j a_{ij} g'(\theta_j) v_j(t) \end{aligned} \tag{A.11}$$

where $\mathcal{F}(\theta_i) = F(\theta_i) + \eta Z(\theta_i) + \frac{\varepsilon^2}{2} Z(\theta_i)Z'(\theta_i)$ and $\xi_t \sim N(0,1)$; Δt is the time increment.

We substitute expression (A.11) as the numerator in the definition of $e_i(t)$ (Eqn. (3.6)), in order to discern the contribution of different terms in the network dynamics to state space expansion. Let us define the following terms

$$\begin{aligned} H_0(t) =& \Delta t |v_i(t)| \mathcal{F}'(\theta_i) \\ H_1(t) =& \Delta t |v_i(t)| Z'(\theta_i(t)) \sum_j a_{ij} g(\theta_j(t)) \\ H_2(t) =& \Delta t Z(\theta_i(t)) \sum_j a_{ij} g'(\theta_j(t)) |v_j(t)| sgn[v_i(t) v_j(t)] \\ H_3(t) =& \sqrt{\Delta t} |v_i(t)| \varepsilon Z'(\theta_i(t)) \xi_t. \end{aligned} \tag{A.12}$$

Notice the use of the absolute value for $v(t)$ components which ensures that $H_k(t) > 0$ implies expansion (or, if $H_k(t) < 0$, contraction) in whichever of the positive and negative directions $v_i(t)$ is pointing.

Here, H_0 captures the contribution of the single-cell vector field to the proportional growth (or decay) of $v_i(t)$. Note from Fig A.1 (A) that $\mathcal{F}'(\theta_i)$, the main contributing part of H_0, is negative for $\theta_i \in (0, 1/2)$ and positive for $\theta_i \in (1/2, 1)$. Meanwhile, H_1 measures the contribution of synaptic inputs and $H_2(t)$ the relative contribution of presynaptic neurons' coordinates. The latter varies quite rapidly, because the derivative of the coupling function $g(\theta_j)$ (shown in Fig A.1 (A)) takes large positive and negative values. In essence, it quantifies the transfer of expansion from one cell to the next: if $|v_j(t)|$ is large, and $sgn[v_i(t)v_j(t)] = 1$, then H_2 causes expansion in the $v_i(t)$. Finally, H_3 captures the contribution of the external drive.

We now assess the relative importance of all of these dynamical effects to spike time reliability. We do this by comparing the magnitude and sign of the H terms. Specifically, we compute spike-triggered averages of these terms in periods before reliable and unreliable spike events. We continue to use the criterion from Chapter 3 that a spike is considered reliable if it occurs on each of the simulated trials.

Notice first that inputs – synaptic or external – enter multiplicatively with $Z'(\theta_i)$, which is negative in $\theta \in (\frac{1}{2}, 1)$ (see Fig A.1). This implies that more-excitatory synaptic inputs – or more-positive external inputs – arriving shortly before spikes promote contraction for H_1 and H_3. We see that both of these terms are primarily negative in the time periods before spikes (Panels (D),(F)), as positive inputs push cells across the spiking threshold.

Expansion – especially for unreliable events – arises from the coupling term H_2 and from the term H_0 representing internal dynamics. Note in particular that this latter term is an order of magnitude higher than the others; thus, we focus our attention on this next. Panel (B) of Fig A.1 shows that the speed at which phases cross the threshold is lower for unreliable spikes than for reliable ones. This further explains why the H_0 averages –mainly depending on $\mathcal{F}'$– are larger for the unreliable spikes.

Thus, we conclude – as noted in Chapter 3 – that the primary dynamical mechanism behind the unstable dynamics is that inputs steer $\theta_i(t)$ in expansive regions of its own subspace (see Fig A.1 (C) or Fig 3.5 (E)). This conclusion that instabilities in the flow are mainly generated by intrinsic dynamics is interesting, as it suggests that network stability could vary in rich ways depending on cell type and spike generation mechanisms.

Appendix B

CHAPTER 4 SUPPLEMENTAL MATERIAL

B.1 Numerical simulations and estimates

B.1.1 Simulations

Throughout Chapter 4, we use data from numerical simulations of the network model described by

$$d\theta_i = [F(\theta_i) + Z(\theta_i)\sum_{j=1}^{N} a_{ij}g(\theta_j) + \frac{\varepsilon^2}{2}Z(\theta_i)Z'(\theta_i)]dt + Z(\theta_i)\underbrace{[\eta dt + \varepsilon dW_i]}_{I_i(t)} \tag{B.1}$$

where $F(\theta_i) = 1 + \cos(2\pi\theta_i)$, $Z(\theta_i) = 1 - \cos(2\pi\theta_i)$ and the coupling function $g(\theta_i)$ is given by

$$g(\theta_i) = \begin{cases} d\left(b^2 - \left[\left(\theta_i + \frac{1}{2}\right) \bmod 1 - \frac{1}{2}\right]^2\right)^3 & ;\ \theta_i \in [-b, b] \\ 0 & ;\ \text{else} \end{cases}$$

with $b = 1/20$ and $d = 35/32$.

All simulations of (B.1) were implemented using a standard Euleur-Maruyama solver with time-steps of 0.005 time-units. We found that using smaller time-steps did not alter our results. The solver was developed using the Python/Cython programming language using the Mersenne Twister random number generator and post-processing (spike binning and empirical noise entropy estimates) was carried out in MATLAB. Large simulations were performed on the NFS XSEDE *Science Gateways* supercomputing platform.

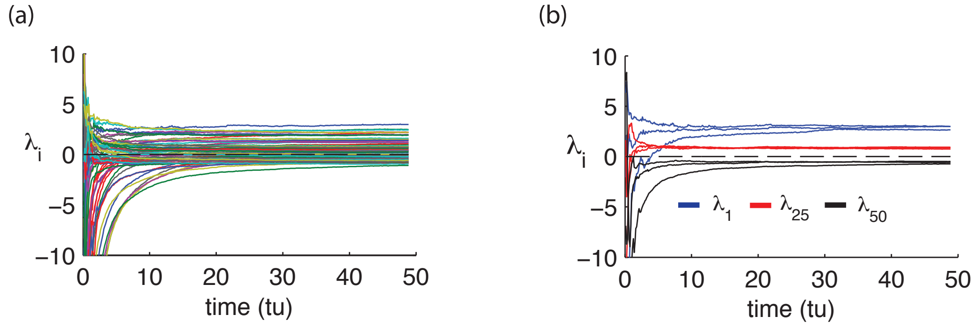

Figure B.1: Initial 50 out of 5000 time-units converging estimates of Lyapunov exponents. (a) Estimates of the first 60 Lyapunov exponents (out of 500) for a given network. (b) Three distinct estimates for λ_1, λ_{25} and λ_{50} where network IC, I and coupling matrix A are selected at random. For both panels, $N = 500$, $\varepsilon = 0.5$, $\eta = -0.5$.

B.1.2 Lyapunov spectrum estimates

Although the Lyapunov exponents $\lambda_1 \geq \lambda_2 \geq ... \geq \lambda_N$ of (B.1) do not depend on a particular choice of I or initial conditions (IC), computing them analytically is a very hard, if not impossible problem. Therefore, we use numerical estimates to approximate them. While numerically integrating a solution of (B.1) above, we simultaneously evolve the linear variational equation

$$\dot{M} = J(t)M \tag{B.2}$$

where $J(t)$ is the Jacobian of (B.1) evaluated along the simulated trajectory. M is a N by N matrix with $M(0)$ is the identity. $M(t)$ is orthonormalized at each time-step and the growth factors of each orthogonal vector obtained from the process are extracted to build estimates that converge toward λ_i's, as described in [40]. This process was repeated for ten random input choices I and initial states, were trajectories were integrated for 5000 time-units. We verified that all reported λ_i's have a standard error less than 0.002 using the method of batch means [1] (batch size of 100 time-units). Figure B.1 (a) shows the initial 50 time-units of converging estimates of the first 60 Lyapunov exponents.

In addition, we find that distinct realizations of connectivity matrix $A = \{a_{ij}\}$ did not significantly affect the Lyapunov exponent estimates, and even less the sum of all positive ones leading to the Kolmogorov-Sinai entropy h_μ. Figure B.1 (b) shows estimates of three λ_i's for three distinct systems, where input choice I, IC and A are all different.

B.2 Validity of $\mathbb{T}^N$-partition assumption

The derivation of the Kolmogorov-Sinai noise entropy bound H_{KS} relies on a simple assumption concerning dynamics of single cells. Namely, that neuron i will spike in time bin $[t, t + \Delta t]$ if and only if $\theta_i(t) \in \gamma_1$ where $\gamma_1 = [1 - 2\Delta t, 1)$. As explained in Chapter 4 this simplification arises from the linearization of θ_i's flow about the spiking phase $\theta_i = 1$ which does not depend on network state nor external inputs. Indeed, such perturbations affect cell i's dynamics via the phase response curve $Z(\theta_i)$ in (B.1) which vanishes at $\theta_i = 1$. It is easy to see that this assumption holds in the limit $\Delta t \to 0$ but it is unclear it breaks down when Δt is small but fixed.

There are two ways in which a neuron's dynamics can violate this partition-based rule: either $\theta_i(t) < 1 - 2\Delta t$ and excitatory inputs (external and network induced) are strong enough to make θ_i spike sometime in $[t, t + \Delta t]$ or $\theta_i(t) \in \gamma_1$ and inhibitory inputs are strong enough to prevent θ_i from spiking in $[t, t+\Delta t]$. Since $Z(\theta_i)$ is vanishingly small on γ_1 for small Δt, such scenarios are very unlikely and their probabilities of occurrence depend on very complex coincidences involving incoming network spikes and input $I_i(t)$ over a Δt time window. In what follows, we do not attempt to analytically track down the probability of such scenarios but rather compare the spiking activity of model (B.1) with an analogous system for which this partition assumption holds true by design.

B.2.1 Piecewise model comparison

Consider the *piecewise* model analogous to system (B.1):

$$d\theta_i = [\tilde{F}(\theta_i) + \tilde{Z}(\theta_i)\sum_{j=1}^{N} a_{ij} g(\theta_j) + \frac{\varepsilon^2}{2}\tilde{Z}(\theta_i)\tilde{Z}'(\theta_i)]dt + \tilde{Z}(\theta_i)\underbrace{[\eta dt + \varepsilon dW_i]}_{I_i(t)} \tag{B.3}$$

in which we replace the functions F and Z by the following piecewise-defined terms:

$$\tilde{F}(\theta_i) = \begin{cases} 1 + \cos(2\pi\theta_i) & ;\ \theta_i \in [0, 1 - 2\Delta t) \\ 2 & ;\ \theta_i \in [1 - 2\Delta t, 1) \end{cases}$$

$$\tilde{Z}(\theta_i) = \begin{cases} 1 - \cos(2\pi\theta_i) & ;\ \theta_i \in [0, 1 - 2\Delta t) \\ 0 & ;\ \theta_i \in [1 - 2\Delta t, 1). \end{cases}$$

It is easy to see that the network defined by (B.3) respects the partition-based spiking rule described above. However, notice that for $\Delta t > 0$, both $\tilde{F}$ and $\tilde{Z}$ are discontinuous functions of S^1 and that (B.3) is ill-defined since $\tilde{Z}'(1 - 2\Delta t)$ does not exist. Nevertheless, for practical purposes, we can simulate system (B.3) and approximate its Lyapunov spectrum since there is only one discontinuity point per neuron and the probability of a discretized trajectory landing on such points is zero.

The purpose of model (B.3) is to assess the differences arising between the true dynamics of (B.1) and the idealized spiking assumption. We fix $\Delta t = 0.05$ as in Chapter 4 and begin by comparing single cell dynamics between the "normal" and piecewise models. Figure B.2 shows a simulated single cell trajectory from each model, with identical input I_i and incoming balanced spike trains extracted from a separate network simulation. This mimics the activity a single cell would receive while imbedded in a network. Notice that apart from small discrepancies that can sometimes arise between spike times, the two trajectories agree almost perfectly. When differences do arise, they are quite small. From a simulation yielding about 3000 spikes from both models, most corresponding spikes from the normal and piecewise models where indis-

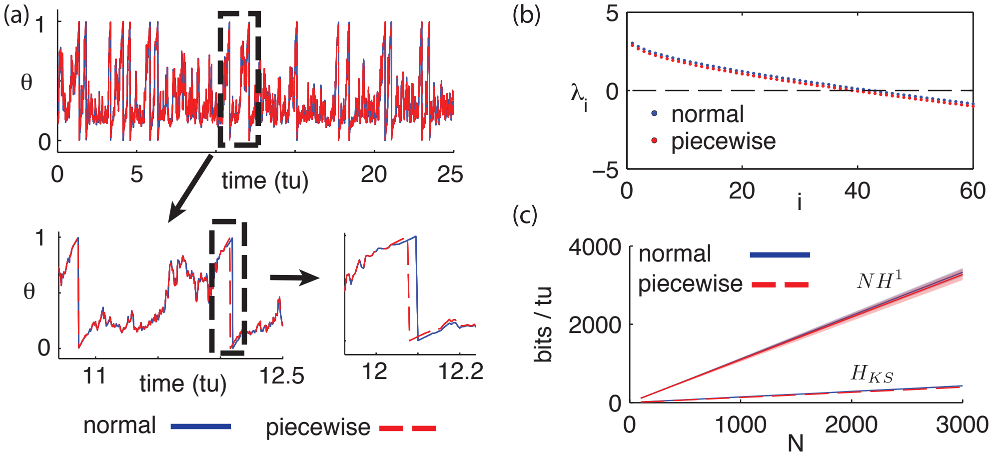

Figure B.2: (a) Single cell trajectory comparison for models (B.1) and (B.3) where initial conditions and inputs are fixed. (b) First 60 Lyapunov exponents of models (B.1) and (B.3). (c) Empirical noise entropy bounds NH^1 and H_{KS} for models (B.1) and (B.3). For all panels, $\eta = -0.5$, $\varepsilon = 0.5$, $\Delta t = 0.05$. For panels (b) and (c), $N = 500$, $\kappa = 20$.

tinguishably close, down to the numerical solver's time-step. The maximal difference was about 0.02 time-units, smaller than a Δt time-bin. In addition, we found that for simulated trajectories of 1000 time-units from network (B.1), only about 0.01% of all spikes violated the spiking rule assumption. This number dropped to zero for $\Delta t = 0.01$.

Since our system is chaotic, one expects network spiking output from (B.1) and (B.3) to differ since small perturbations are amplified. However, of relevance is not an exact match of spike output for fixed IC and I between the two models but their respective noise entropy production. Figure B.2 (b) shows the first 60 Lyapunov exponents of a network with size $N = 500$, simulated with both the normal (B.1) and piecewise (B.3) models. Since, Lyapunov exponents depend on the Jacobian of a system, we expected the piecewise model to yield smaller exponents since it's derivative is zero on the intervals $[1 - 2\Delta t, 1)$. However, this difference is very minimal and amounts for a difference of about 0.002 bits per neuron per time-unit in the slope of the H_{KS} estimates shown in Figure B.2 (c). Finally, we empirically estimate the noise entropy bound H^1, as described in Chapter 4, for the piecewise model (B.3). Its value differed from the normal model estimate by about 0.01 bits per neuron per time-unit, well below the standard error of the mean of estimates from both models, as can be seen in Figure B.2 (c).

In light of these tests, we feel confident that the H_{KS} bound we derive in Chapter 4 reflects a robust phenomenon present in driven balanced networks of the type modeled by (B.1).